

INVESTIGATING SECOND HARMONIC GENERATION IN COLLAGEN TISSUES

by

MENGZHE SHEN

B.Sc., Shanghai Jiao Tong University, 2007

M.Phil., University of Hong Kong, 2009

A THESIS SUBMITTED IN PARTIAL FULFILLMENT OF
THE REQUIREMENTS FOR THE DEGREE OF

DOCTOR OF PHILOSOPHY

in

THE FACULTY OF GRADUATE AND POSTDOCTORAL STUDIES
(ELECTRICAL AND COMPUTER ENGINEERING)

THE UNIVERSITY OF BRITISH COLUMBIA

(Vancouver)

August 2015

© Mengzhe Shen, 2015

Abstract

Collagen is the most abundant structural protein in the human body. When it is excited by femtosecond near infrared laser, second harmonic generation (SHG) signal at half the wavelength of the excitation wave is excited. For imaging thick tissues, the SHG signal is collected in the backward direction. The objective of this work is to elaborate the origin of the backward SHG in collagen at the fibril level and investigate some of its optic characteristics.

The optic characteristics investigated include the wavelength dependence of SHG intensity, which is useful to analyze SHG in collagen tissues. However, the current published results are inconsistent. We study the microscopy system factors affecting the wavelength dependence and calibrate them by measuring the wavelength dependence of SHG intensity in a BaB₂O₄ crystal. With the proper calibration, typical wavelength dependence SHG spectra from mouse tail and Achilles tendon are investigated.

The backward-collected SHG signal includes the backward generated SHG, and the forward generated but backward scattered SHG. Those two sources of the total backward SHG have different properties due to the difference in phase mismatch in the forward and backward directions. Here a non-invasive method is developed to separate them by using pinholes. By varying the pinhole size in a confocal multiphoton microscopy, the proportion of the backward scattered SHG to the total backward SHG can be obtained. Our results indicate that backward scattered SHG may not be the major source of backward SHG in the mouse tail tendon, which means significant SHG is purely generated in the backward direction.

A large phase mismatch exists in generating backward SHG. Nevertheless, significant backward generated SHG has been observed in collagen tissues. We hypothesize that the periodic lattice structure of fibrillar collagen can provide a virtual momentum to assist the

backward phase matching. Here the backward SHG phase matching is investigated in theory, simulation, and experiments, which are consistent and support the hypothesis.

The various properties investigated in this thesis can provide a better understanding about SHG in collagen tissues and lead to new applications of SHG microscopy in diagnosing collagen related diseases in the future.

Preface

All of the work presented henceforth was conducted in the Biophotonics Laboratory at the University of British Columbia, Vancouver and Integrative oncology department at the British Columbia Cancer Agency Research Center, Vancouver. All animal experiments were approved by the University of British Columbia's Committee on Animal Care [certificate #A10-0338].

A version of Chapter 3 has been published

- *Mengzhe Shen, Jianhua Zhao, Haishan Zeng, and Shuo Tang. "Calibrating the measurement of wavelength dependent second harmonic generation from biological tissues with a BaB₂O₄ crystal." Journal of Biomedical Optics 18:031109, 2013.*

I was the lead investigator, responsible for all major areas of theory, simulation and experiment, as well as manuscript composition. Jianhua Zhao was involved in the single photon excitation spectrum measurement. Shuo Tang was the supervisory author on this project and was involved throughout the project in concept formation and manuscript composition.

A version of Chapter 4 has been published

- *Mengzhe Shen, Yunxian Tian, Shau Poh Chong, Jianhua Zhao, Haishan Zeng, and Shuo Tang. "Quantifying the backscattering of second harmonic generation in tissues with confocal multiphoton microscopy." Journal of Biomedical Optics 18:115003, 2013.*

I was the lead investigator, responsible for all major areas of theory, simulation and experiment, as well as manuscript composition. Yunxian Tian was involved in the helping with conducting experiment. Shau Poh Chong provided the original version of the simulation program code. Shuo Tang was the supervisory author on this project and was involved throughout the project in concept formation and manuscript composition.

I was the lead investigator for the projects located in Chapters 5 where I was responsible for all major areas of theory, simulation and experiment, as well as manuscript composition. Shuo Tang was the supervisory author on this project and was involved throughout the project in concept formation and manuscript composition.

Other conference publications are

- *Mengzhe Shen, Hequn Wang, Anthony Lee, Jianhua Zhao, Haishan Zeng, and Shuo Tang. “A study on the spectral dependence of second harmonic generation from collagen tissues.” SPIE BIOS 82263R, 2012.*
- *Mengzhe Shen, Yunxian Tian, Shau Poh Chong, Jianhua Zhao, Haishan Zeng, and Shuo Tang. “Investigating backward scattered second harmonic generation from various mouse collagen tissues.” SPIE BIOS 89482V, 2014.*

Table of Contents

Abstract.....	ii
Preface.....	iv
Table of Contents	vi
List of Tables	ix
List of Figures.....	x
List of Abbreviations	xvi
Acknowledgements	xviii
Dedication	xx
Chapter 1: Introduction	1
1.1 Collagen	1
1.1.1 Collagen molecule structure and disorders	1
1.1.2 Conventional measurement techniques.....	3
1.2 SHG microscopy.....	4
1.3 Review of research on SHG from collagen	9
1.3.1 SHG imaging in forward and backward directions.....	10
1.3.2 SHG directionality	12
1.3.3 Current models interpreting SHG from collagen.....	13
1.4 Objectives and contributions.....	15
1.5 Outline.....	16
Chapter 2: Classic theory of second harmonic generation	18
2.1 Nonlinear polarization	18

2.2	SHG in bulk material	20
2.3	Phase matching	21
Chapter 3: Measuring the wavelength dependence of SHG and calibrating with a BaB₂O₄ crystal.....		25
3.1	Introduction.....	25
3.2	Material and methods.....	28
3.2.1	SHG power expression from BBO crystal.....	28
3.2.2	Experiment setup	33
3.2.3	System factors affecting wavelength dependence	35
3.3	Calibration results	41
3.4	SHG excitation spectrum from collagen tissues	42
3.5	Conclusions.....	47
Chapter 4: Quantifying the back scattering of SHG		48
4.1	Introduction.....	48
4.2	Methods.....	52
4.2.1	Calculation methods.....	52
4.2.2	Sample preparation	54
4.3	Monte Carlo simulation	55
4.4	Experiment setup and calibration.....	63
4.5	Experimental results and discussions.....	67
4.6	Conclusions.....	75
Chapter 5: Phase matching of backward second harmonic generation assisted by lattice structure.....		76

5.1	Introduction.....	76
5.2	Theory.....	79
5.2.1	Lattice assisted phase matching and angle tilting for backward SHG.....	79
5.2.2	Theoretical background of the SHG in collagen simulation.....	81
5.3	Simulations	83
5.3.1	Effect of lattice structure and angle tilting on phase matching for backward SHG .	83
5.3.2	Effect of single fibril and excitation beam focusing on backward SHG excitation spectrum.....	86
5.4	Experiment.....	89
5.4.1	Experiment setup and preparation	89
5.4.2	Manipulating the excitation beam angle.....	93
5.4.3	Manipulating the emission beam angle.....	96
5.4.4	The impact of different fibril diameter	98
5.4.5	Manipulating both the excitation and emission angle.....	100
5.5	Conclusions.....	101
Chapter 6: Summaries and future work.....		103
6.1	Summaries.....	103
6.2	Future work.....	105
Bibliography		108
Appendices.....		115
Appendix A Monte Carlo method for simulating photon transportation.....		115
Appendix B Plane wave expansion method.....		118

List of Tables

Table 4.1 A summary of the curve fitting parameters for pinhole experiment results and the derived values describing the scattering property of the tail tendon tissue at different depths. ...	71
Table 4.2 The ρ and $c(1)$ values at different depths for mouse tail tendon tissues from three animals.	72
Table 4.3 The curve fitting parameters and the derived ρ and $c(1)$ values of Achilles tendon with different thicknesses at 50 μm depth.	74

List of Figures

Figure 1.1 (left) Hierarchical structure of tendon; (right) TEM image of collagen tissue sample with 250 nm scale bar. From © P. Fratzl, “Collagen: structure and mechanics”. 2008: Springer Science & Business Media. Page 10. By permission from publisher.	3
Figure 1.2 Illustration of one-photon, two-photon and SHG energy diagram. The thick black lines represent the ground state. Thin gray lines represent electronic states and dashed lines represent virtual states. Different colored solid arrows indicate the incident and generated photons.	6
Figure 1.3 Experiment setup of a typical SHG microscopy.	7
Figure 1.4 SHG images of a thin section of Achilles tendon (a) forward image (b) backward image. From © F. Legare, C. Pfeffer, and B. R. Olsen, “The role of backscattering in SHG tissue imaging”. Biophysical journal, 2007. 93(4): p. 1212-1320. Page 1214. By permission from publisher.	11
Figure 1.5 High resolution images revealing the hollow tube appearance of thick fibrils which can be resolved by SHG microscopy. The hollow cores are marked by arrows. From © R. M. Williams, W. R. Zipfel, and W. W. Webb, “Interpreting second-harmonic generation images of collagen I fibrils”. Biophysical journal, 2005. 88(2): p. 1377-1386. Page 1381. By permission from publisher.	15
Figure 2.1 Normalized SHG intensity versus normalized phase mismatch $\Delta k_b L / 2\pi$. The intensities for three different lengths L are marked. The refractive indices for excitation and SHG waves n_1, n_2 are 1.35 for simplicity and excitation wavelength is 800 nm.	23
Figure 3.1 (a) Calculated wavelength dependent phase matching in BBO crystal; (b) comparison of calculated wavelength dependent SHG power in different NA situations.	29

Figure 3.2 Experimental setup for wavelength dependent SHG measurements in forward and backward directions from BBO and mouse tissues. 34

Figure 3.3 (a) Pulse width measurement results before objective lens; (b) Plot of excitation power versus analyzer angle at different wavelengths; (c) Plot of emission power versus analyzer angle at different wavelengths. 36

Figure 3.4 (a) Factory supplied NIST traceable spectrum of the standard lamp (black) and the lamp spectrum measured by our optical system (red) with which transmission/detector response correction coefficient is calculated (green); (b) One-photon and two-photon fluorescence emission spectrum for NADH with or without transmission/detector response calibration. 39

Figure 3.5 Experiment results for wavelength dependent SHG power versus emission wavelength with (a) 40X objective (NA=0.8), (b) 10X objective (NA=0.25) and (c) collimated beam; (d) theoretical and experimental comparison for wavelength dependent SHG power for collimated beam and focused beams. 42

Figure 3.6 Wavelength dependent SHG spectrum from 10 μm mouse tail tendon with two typical spectrum patterns: (a) monotonically decreasing and (b) single peak. For each pattern, five spectra are plotted. The error bar draws the standard deviation of six repeated measurements at a same location. 44

Figure 3.7 Wavelength dependent SHG spectrum from 10 μm mouse Achilles tendon with two typical spectrum patterns: (a) monotonically decreasing and (b) single peak. For each pattern, five spectra are plotted. The error bar draws the standard deviation of six repeated measurements at a same location. 45

Figure 4.1 An illustration of photon generation and collection by pinholes in the Monte Carlo simulation with various SHG signal components in forward and backward directions. 51

Figure 4.2 (a) The BG-SHG intensity only versus radial distance from optical axis in the pinhole image plane for SHG at 50, 75 and 100 μm depth; (b) BG-SHG intensity only distribution without scattering in the pinhole image plane; (c) BS-SHG intensity only versus radial distance from optical axis at 50 μm depth with 300 μm thicknesses; (inset) the zoomed in BS-SHG distribution over a shorter range; (d) dependence of relative B-SHG power on pinhole sizes for F/B ratio = 7.5 in the focal plane at the 50, 75 and 100 μm depths; (e) BG-SHG intensity versus radial distance from optical axis for reduced scattering coefficients 15, 45 and 75 cm^{-1} ; (f) dependence of relative B-SHG power on pinhole sizes for F/B ratio = 7.5 in the focal plane at three reduced scattering coefficients; (g) BS-SHG intensity versus radial distance from optical axis for tissue thicknesses as 300, 500 and 1000 μm ; (h) dependence of relative B-SHG power on pinhole sizes for F/B ratio = 7.5 in the focal plane for the three thicknesses. 57

Figure 4.3 (a) Experiment setup for measuring the scattering property of tissues based on a confocal multiphoton microscopy; $\lambda/2$, half wave plate; PBS, polarization beam splitter; F1, F2, and F3, filter sets; L1, L2, L3, and L4, lens sets; OBJ1, and OBJ2, objective lens; DM, dichroic mirror; (b) experiment measurement for the dependence of relative backward TPEF power on fiber diameter for TPEF solution and the fitting curve with $\omega = 15 \mu\text{m}$; (c) TPEF intensity distribution along the horizontal direction on CCD image plane and its fitting with Gaussian shape; (inset) CCD captured image for TPEF signal; (d) experiment measurement for the dependence of relative B-SHG power on fiber diameter for of 10 μm mouse tail tendon tissues and the fitting curve with $\omega = 14 \mu\text{m}$ 63

Figure 4.4 (a) Experiment measurement for the dependence of relative B-SHG power on fiber diameter for mouse tail tendon at different depths and the related fitting curves; (b) contour map

plotting the isolines of fitting error with various ω and fc/b ; the sensitivities are plotted along the two dash lines crossing at the best fitting pair ($\omega = 75$ and $fc/b = 0.0005$) as a function of ω (c) and fc/b (d); (e) the dependence of relative B-SHG power on fiber diameter for tail tendon and Achilles tendon with similar tissue thicknesses and focal point depth; (f) the dependence of relative B-SHG power on fiber diameter for Achilles tendon with different thicknesses but at the same focal point depth 50 μm 67

Figure 5.1 (a) Illustration of the periodic structure with elementary lattice vectors $(a,0)$ and $(0,a)$; The red and green arrows represent the wave vector of fundamental and SHG $k_{\text{fundamental}}$, k_{SHG} ; (b) the corresponding k space diagram with elementary reciprocal vector $(0,2\pi/a)$ and $(2\pi/a, 0)$; The red, green and purple arrows between A, B dots illustrate fundamental, SHG wave vector k_1 , k_2 and the backward phase mismatch Δk 81

Figure 5.2 The contour map of $\Delta k'_x$, $\Delta k'_y$ and SHG intensity depends on fundamental excitation angle α and SHG emission angle θ for 800 nm excitation wavelength (a)-(c) and 900 nm excitation wavelength (d)-(f). (g) For $\alpha = -\theta = 0^\circ$ and 23.4° , the corresponding SHG intensity from 750 nm to 950 nm. The structure is $N_x = 4$, $N_y = 10$ and $a = 150$ nm. 85

Figure 5.3 The normalized SHG excitation spectrum for fibril diameter $d = 140$ nm, structure $N_x = 4$, $N_y = 10$, without (solid green) and with (dash cyan) focusing. In the non-focusing case, $\alpha = 0^\circ$. The focused beam effect is simulated through summing up the excitation spectrum generated by plane waves with incidence angles vary from 0 to 35° . The wavelength dependence of $F(k_1, k_2)^2$ function is plotted in dash dot purple, which shows the impact of single fibril on excitation spectrum. 88

Figure 5.4 Pictures of the ring filters and schematics of their positioning in the beam path for different experiment conditions: (a) filtering the excitation path; (b) filtering the emission path and (c) filtering both excitation and emission path. (d) illustration of SHG excitation spectrum. The solid curve are the SHG emission spectra for different excitation wavelengths from 750 to 950 nm. The dashed line is the SHG excitation spectrum. 90

Figure 5.5 (a) The normalized and (b) actual average excitation spectrum of mouse tail tendon with the excitation path filtered by ring filter B1; The results are averaged over three measurements at the same location and the error bar shows the standard deviation. The allowed α angles are 12° to 22° and 23° to 32° . (c) Simulation results with $a = 150$ nm, $d = 140$ nm and fibril numbers $N_x = 4$, $N_y = 10$ for the above angled excitation beams..... 95

Figure 5.6 One typical type of the (a) normalized and (b) actual average excitation spectrum of mouse tail tendon with the emission path filtered by ring filter B2; (c) another typical type of the normalized excitation spectrum; (d) simulation for the experiment results in (a) with $a = 150$ nm, $d = 140$ nm and fibril numbers $N_x = 4$, $N_y = 10$ for focused excitation beam. When the emission path is filtered, the allowed $-\theta$ angles are 0° to 11° , 12° to 17° , 18° to 22° , 24° to 28° and 29° to 33° 97

Figure 5.7 (a) Normalized and (b) actual average excitation spectrum of mouse Achilles tendon with the emission path filtered by ring filter B2; (c) simulation for the experiment results in (a) with $a = 120$ nm, $d = 110$ nm and fibril numbers $N_x = 4$, $N_y = 10$. When the emission path is filtered, the allowed θ angles are 12° to 17° , 18° to 22° , 24° to 28° and 29° to 33° 99

Figure 5.8 (a) Experimental results of the normalized excitation spectrum comparison with different filtering setups for mouse tail tendon; (b) Simulation results with (dash) and without (solid) excitation path filtering. $a = 150$ nm and $d = 140$ nm with fibril numbers $N_x = 4$, $N_y = 10$.

When the excitation beam is filtered by the rings, the allowed α angles are 12° to 22° and 23° to 32° 101

Figure A.1 Flowchart for Monte Carlo simulation of photon propagation in tissues. From © V. Periyasamy and M. Pramanik, “Monte Carlo simulation of light transport in tissue for optimizing light delivery in photoacoustic imaging of the sentinel lymph node”, Journal of biomedical optics, 2013. 18(10): p. 106008-106008 [100]. Page 3. By permission from publisher.....117

Figure B.1 Comparison of (top) our calculated photonic band structure of a 2D square lattice composed of circular cylinders with the (bottom) results given in text book. From © K. Sakoda, “Optical properties of photonic crystals”. Vol. 80. 2004: Springer Science & Business Media. Page 29. By permission from publisher.....121

Figure B.2 Electrical fields of TE modes inside a unit square array of dielectric cylinders in medium. The color indicates the amplitude of the electrical field. The parameter simulations are $a = 150$ nm, $d = 140$ nm, $n_{cylinder} = 1.4$, $n_{medium} = 1.3$ with excitation wavelength at 800 (a) and 400 nm (b). In (c), the excitation wavelength is 800 nm and $d = 30$ nm.....122

List of Abbreviations

AFM Atomic force microscopy

BBO BaB₂O₄

BF Bandpass filter

BG-SHG Backward generated SHG

B-SHG Backward SHG

BS-SHG Backscattering of the forward generated SHG

CT Computed tomography

DM Dichroic beam splitter

EDS Ehlers-Danlos syndrome

F/B Forward over backward intensity ratio

FIB Focused ion-beam

FT-SHG Fourier transform-second-harmonic generation

FWHM Full width half maximum

MC Monte Carlo method

MRI Magnetic resonance imaging

NA Numerical aperture

NaCl Sodium chloride

NADH Nicotinamide adenine dinucleotide

ND Neutral density

OI Osteogenesis Imperfecta

PBS Polarization beam splitter

PMT Photo-multiplier

PRS Picro-sirius red

QPM Quasi-phase matching

RAFT Real architecture for 3D tissue

SAAID Second harmonic to auto-fluorescence aging index of dermis

SEM Scanning electron microscopy

SHG Second harmonic generation

TEM Transmission electronic microscopy

TPEF Two photon excitation fluorescence

Acknowledgements

Many people have contributed to this work both directly and indirectly. Firstly, I would like to thank my supervisor Dr. Shuo Tang for giving me this opportunity to study at UBC ECE and her constant patience in providing guidance during my Ph.D career. Secondly, I would like to thank Dr. Haishan Zeng for kindly giving access to the equipment at oncology imaging lab at BCCRC so that I can conduct the experiments necessary for this thesis work. I am indebted to Jianhua Zhao who has provided constant support and pleasant collaboration throughout my research at BCCRC. In addition, I would like to thank all members (past and present) of both BCCRC and the UBC labs for a pleasant time and excellent collaborations. The following listing order is based on the time sequence that I met with each of you. You are: Kanny Chan, Yinqiu Yu, Yifeng Zhou, Jiali Yu, Leo Pan, Tom Lai, Shau Poh Chong, Lin Huang, Min Ai, Weihang Shu, Yuan Zhao, Mingyu Sheng, and Xin Zhou from UBC ECE. You are Hequn Wang, Kam Chow, Yunxian Tian, Wenbo Wang, Shangyuan Feng, Yimei Huang, and Zhenguo Wu from BCCRC.

I extend my thanks and gratitude to all the friends in and out Vancouver for your genuine help and accompany in the last six years. Considering the hundreds of contacts on my WECHAT and FACEBOOK homepage, I am not able to name all of you here but I remember all the stories among us, joy or sorrow. I would like to thank my parents, in China for giving me the opportunity and support needed to get to where I am today. I understand that not being able to witness my growing day by day in the past years is their regret and they tolerate this for my benefit. Lastly, I would like to thank my wife, Jie Lu, for everything.

Finally, I would like to thank a group of special people who has very the same God's life in me. It is you who make Vancouver my second home on this blue planet. Thank God for putting me among you under His dominion and arrangement. May we all dwell in the house of Jehovah for all the days of our lives.

Dedication

For everything there is a season, And a time for every purpose under heaven:

A time to be born, and a time to die; A time to plant, and a time to pluck up what is planted;

.....

A time to love, and a time to hate; A time for war, and a time for peace.

What profit does the worker have in all that he labors?

I have seen the travail that God has given the children of men to travail in.

He has made everything beautiful in its own time; also He has put eternity in their heart, yet so that man does not find out what God has done from the beginning to the end.

.....

That which is has already been, and that which will be has already been; and God seeks what has passed.

Ecclesiastes 3:1-15

Chapter 1: Introduction

1.1 Collagen

As an important functioning protein and one found abundantly in human body, investigating collagen's fiber structure organization and variation is key to our understanding and treatment of many diseases. On one hand, collagen provides the necessary strength and toughness to a wide range of organs such as cornea, tendon and bone [1-4]. On the other hand, biological functions such as tissue repairing and scaffolding are served by collagen [5, 6]. Because of these functions, collagen is involved in different stages of physiological and disease processes [7, 8].

Although people have already found more than twenty types of collagen in human body, type I collagen, which is grouped as fibrillary collagen, dominates by accounting for as much as 90% of the total collagen. In this section, we review the basics about type I collagen such as its molecule structure, macromolecule hierarchy, common diseases associated with it and some conventional techniques to probe it.

1.1.1 Collagen molecule structure and disorders

Type I collagen molecule is composed of three polypeptide chains (α -chains). These chains form a right-handed triple helical structure held together by hydrogen bonds. Each molecule is 1.5 nm in diameter and 300 nm in length. Fig. 1.1 shows the hierarchical organization of fibrillar collagen in tendon [9]. From the lowest level to highest level, collagen molecules organize to form fibrils along the axial direction. Fibrils shown in the transmission

electronic microscopy (TEM) image have a diameter ranging from 50 nm to 500 nm in different tissues. Multiple collagen fibrils are joined together to form a collagen fascicle and fiber.

Many diseases are characterized by defects or disorders of type I collagen in the respective tissues. For example, Osteogenesis Imperfecta (OI) is associated with connective tissue disorder and is characterized by abnormal collagen assembly that shows symptoms such as fragile bones and reduced bone mass. Ehlers-Danlos syndrome (EDS) is another kind of inherited connective tissue disorder which is caused by problematic structure, production and processing of collagen. Patients diagnosed with EDS suffer from a fragile and tender skin, and easy bruising [10, 11]. Collagen gene mutations are likely to be the reason behind these defects. Additionally, abnormal collagen assembly is also observed in malignant tumors which is different from what is observed in the normal tissues [12]. In order to understand the role of collagen in healthy and diseased tissues, and further to develop diagnosis and treatment methods, it is necessary to probe the collagen fiber organization and structure.

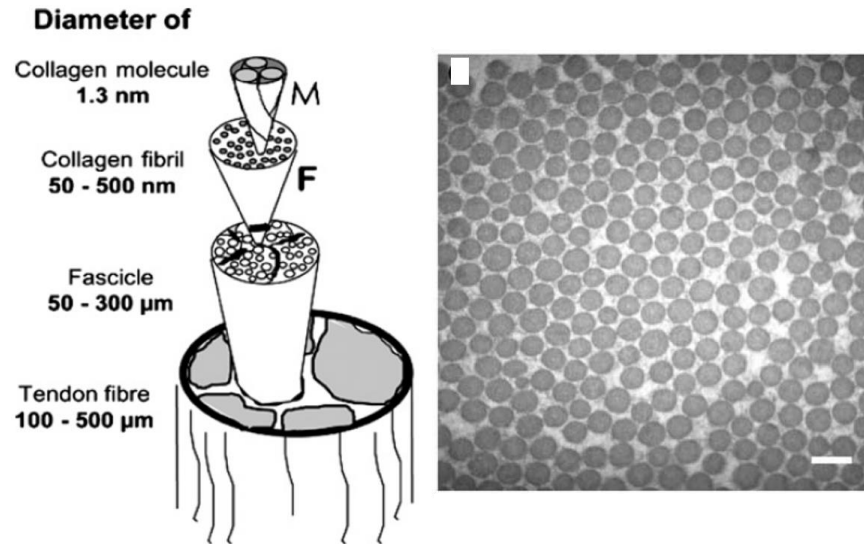


Figure 1.1 (left) Hierarchical structure of tendon; (right) TEM image of collagen tissue sample with 250 nm scale bar. From © P. Fratzl, “Collagen: structure and mechanics”. 2008: Springer Science & Business Media. Page 10. By permission from publisher.

1.1.2 Conventional measurement techniques

In the first half of this century, light microscopy was the principal technique for the study of connective tissues such as collagen but the fine organizations could not be visualized in very detail. During the last a few decades, scanning electron microscopy (SEM) has become widely employed but tremendous efforts were taken to remove the cellular elements hampering measurements [13, 14].

TEM has long been used for microstructural examinations at nano-size scales, with numerous studies on collagen being reported in literature over the past years [15]. The axial 67 nm periodicity (D period) that separates collagen from other fibrillary molecules is first discovered by TEM. The advent of diamond-knife microtomy, ion beam techniques, and focused

ion beam (FIB) preparation methods gradually evolve to reduce the work load of sample preparation and avoid artificial damage [16, 17].

Atomic force microscopy (AFM) has also contributed to the understanding of collagen structure. An advantage of AFM over SEM or TEM is that it can be used to investigate biological systems in aqueous solution, thereby preserving their physiological conformations and functions [18]. In addition, the high signal-to-noise ratio, superior to any other microscopic technique, can permit resolution of surface structural details down to less than 1 nm [19].

However, SEM, TEM and AFM require special sample preparation and can't be used in imaging thick tissues or tissues *in vivo*.

1.2 SHG microscopy

Compared with electron microscopy and AFM, optical imaging methods offer key advantages such as non-invasiveness. In addition, they are simple regarding sample preparation, setup implementation, and image post processing and interpretation.

For imaging collagen fibers with optical methods, the combination of confocal microscopy and a specific stain picro-sirius red (PSR) have been used to study the 3D morphology of collagen in cardiac tissues [20, 21]. Compared with light and polarization microscopy, it provides more insight into the spatial arrangement of collagen fibers. However, a drawback with PSR is that the content amount of collagen cannot be determined by the strength of the fluorescence due to the binding manner of the PSR with collagen [22].

Among all the optical imaging techniques, a nonlinear optical technique called second harmonic generation (SHG) imaging is well suited for imaging collagen fibers [23-26]. SHG is associated with a non-centrosymmetrical environment which gives rise to a hyperpolarizability β

at the molecular scale. In biological tissues, it is the peptide bonds along the protein backbones that exhibit β . The SHG signal in a macromolecular assembly of collagen is from the coherent summation of these elementary β contributions [27]. At the macroscopic level, the susceptibility $\chi^{(2)}$ is used to describe SHG, which originates from the macromolecular assembly. Besides collagen type I, it is reported that other fibrillar collagens such as type II and III can also generate SHG. For example, cartilage which is mainly composed of type II collagen has been visualized by SHG [28]. Purified amorphous type III collagen also generates SHG but its intensity is much weaker than that from type I collagen in human skin [25, 29].

Two-photon excitation fluorescence (TPEF) microscopy is a widely used nonlinear microscopy technique. SHG microscopy is another nonlinear microscopy that targets at imaging specific biological structures, such as collagen. It has the advantages such as endogenous contrast, preservation of phase information and specificity to molecular structure organization. In Fig. 1.2, a comparison of one-photon and two-photon fluorescence, and SHG regarding their energy diagram is illustrated. In one-photon fluorescence, a fluorophore is excited to an excited state after the absorption of a high-energy photon first. Subsequently, some of the energy absorbed is lost through vibrational relaxation and the remaining energy is re-radiated as a photon of lower energy when the fluorophore returns to its ground state. In two-photon fluorescence, two lower energy photons are absorbed simultaneously to excite the fluorophore, assisted by an intermediate “virtual” state. Same as the one-photon case, the transition from the ground state to excited state also involves with molecular absorption and the subsequent emission of a fluorescence photon. In both cases, the absorption of energy eliminates the coherence between the emitted fluorescence photon and the original excitation photons. Potential photo-damage of the fluorophore is caused by this mechanism. In contrast, SHG operates by a

mechanism without the involvement of medium absorption. A single higher energy photon is created when two lower energy photons with twice the wavelength are annihilated simultaneously. In this mechanism, no molecular absorption takes place and photo-damage is greatly reduced. The coherence between the incoming photons and the emitted SHG photon is maintained.

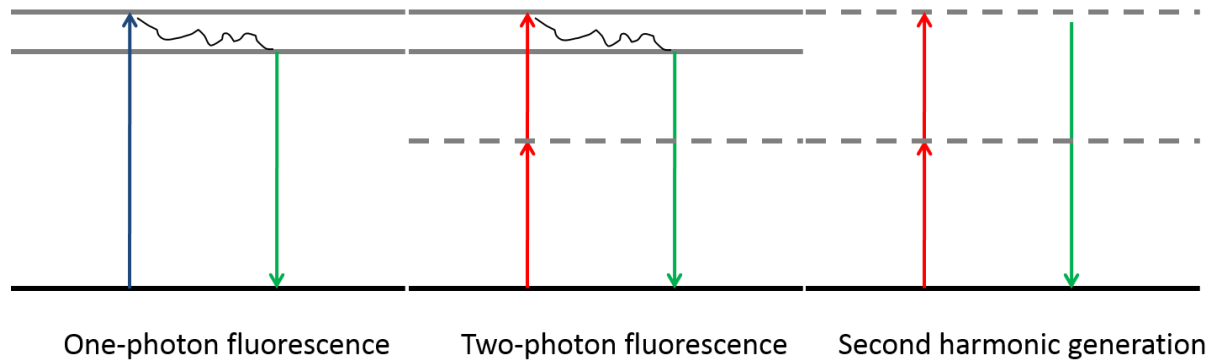


Figure 1.2 Illustration of one-photon, two-photon and SHG energy diagram. The thick black lines represent the ground state. Thin gray lines represent electronic states and dashed lines represent virtual states. Different colored solid arrows indicate the incident and generated photons.

A schematic experimental setup for SHG microscopy is shown in Fig. 1.3 [30]. A wavelength tunable Ti:Sapphire laser produces a laser beam with femtosecond pulse width and linearly polarized pulses at tens of MHz repetition rate. The choice of wavelength depends on the biological tissue under investigation, but its usual range is from 700 nm to 1000 nm. After passing through a combination of relay lens for beam spatial filtering and collimation, the beam is sent to a galvanometer-driven XY scanner, which is driven by a raster-scanning pattern. After transmitting through a long pass dichroic mirror (DM), the beam is focused onto the sample by a high numerical aperture (NA) water-immersion illumination objective. The generated signal is collected in forward direction by a second objective with an NA larger than that of the first

objective for efficient collection. The excitation beam is filtered out in the collection path by a bandpass filter (BF). The SHG signal is further selected by a filter that transmits only the SHG signal wavelength. A photo-multiplier tube (PMT) records the SHG intensity by counting the number of photons reaching it. The imaging is synchronized with the raster scanning of the galvo-scanner, and 3D image stacks are acquired from various depths into the sample. In a similar fashion, the SHG signal can also be collected in the backward direction where the backward propagated SHG signal is reflected by the DM, filtered by a SHG filter, and finally collected by another PMT.

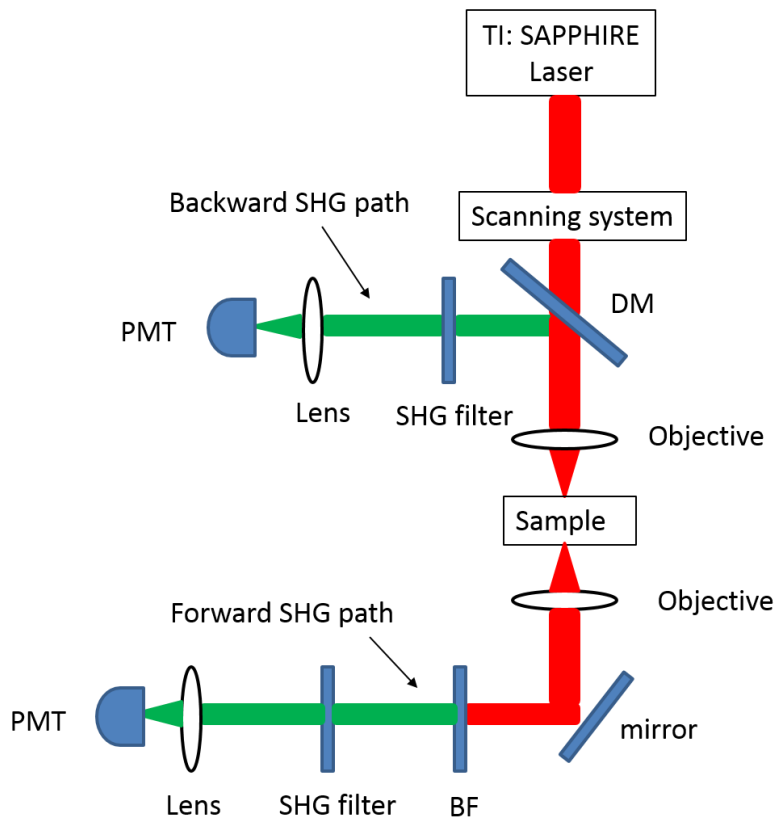


Figure 1.3 Experiment setup of a typical SHG microscopy.

The resolution of SHG is similar to that of TPEF. The full width half maximum (FWHM) transverse resolution is given by [31]

$$w_t = \frac{\sqrt{2 \ln 2} \times 0.325 \lambda_{ex}}{NA^{0.91}} \quad (1.1)$$

while the axial resolution is

$$w_z = \sqrt{2 \ln 2} \times 0.532 \lambda_{ex} \left[\frac{1}{n - \sqrt{n^2 - NA^2}} \right] \quad (1.2)$$

where n is the refractive index of the immersion fluid, and λ_{ex} is the excitation wavelength. For example, a water immersion objective of $NA=0.8$ and $\lambda_{ex} = 800$ nm gives transverse and axial resolution of 400 nm and 1800 nm.

Conventional SHG microscopy utilizes photons in the near infrared wavelength range because the absorption of biological tissue is low in this range. Therefore, it allows for a deeper penetration depth. Depths as large as 1000 μm in brain tissue have been imaged using SHG microscopy [32].

Regarding the maximum optic power shed onto the tissue, it varies among different tissue species. Although the SHG mechanism itself does not require the molecule absorption of photons, once the high intensity excitation beam is focused onto the tissue, there is an unavoidable absorption of the photons, which can cause photo-thermal effects. Hence, it is necessary to keep the power as low as possible if there is enough SHG collected. Our observation and some literatures suggest that tissues such as tendon can withstand optic power as high as 50 mW without visible damage [33].

In the excitation path of SHG microscopy, a half-wave and quarter-wave plate combination is sometimes used to control the polarization of the laser at the focal plane.

Furthermore, Glan-Laser polarizers may be put in the collection paths for analysis of the SHG signal polarization [34]. In addition to the intensity characteristics, the SHG signals have well-defined polarization pattern with respect to the laser polarization and specimen orientation [35]. It can be used to determine the absolute orientation of the protein molecules in the tissue, as well as the degree of organization of proteins in tissues [36]. By incorporation of the polarization sensitivity, it is possible to identify the different molecular sources of SHG based on their susceptibility [37, 38]. In the last a few years, this technique has been used to study biomedical problems such as breast cancer and pathological skin states [39, 40]. Characterization of muscle and engineered tissue has also been performed [41, 42].

The advantages of SHG microscopy include: (1) no exogenous staining necessary; (2) deeper imaging depth; (3) less photo-thermal effect; (4) intrinsic 3D sectioning ability; and (5) containing phase and polarization information. Meanwhile, the limitations include (1) significant investment on hardware such as femtosecond laser, high NA objective and fast scanner; (2) weak signal strength due to the small nonlinear susceptibility; (3) the sensitivity to only specific biological tissues which limits its application areas.

1.3 Review of research on SHG from collagen

The current research related to SHG is categorized into two branches depending on the sample category [43, 44]. The first is to use SHG to study the biophysics of membrane structures; the second is to investigate the structural protein arrays such as collagen (either in natural tissues or in self-assembled structures) and myosin in muscle. In this dissertation, we focus on the SHG from collagen.

The first practical SHG imaging on biological samples was reported by Freund et al., in which the polarity of the fiber bundle in a rat tail tendon was investigated [45]. Some other reported applications include visualizing collagen, myosin and muscle [30]. Other than morphological imaging, quantitative analysis based on SHG images has also been developed. There are several image analysis methods specific to SHG such as second harmonic to auto-fluorescence aging index of dermis (SAAID), tumor-associated collagen signatures (TACS) and Fourier transform-second-harmonic generation (FT-SHG) [46-48].

There are many areas of study on SHG in collagen. In the next, we will review a few areas that are more relevant with the studies in this dissertation, which are the characteristics and mechanism of backward SHG in collagen tissues.

1.3.1 SHG imaging in forward and backward directions

Due to the coherent nature of SHG, a stronger forward SHG intensity than backward intensity is expected. Therefore, transmission detection in the forward direction and sectioned tissue slides are commonly applied in *ex vivo* imaging at early years [23, 49]. However, for practical *in vivo* imaging and eventually medical use, backward detection is more useful. Due to the coherent nature, there are significant feature differences between them.

Légaré et al. compared the difference between forward and backward SHG images from a same sample. In Fig. 1.4, forward and backward SHG images from a thin section of Achilles tendon with $\sim 10 \mu\text{m}$ thickness are shown [50]. In the forward image, a continuous sheet of parallel collagen fibrils is observed while in the backward image, though the general parallel sheet like feature is still observed, the fibrils are not continuous. Instead, heterogeneous features are more obvious. In another publication, Nadiarykh et al. found that similar behavior occurs in

Valonia, a type of cellulose [51]. It was also seen that backward detection images revealed smaller and segmented fibrils while the forward detection images were more continuous. Williams et al. attributed it to the interference among local thickness or density variation because they found that mature (thicker) fibrils were identical in the two detection directions but immature (thinner) fibril segments scatter prominently in the backward [52]. Due to the regularity of the periodic structure of collagen, its spatial distribution and size of the fibrils are considered to be a reason for the different directionality among different tissue types. The fibrils act like phase antennas that can control the directionality of the radiation pattern. This has been first described by Mertz et al. for an inhomogeneous distribution of scatters [53]. For further investigation of this interference issue, the F/B intensity ratio can be used because it assesses the axial size of fibrils in the focal volume.

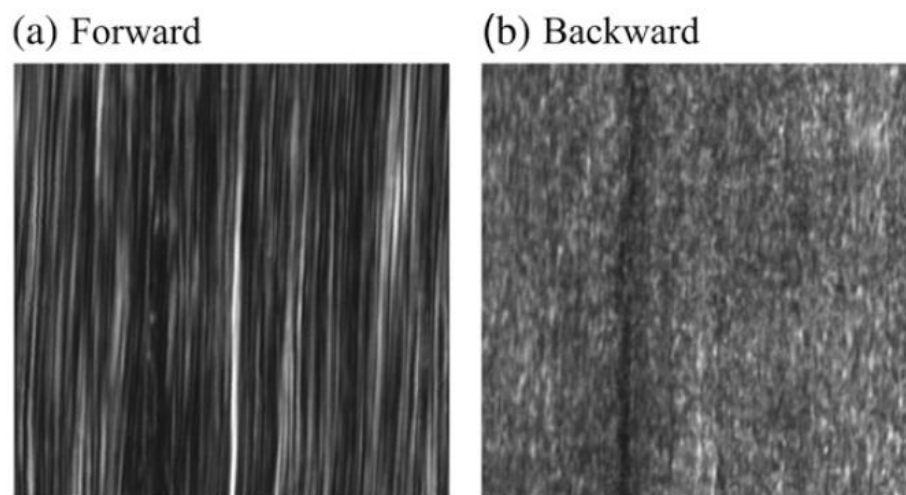


Figure 1.4 SHG images of a thin section of Achilles tendon (a) forward image (b) backward image. From © F. Legare, C. Pfeffer, and B. R. Olsen, “The role of backscattering in SHG tissue imaging”. *Biophysical journal*, 2007. 93(4): p. 1212-1320. Page 1214. By permission from publisher.

1.3.2 SHG directionality

The nature of SHG directional components has received important attention in recent years. In uniform materials such as crystals there is essentially no backward propagating component due to the phase matching limitation which will be discussed in Chapter 2. Similarly, if the collagen fibril thickness is longer than the coherence length in the backward direction, the backward SHG intensity is not likely to be comparable with the forward SHG intensity. However, in collagen fibrils, it has been shown that the backward component is on the order of 10 ~ 100% of the forward component in different tissue types [54, 55]. For example, tendon collagen fibrils with diameter ~ 200 to 300 nm, are measured with unity F/B ratio. Forward and backward SHG intensity are comparable from sclera, which is also with a diameter about a few hundred nm [56].

As specific examples of the effect of fibril spatial distribution, tendon tissue which is highly ordered with thick fibrils gives a large forward component, whereas skin which is less ordered with smaller fibrils gives comparable forward and backward components [57]. It was reported that the F/B ratio has been used to differentiate between different types of collagen. For example, type I collagen, which is crystalline, produces large F/B while Type III and IV collagens, which are less crystalline produce smaller F/B [40].

Besides spatial distribution, another observation about the emission directionality is that F/B has been ascribed to fibril size [58]. Han et al. compared fibrils in cornea and sclera [56]. Corneal collagen fibril is about 30 nm, while fibril in sclera is about one magnitude larger than that in cornea. According to the authors, the backward SHG for cornea is weak since fibril bundles are parallel arranged so that destructive interference reduces their intensity; while the backward SHG for sclera is comparable to forward SHG because the fibrils are randomly arranged. In another work, Chu et al. measured the thickness of single fibril using AFM and

found a linear relationship between fibril thickness and F/B ratio in collagen matrix from bovine skin [58]. They also pointed out that forward signal revealed fiber bundle size and direction and backward signal contained information about the level of submicron structure heterogeneity.

Despite these quantitative observations and measurements, how to interpret the SHG from tissues rich in collagen type I is still very challenging. A thorough description about SHG generation is needed in order to elaborate the backward SHG from collagen structure.

1.3.3 Current models interpreting SHG from collagen

Several models have been proposed in order to explain the significant backward generated SHG from collagen tissues. Williams et al. attribute the SHG from a thin surface layer with tens of nanometers thickness, which reduces the interaction length in the collagen so that it is comparable with the coherence length for backward SHG [52]. As supporting evidence, Fig 1.5 reveals the hollow tube appearance of resolvable fibrils. However, this model only addresses the SHG from a single fibril. Collagen tissues are composed of a large number of fibrils. As a coherence process, the interaction of the SHG generated from single fibrils can dramatically affect the total SHG within the focal volume of the imaging system. Thus, this model can't explain the interaction between fibrils.

Another explanation stems from the fact that type I collagen fibrils usually form highly organized quasi-crystalline structures. It has been recognized that biological world has evolved a vast range of such systems serving as a way to manipulate light transmission and colorful appearance [59]. The emission directionality depends on not only fibril size but also packing density and order of the fibril structure. LaComb et al. relate the different phase mismatch Δk in the forward and backward directions to the fibril diameter and packing under the framework of

quasi-phase matching (QPM) theory [60, 61]. QPM achieves efficient phase matching by correcting relative phase at regular intervals on the basis of a periodic structure built into the nonlinear medium [62]. However, the authors only provide a heuristic treatment but how the Δk is related with the actual fibril structure is not explained.

Later on, Tian et al. discussed about the effect of additional wave vector by lattice structure on optimum backward SHG under a dipole model framework [61]. Although very intuitive, the dipole method lacks a physical insight into the problem and has some unsolved problems such as the selection of dipole size. In addition, the underlying assumption behind dipole model is that the generated SHG photon does not interact with the surrounding fibrils, which is not strict.

Although those models can explain some properties of SHG in collagen, they still have serious limitations and there are also significant differences among the models. Currently there is still a lack of systematic way of explaining the mechanism of backward SHG. In addition, there is a lack of experiment approach to validate the proposed inter-fibril mechanism.

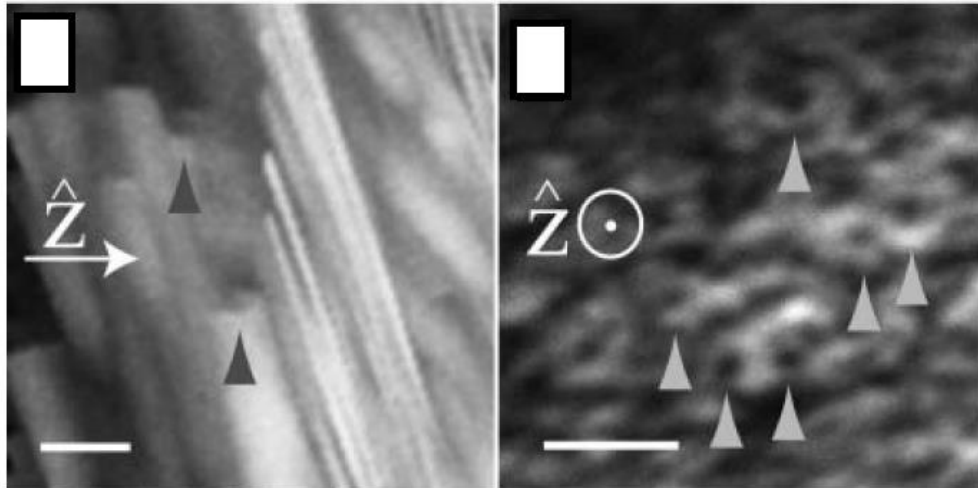


Figure 1.5 High resolution images revealing the hollow tube appearance of thick fibrils which can be resolved by SHG microscopy. The hollow cores are marked by arrows. From © R. M. Williams, W. R. Zipfel, and W. W. Webb, “Interpreting second-harmonic generation images of collagen I fibrils”. *Biophysical journal*, 2005. 88(2): p. 1377-1386. Page 1381. By permission from publisher.

1.4 Objectives and contributions

Backward detection of SHG is especially important for imaging thick tissues and tissues *in vivo*. However, there is a lack of clear understanding about the mechanism of backward SHG in collagen due to the large phase mismatch between the excitation and SHG waves.

The objective of this work is to study the SHG from collagen, especially the backward SHG. Several properties of backward SHG are characterized, including its intensity dependence on excitation wavelength, and back scattering of SHG in collagen tissues. Those studies shine light on the understanding about the backward SHG. We further investigate QPM in collagen in a systematic way and find its relation with fibril organizations, to study the mechanism of phase matching for the backward SHG in collagen tissues.

In order to investigate the wavelength dependence of backward SHG, or SHG excitation spectrum for short, we evaluate the system factors that may affect the wavelength dependence measurement and validate our calibration method. For quantifying the backward scattering of SHG, its contribution among the total backward SHG is measured by a non-invasive method based on confocal microscopy technique. We also introduce a mechanism assisting the backward phase matching of SHG in collagen via solving the SHG intensity in a periodic structure and validate it in experiment.

In the course of achieving the objectives, the main contributions I made include: (1) developed a calibration method for SHG excitation spectrum measurement and applied it to collagen tissue measurements; (2) identified the sources of backward collected SHG and quantified them by a method with pinholes; (3) investigated quasi-phase matching mechanism for generating backward SHG in collagen tissues in theory, simulation and experiment.

1.5 Outline

The dissertation is organized as follows:

In Chapter 2, we review the theoretical background of classic SHG from bulk material and the phase matching of SHG.

In Chapter 3, we calibrate system factors that may potentially affect the measurement accuracy of the SHG excitation spectrum, including pulse width, polarization, and transmission of the optic components. A reliable calibration is performed by measuring the wavelength dependence of SHG signal from a BaB_2O_4 (BBO) crystal. With a match between theoretical and experiment results of the wavelength dependence of SHG in BBO crystal, we establish a reliable method to validate the wavelength dependent SHG measurement over a broad wavelength range.

Based on the calibration, SHG excitation spectra from different types of collagen tissues are investigated.

In Chapter 4, to work toward the goal of investigating the backward scattering of SHG, we study the backward SHG in mouse tissues with a confocal multiphoton microscopy system. A non-invasive method is developed to quantify the proportion of BG-SHG among the total backward SHG.

In Chapter 5, we investigate the effect of periodic structure on backward SHG. We hypothesize that the lattice structure of collagen provides a virtual momentum to assist the phase matching of backward SHG. From theory, simulation, and experiment aspects, we analyze the relation between excitation/emission angles and the optimized excitation wavelength of SHG, which is a direct result and validation of the structure assisted backward phase matching.

Finally, Chapter 6 discusses and summarizes our investigations and presents suggestions for future work.

Chapter 2: Classic theory of second harmonic generation

In this chapter, theoretical background of classic SHG theory is presented. It is found that the conventional phase matching cannot provide efficient generation of backward second harmonic wave in collagen.

2.1 Nonlinear polarization

Nonlinear optics deals with the interaction between optical fields in a nonlinear medium. In contrast to the case that the medium is treated linearly, and the properties of the medium such as refractive index and absorption coefficient are independent of intensity, such nonlinear interaction between fields and material usually does not happen under low optical intensities. Nonlinear optical processes are observed only after the advent of lasers, which could provide the required high intensities to excite the nonlinear effects. As soon as the first laser had been built, Franken et al. demonstrated that shining deep-red pulses of ruby laser light through a quartz crystal produced ultraviolet light, the second harmonic of the original light [63].

In the case of linear optics, the induced polarization $P(t)$ depends linearly on the electric field strength $E(t)$ in a manner that can often be described by [64]

$$P(t) = \epsilon_0 \chi^{(1)} E(t) \quad (2.1)$$

The $\chi^{(1)}$ is known as the linear susceptibility and ϵ_0 is the permittivity of free space. However, under high intensities the medium properties become intensity dependent, and as a result the medium acts as a mediator for interaction between optical fields. The optical response

can be described by generalizing Eq. (2.1) via expressing the polarization $P(t)$ as a power series of the field strength $E(t)$ as

$$P(t) = \varepsilon_0[\chi^{(1)}E(t) + \chi^{(2)}E^2(t) + \chi^{(3)}E^3(t) + \dots] = P^{(1)}(t) + P^{(2)}(t) + P^{(3)}(t) + \dots \quad (2.2)$$

The quantities $\chi^{(2)}$ and $\chi^{(3)}$ are known as the second and third order nonlinear optical susceptibilities, respectively. Here $P(t)$ and $E(t)$ are vectors, $\chi^{(1)}$ is a second rank tensor, $\chi^{(2)}$ is a third-rank tensor and so on. For simplicity, we have taken the $P(t)$ and $E(t)$ to be scalar quantities in writing Eq. (2.1) and (2.2), which is a typical way to express different orders of nonlinearity in previous literatures such as in Ref. 64. For a more rigorous tensor expression, please also refer to Re. 64 as well. In Eq. (2.2), $P^{(2)}(t)$ is referred as the second order nonlinear polarization which gives rise to nonlinear effects such as SHG and sum/difference frequency generation.

More specifically, the second order polarization is given by

$$P_i^{2\omega} = \chi_{ijk}^{2\omega} E_j^\omega E_k^\omega \quad (2.3)$$

Where the subscripts denote Cartesian components and superscripts denote the relevant frequencies. The second order nonlinear optical susceptibility $\chi_{ijk}^{2\omega}$ is a $3 \times 3 \times 3$ third-rank tensor, whose elements sum up to zero for materials with inversion symmetry. Physically, this means that the ability to generate second harmonics is peculiar to molecules which are not centrosymmetric.

In order to produce appreciable SHG, a material must be non-centrosymmetric over macroscopic distances. SHG signal is therefore restricted to certain types of molecules which show non-centrosymmetric characteristics over macroscopic distances such as collagen, microtubules and myosin, among which, collagen type I is most abundant in higher vertebrates

[9]. SHG also takes place at interfaces where there is a large difference in refractive index, such as in a surface, but this type of surface SHG is not within the scope of this dissertation.

2.2 SHG in bulk material

The classic theory of SHG in bulk material is briefly described here as a knowledge background for the thesis. The wave equation describing the SHG process is [65]

$$\nabla^2 E_2 - \frac{n^2}{c^2} \frac{\partial^2 E_2}{\partial t^2} = \mu_0 \frac{\partial^2 P^{NL}}{\partial t^2} \quad (2.4)$$

where n , c , μ_0 are the refractive index, speed of light in vacuum, and vacuum permeability.

Denoting the tilde E_1 as complex field of fundamental excitation, A_1 as the slowly varying amplitude and k_1 as the wave number, the nonlinear polarization can be written as

$$\tilde{P}^{(2)}(\omega_2) = \epsilon_0 \chi^{(2)} \tilde{E}_1^2 = 2d_{eff} \tilde{E}_1^2 = 2d_{eff} A_1^2 e^{-i2k_1 z} \quad (2.5)$$

where d_{eff} is the effective value of the second order susceptibility. The nonlinear polarization for SHG is in the form

$$P^{NL} = \tilde{P}^{(2)}(\omega_2) e^{i\omega_2 t} + c.c. \quad (2.6)$$

Similarly, the SHG electric field is

$$E_2 = A_2 e^{-i(k_2 z - 2\omega_2 t)} + c.c. \quad (2.7)$$

Substituting the expressions about P^{NL} and E_2 into the nonlinear wave equation, neglecting the complex conjugate part, and integrating over the length L of the nonlinear medium, we get

$$\left(\frac{\partial^2 A_2}{\partial z^2} + 2ik_2 \frac{\partial A_2}{\partial z} - A_2 k_2^2 + A_2 \frac{n_2^2 \omega_2^2}{c^2} \right) e^{-i(k_2 z - \omega_2 t)} = -2d_{eff} A_1^2 e^{-i2k_1 z} e^{i\omega_2 t} \omega_2^2 \quad (2.8)$$

$$A_2 = \frac{d_{eff} A_1^2 \omega_2^2 L}{2ik_2} e^{-\frac{i\Delta k L}{2}} \text{sinc}\left(\frac{\Delta k L}{2}\right) \quad (2.9)$$

From Eq. (2.8) to Eq. (2.9), the slowly varying amplitude approximation applies. The intensity is given by

$$I_{SHG} = \frac{|A_2|^2}{2\eta} = \frac{|A_2|^2}{2\sqrt{\frac{\mu_0}{n_2^2 \epsilon_0}}} = \frac{d_{eff}^2 c^2 I_1^2 \omega_2^2 L^2}{2n_1^2 n_2} \text{sinc}^2\left(\frac{\Delta k L}{2}\right) \quad (2.10)$$

η is the optical impedance in a nonmagnetic material. The SHG intensity peaks at $\Delta k L/2=0$, which requires the phase mismatch $\Delta k = 2k_1 - k_2 = 0$. k_1 and k_2 are wave propagation vectors for fundamental and SHG waves respectively.

2.3 Phase matching

In Eq. (2.10), the SHG intensity has a sinc square dependence on the phase mismatch factor Δk . The fundamental and second harmonic waves travel with different velocities determined by the index of refraction at the fundamental and harmonic wavelength. In general, the refractive index of SHG is greater than that of the fundamental because of the normal dispersion in the material, so that the fundamental and second harmonic wave travel at different phase velocities. Since the transfer of power flow from one wave to the other is determined by the relative phase between the waves, the continuous phase change caused by the different phase velocities leads to an alternation in the direction of the flow of the power transfer. Therefore, SHG is produced efficiently until $\Delta k L/2 = \pi$. The distance over which the relative phase between the two waves changes by π is the coherence length which is the half period of the growth and decay cycle of the second harmonic. The coherence length L_c of SHG is defined as

$$L_c = \frac{\pi}{|\Delta k|} = \frac{\lambda}{4|n_{fundamental} - n_{SHG}|} \quad (2.11)$$

Smaller Δk translates to longer L_c . Longer L_c allows a longer interaction length L , which in turn allows for higher SHG intensity. With a non-perfect phase matching condition, where $\Delta k \neq 0$, the SHG intensity is much weaker.

In one dimension, the phase mismatch equals to $\Delta k_f = 2k_1 - k_2 = |2k_1| - |k_2|$ for forward SHG, in which k_1 and k_2 propagate in the same direction. For backward SHG, the phase mismatch equals to $\Delta k_b = 2k_1 - k_2 = |2k_1| + |k_2|$, because k_1 and k_2 propagate in the opposite direction. As we can see, the phase mismatch in the backward direction is much larger than that in the forward direction, which greatly reduces the backward coherence length in the medium. Fig. 2.1 is a plot of the normalized SHG intensity versus normalized phase mismatch $\Delta k_b L / 2\pi$. For reader's reference, we mark three different lengths $L = 30, 120$ or 1500 nm. As we can see, the length L longer than the coherence length (~ 70 nm) produces much lower SHG intensity.

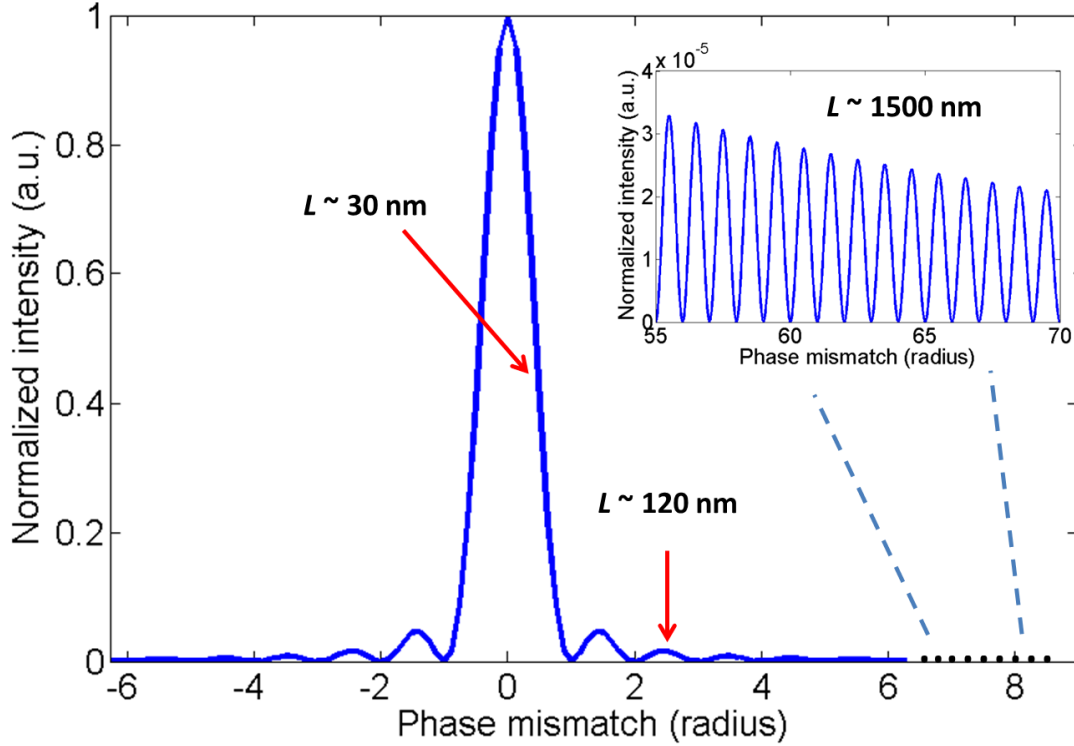


Figure 2.1 Normalized SHG intensity versus normalized phase mismatch $\Delta k_b L / 2\pi$. The intensities for three different lengths L are marked. The refractive indices for excitation and SHG waves n_1, n_2 are 1.35 for simplicity and excitation wavelength is 800 nm.

Phase matching can be achieved by means of birefringence in an anisotropic material when the phase mismatch is relatively small [66]. Another method for enabling efficient growth of the harmonic wave is quasi-phase matching which involves repeated inversion of the relative phase between the fundamental and second harmonic wave [62]. One way to invert the phase is to change the sign of the nonlinear coefficient via inverting the optical axis of a ferroelectric material periodically. For example, in one dimension, when the second order susceptibility $\chi^{(2)}$ is spatially modulated at a frequency Q , the d_{eff} becomes [64],

$$d_{eff}(z) = d \exp(-iQz) \quad (2.12)$$

The phase matching condition in this case becomes,

$$\Delta k = 2k_1 - k_2 - Q \quad (2.13)$$

Perfect phase matching is obtained when $Q = 2k_1 - k_2$. From the point view of physics, the periodic structure produces grating effects and provides a virtual momentum to assist the phase matching. This leads to constructive interference in a certain direction. By the mechanism of quasi-phase matching, efficient SHG can be generated over a relatively long distance or when the phase mismatch is relatively large.

More discussions about the phase matching of SHG, especially backward generated SHG in collagen tissues can be found in Chapter 5, where we show that the mechanism of quasi-phase matching can assist backward generated SHG in collagen tissues.

Chapter 3: Measuring the wavelength dependence of SHG and calibrating with a BaB₂O₄ crystal

In this chapter, the wavelength dependence of backward SHG from collagen tissues is investigated. The results imply that there may exist a phase matching mechanism performing wavelength selection.

3.1 ¹Introduction

The wavelength dependence of SHG intensity from collagen-rich tissue is an optical property that is not fully understood yet. The SHG intensity depends on both phase matching and nonlinear coefficient β . Hall et al. used a two-step model to estimate the wavelength dependence of β and compared it with experiment measurements [67]. In both experiment and theoretical model, within the wavelength span from 750 to 950 nm, the β drops down by no more than five times. However, the variation of phase mismatch over wavelength is not clear because measurement results of the wavelength dependence of SHG intensity are not consistent [68-72]. In Chapter 5, the peak wavelength of the excitation spectrum of the SHG may indicate the phase matching information including lattice distance between fibrils and the excitation/emission angles. An accurate determination of the peak wavelength shift is therefore a key to validate the phase matching mechanism of backward SHG when the excitation/emission angles are varied.

¹ A version of chapter 3 has been published as Shen M., Zhao, J., Zeng, H., and Tang, S. (2013), *Calibrating the measurement of wavelength dependent second harmonic generation from biological tissues with a BaB₂O₄ crystal. Journal of Biomedical Optic.* Edits have been made to better meet the requirements of the journal.

As for the wavelength dependence of SHG from collagen, several publications presented different experimental results so far [68-72]. In Ref. [71], for collagen type I and III gel and rat tail tendon, with the excitation wavelength increasing from 740 to 960 nm, the SHG intensity was found to decrease monotonically by as much as 20%. In [72], experimental studies on an organotypic real architecture for 3D tissue (RAFT) model (containing collagen) indicated that the SHG intensity had an oscillation pattern with maximum at 800 nm excitation. In [69], the authors observed similar oscillation pattern that peaked at 840 nm excitation for mouse skin. Ref. [70] showed four maxima of comparable intensities at 845, 880, 895, and 915 nm from a rat tendon cryosection and a bovine Achilles tendon measured in a backscattered geometry. Recently, more tissue types and tissue engineering scaffolds were measured in [68]. It was found that polymer scaffold SHG peaked at around 840 nm excitation while bovine tendon collagen SHG tended to increase monotonically from 740 to 1000 nm. The authors also reported that the effect of fixation on bovine tendon shifted the SHG excitation peak from 1000 nm to 840 nm.

From the above references, there are conflicting and controversial results on the wavelength dependent SHG obtained by different research groups and among different tissue types. Part of the inconsistency could be due to the lack of a standard calibration and validation method. SHG depends on various factors such as the pulse width and polarization of the incident beam. For example, the SHG signal is inversely dependent on the pulse width. In addition, the way the dipole lies along the symmetry axis of the collagen may suggest how the SHG signal depends on laser polarization. Therefore, a calibration of these parameters is essential for a fair comparison among multiple wavelengths. On the collection side, transmission of the collection system and detector response can also vary over a broad wavelength range. In the above references, transmission/detector response calibration was executed either by a standard

calibration lamp [72] or by standard fluorophores such as tryptophan in water and quinine sulfate in perchloric acid [69], but the calibration methods were not described in detail. In many of the other above references, calibration methods were not mentioned. Therefore, a detailed investigation about calibration method is necessary for carrying out investigations about wavelength dependent SHG in biological tissues. In addition, there has been no report on a standard sample that can be used to validate the accuracy of the calibration methods.

In this chapter, we will discuss the important factors that affect wavelength dependent SHG. Details about how to verify those effects and perform system calibrations will be described. We perform validation for our wavelength dependent measurement by measuring the wavelength dependence of SHG from a standard BaB_2O_4 (BBO) crystal and comparing it with theoretical calculations. For plane wave incidence, SHG intensity drops down quickly when the excitation wavelength deviates away from the designated phase matching wavelength determined by the angle cut of the BBO crystal. However, in the tight focusing condition, strong SHG intensity can be excited over a broader range of excitation wavelengths because the focal length ($\sim 1\text{-}2\ \mu\text{m}$) is even shorter than the coherence length of the SHG process ($\sim 10\ \mu\text{m}$). Hence, we can utilize this effect to obtain strong SHG over a wide wavelength range and further use it as a standard to examine the accuracy of wavelength dependent SHG measurement in tissues because the results from BBO can be predicted by theory. Besides the verification purpose, another aspect of investigating the SHG from BBO crystal is that it is relatively easy to understand what factors affect its SHG wavelength dependence from the nonlinear coupled equation describing it, which further help us understand the wavelength dependence in biological tissues. Two typical patterns of wavelength dependence spectra from mouse tail tendon and Achilles tendon are given in the end.

3.2 Material and methods

3.2.1 SHG power expression from BBO crystal

Due to the dispersion of BBO, it is not possible to achieve phase matching unless its birefringence property is utilized. BBO has two independent refractive indices $n_o(\lambda)$ and $n_e(\lambda)$, which are termed as ordinary and extraordinary refractive index respectively. The electrical field $E(\lambda)$ that propagates according to $n_o(\lambda)$ is orthogonal to the optic axis. Otherwise, it follows $n_e(\theta, \lambda)$ which is a function of the angle between the incident beam and the optic axis [64]

$$n_o^2(\lambda) = 2.7359 + \frac{0.01878}{\lambda^2 - 0.01822} - 0.01354\lambda^2 \quad (3.1)$$

$$n_e^2(\lambda) = 2.3753 + \frac{0.01224}{\lambda^2 - 0.01667} - 0.01516\lambda^2 \quad (3.2)$$

$$\frac{1}{n_e^2(\theta, \lambda)} = \frac{\cos^2 \theta}{n_o^2(\lambda)} + \frac{\sin^2 \theta}{n_e^2(\lambda)} \quad (3.3)$$

By adjusting the angle θ , the phase matching condition $\Delta k = 2\pi[n_o(\lambda) - n_e(\theta, \lambda/2)]/\lambda = 0$ can be satisfied for a certain excitation wavelength. Only when Δk is zero, the energy from the fundamental wave can be efficiently transferred to the SHG wave. For the BBO used in this experiment, the angle between surface normal and optic axis is 29.3 degree which helps achieve phase matching for excitation wavelength at 800 nm. In Fig. 3.1 (a), we plot how the Δk varies with excitation wavelength. When excitation wavelength is shorter than 800 nm, Δk is negative; while Δk is positive when the excitation wavelength is longer than 800 nm. It is also worth mentioning that the effective nonlinear coefficient d_{eff} depends on the projection of $E(\lambda)$ on each

axis of the $\chi^{(2)}$ nonlinear susceptibility. Therefore, SHG generation efficiency is also related to the polarization of $E(\lambda)$.

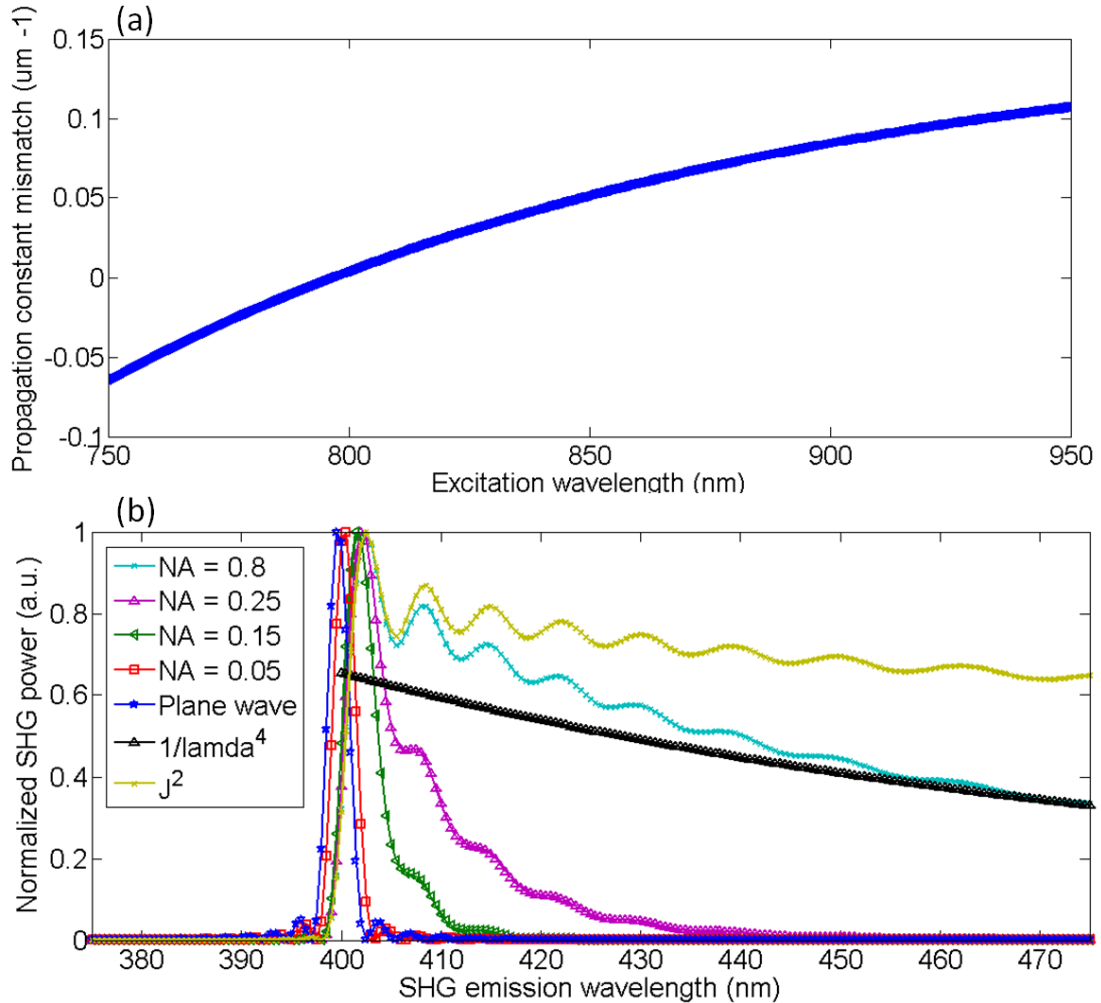


Figure 3.1 (a) Calculated wavelength dependent phase matching in BBO crystal; (b) comparison of calculated wavelength dependent SHG power in different NA situations.

Now we try to deduce how the SHG power varies with excitation wavelength theoretically for both collimated beam and focused Gaussian beam. For the sake of theory and experiment comparison, we will keep quantifying SHG strength by power within the whole chapter. For collimated wave incidence, it is assumed that we can apply the theory based on

plane wave excitation because of its very low NA. The theoretical expression for SHG intensity I_2 for plane wave excitation is given according to [73]

$$I_2 = \frac{8(\chi^{(2)})^2 \omega_2^2 I_1^2}{n_1^2 n_2 \epsilon_0 c^3} L^2 \text{sinc}^2\left(\frac{\Delta k L}{2}\right) \quad (3.4)$$

in which $\chi^{(2)}$, n_1 , n_2 and ϵ_0 are the second order susceptibility, refractive index of excitation fundamental wave, refractive index of second harmonic wave and vacuum permittivity, respectively. ω_2 is the frequency of SHG and c is the speed of light. I_1 is the intensity of fundamental wave, L represents the thickness of the crystal and Δk is phase mismatching. Eq. (3.4) can be converted to the expression of power by using

$$P = \int I 2\pi r dr \quad (3.5)$$

where r represents the transverse distance from center. For a Gaussian beam with finite beam spot as $2\omega_0$, the power of SHG is given by

$$P_2 = \frac{1}{2} \pi \omega_0^2 I_2 \quad (3.6)$$

The beam waist is given by,

$$\omega_0 = \frac{1.27 \times f \times \lambda}{d} \approx \frac{1.27 \times \lambda}{2NA} \quad (3.7)$$

in which d , f and NA are the clear aperture, focal length and numerical aperture of the lens respectively. We are interested in wavelength dependent SHG power when the fundamental power is kept constant. Substituting Eq. (3.4) into (3.6) while neglecting the terms that are not or less wavelength dependent (such as the n_2 , n_1 and $\chi^{(2)}$), we have,

$$P_2 = 16 \left(\frac{2\pi}{\lambda_2}\right)^2 \frac{n_2 (\chi^{(2)})^2 P_1^2 \omega_{02}^2}{\pi n_1^2 \epsilon_0 c \omega_{01}^4} L^2 \text{sinc}^2\left(\frac{\Delta k L}{2}\right) \propto \frac{\text{sinc}^2\left(\frac{\Delta k L}{2}\right)}{\lambda_2^2 \times \lambda_2^2} \quad (3.8)$$

Here ω_{01} and ω_{02} are the beam waist for fundamental and SHG wave respectively. The denominator of the right most expression in Eq. (3.8) consists of a product of two λ_2^2 term. The first λ_2^2 term originates from the time derivative term in the coupled wave equation which indicates that higher frequency oscillation of the SHG dipole will generate stronger nonlinear effect. The other λ_2^2 term is due to the variation of beam diameter with wavelength. If we maintain the fundamental power to be a constant, an increase of the beam waist will result in a decrease of peak intensity because SHG depends quadratically on the peak intensity.

In the tight focusing condition, which reflects the case when a high NA objective lens is used to focus light into the crystal, we first have the expression for the amplitude of SHG as [73],

$$A_2 = \frac{i\omega_2}{2n_2c} \chi^{(2)} A_1^2 J_2 \quad (3.9)$$

where A_1 and A_2 are complex amplitudes of the fundamental excitation and second harmonic wave respectively, and J_2 is an integral from crystal surface z_0 to a certain depth z

$$J_2(\Delta k, z_0, z) = \int_{z_0}^z \frac{e^{i\Delta k z'}}{1 + 2iz'/b} dz' \quad (3.10)$$

The confocal parameter b is defined as $b = k\omega_0^2$. By relating amplitude with intensity

$$I = 2n\varepsilon_0c|A|^2 \quad (3.11)$$

and using Eq. (3.6) and (3.7), we have

$$P_2 = \frac{1}{4} \left(\frac{2\pi}{\lambda_2} \right)^2 \frac{n_2 \left(\chi^{(2)} \right)^2 P_1^2}{\pi n_1^2 \varepsilon_0 c} \frac{\omega_{02}^2}{\omega_{01}^4} J_2^2 \propto \frac{1}{\lambda_2^4} J_2^2 \quad (3.12)$$

From the above derivation, we can see that the wavelength dependence of SHG power depend on not only phase matching but also variation of beam waist for both collimated and focused wave.

Fig. 3.1 (b) shows the SHG power versus wavelength for different NAs of focusing lens. The dispersion property of the crystal is calculated from Eq. (3.1) to (3.3). The SHG power for different NAs are normalized and compared with collimated beam in Fig. 3.1 (b). For collimated beam, since the phase mismatch Δk is critical for a strong SHG emission, the pattern follows a sinc square function that peaks at 400 nm. When the NA is as small as 0.05, its pattern is very similar to that of plane wave except for a peak wavelength shift which will be explained later. It validates our treatment of collimated beam as plane wave. For NA = 0.15 and 0.25, after a steep rise and peak around 400 nm, the emission SHG power decreases slower than in the plane wave case when the excitation wavelength deviates from the phase matching excitation wavelength. One may notice that the peak wavelength in this case is shifted from 400 nm to longer wavelength compared with the plane wave and NA = 0.05 cases. This is because the fundamental wave experiences Gouy π phase shift in the focal region within a length equal to the confocal parameter of the beam, which reduces the effective propagation constant k in the focal volume [74]. Therefore, only if there exists a positive phase mismatch (for the crystal we use, it is generated by excitation wavelength longer than 800 nm), can we achieve perfect phase matching in the focal volume. Otherwise, at the wavelength region that originally we have Δk equal to or smaller than zero phase mismatch, the phase matching condition deteriorates such that the SHG power is greatly reduced. This explains the fast decreasing of SHG power when the excitation wavelength is shorter than the peak wavelength. It is also observed that a uniformly spaced oscillation structure is superposed on the decaying pattern, which originates from the relative phase of a particular excitation wavelength compared with that of the peak wavelength [75]. When the NA is even higher, the SHG power reduces slower with wavelength change than lower NA cases. For example, with NA = 0.8, the SHG power reduces to around 40 % when the

excitation wavelength varies from 800 nm to 950 nm. In order to distinguish the contribution of J_2^2 and $1/\lambda^4$ in Eq. (3.12) to the pattern of NA = 0.8 curve, the wavelength dependence of these two terms are plotted separately. When the excitation wavelength is close to optimum phase matching (corresponding to better phase mismatch), the wavelength dependence is dominated by J_2^2 ; when the excitation wavelength deviates from optimum phase matching wavelength (corresponding to worse phase mismatch), the tail of the oscillating decreasing curve approaches the $1/\lambda^4$ term. These observations will be helpful when we investigate the wavelength dependence of SHG from collagen in later sections.

3.2.2 Experiment setup

Fig. 3.2 is a schematic drawing of the optical layout of the measurement system setup. The light source is a mode-lock titanium-sapphire laser (Chameleon, Coherent, USA) providing wavelength tunable femto-second laser pulse from 720 to 960 nm. A combined half wave plate ($\lambda/2$, 10RP52-2 Newport, USA) and polarization beam splitter (PBS, PBS052 AR600-1000 nm, Thorlabs, USA) module is used for coarse control of the excitation laser power. The fine control of the laser excitation power at different wavelengths is achieved by rotating a variable neutral density filter wheel (ND, NDC-50C-2M-B, Thorlabs, USA). In order to retain the polarization state of excitation light at all wavelengths, a dichroic glass polarizer (POL 1, VISIR 600 – 1200 nm, color Pol, USA) is used. The laser beam is expanded by two lens (L1, L2) with focal length 25 and 250 mm respectively so that the back aperture of the objective lens is filled, after which the laser beam is cast onto the sample by a 40X (NA = 0.8) objective (OBJ1, LUMPLFLN, Olympus, USA). For comparison purpose, the 40X objective lens can be replaced with a 10X (NA = 0.25) objective (Plan N, Olympus, USA) or completely removed away for collimated

beam excitation. The backward SHG is collected by the same objective and is directed to a spectrograph through a long pass dichroic beam splitter (DM, FF660-Di02, Semrock, USA). The residual excitation fundamental wave is further attenuated by a band-pass filter (FF01-750, Semrock, USA). Another polarizer (POL2) (LPVISE100-A, Thorlabs, USA) is placed before the focusing lens (L3) to examine the polarization state of the SHG signal. The focusing lens has a focal length of 75 mm. The one-meter long multimode fiber (FG200-UCC, Thorlabs, USA) used has a 200 μm core diameter with $\text{NA} = 0.22$. Spectral measurements are obtained with a spectrograph with a resolution of 0.5 nm (SpectraPro-150, Roper Scientific, USA), which is directly coupled to the multimode fiber. The dashed part in Fig. 3.2 is a setup for collecting forward SHG signal which includes a 60X (NA=1.0) objective (LUMPLFLN, Olympus, USA). The rest components are exactly the same as what are used in the backward path.

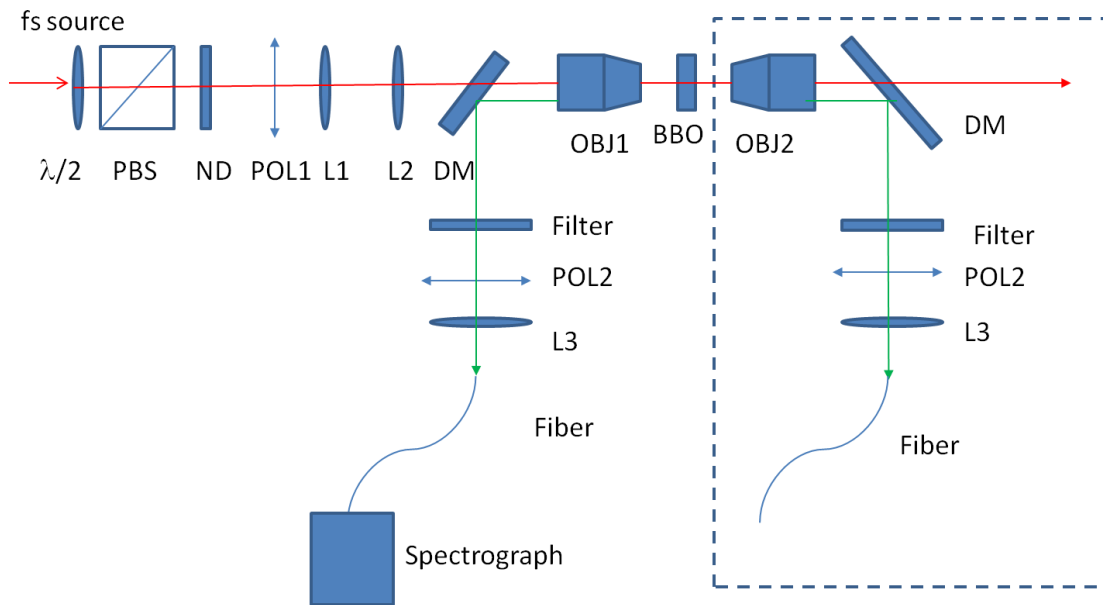


Figure 3.2 Experimental setup for wavelength dependent SHG measurements in forward and backward directions from BBO and mouse tissues.

3.2.3 System factors affecting wavelength dependence

Besides the factors such as phase mismatching and intensity variation, we try to calibrate system factors that may affect the measurements of the wavelength dependent SHG. In the following, we will discuss this issue in the context of using 40X objective lens because it is directly related to our calibration purpose. These factors can be examined in the order of how the SHG signal is generated and collected with four steps.

First, properties of the excitation beam that affect the SHG power should be kept constant for each wavelength. For example, the excitation power under different excitation wavelengths is controlled by rotating the angle of the variable ND filter wheel. The angle of the filter is calibrated for each wavelength so that the excitation power, monitored by a wavelength calibrated silicon-based power meter (S132A 600-1000 nm, Thorlabs, USA), is kept the same after the objective. An auto-correlator (FR 103M, Femtochrome Research, USA) is used to measure the laser pulse width before the objective and the pulse width variation is not significant as shown in Fig. 3.3 (a) assuming a hyperbolic secant pulse shape. As we have mentioned earlier, the polarization of the excitation beam must be kept the same for all the wavelengths because the effective nonlinear coefficient depends on the polarization. By rotating the angle of polarizer POL1 and measuring the laser power after it at different angles at four excitation wavelengths separated by 50 nm as shown in Fig. 3.3 (b), we are able to know that the polarization state of excitation laser before objective is the same for all the wavelengths. If we compare the angle dependent power with a cosine square function which represents a linear polarization, the incident light is confirmed to be linearly polarized.

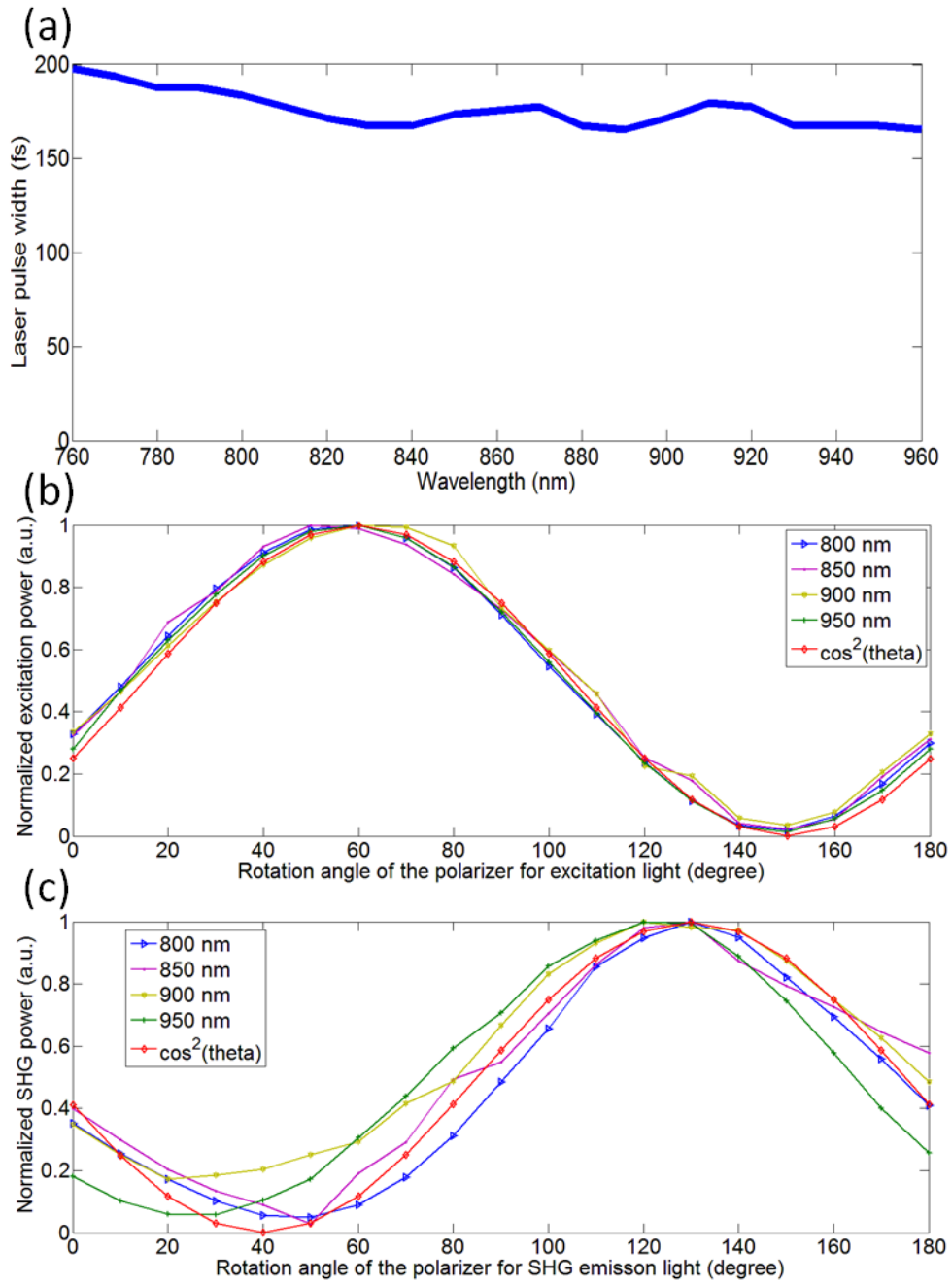


Figure 3.3 (a) Pulse width measurement results before objective lens; (b) Plot of excitation power versus analyzer angle at different wavelengths; (c) Plot of emission power versus analyzer angle at different wavelengths.

Then we need to make sure that all these factors are not altered at the focal spot inside the BBO crystal. The transmission curve of BBO in the 700 to 1000 nm range is quite flat. Therefore, we can reasonably assume that the excitation power is the same for all the wavelengths over the laser tuning range at the focal point [76]. The effect of the group velocity dispersion from the crystal and the objective lens on the pulse width broadening can be calculated by

$$t = \tau_0 \sqrt{1 + \left(\frac{4 \ln 2 D}{\tau_0^2} \right)^2} \quad (3.13)$$

where t is the broadened pulse width, τ_0 is the original pulse width and D is the group velocity dispersion. It is estimated that for a 1 mm-thick BBO crystal and a 40X objective lens, D is roughly 200 fs² and 6500 fs² respectively [77]. Even for a large dispersion such as 6500 fs², the pulse will be broadened by only 10% for 170 fs pulse width, which indicates that pulse broadening effect is not significant for the pulse width we use. Hence, pulse widths for different wavelengths are considered to be the same at the focal point. High NA objectives can affect the polarization state of the excitation beam due to either the anti-reflection coating of the lens or the angle of incidence beam. The polarization state of the excitation beam at the focal point can be examined by analyzing the polarization state of the SHG signal. It is because that the polarization state of the excitation light (o light) and emission light (e light) are orthogonal with each other. Therefore, if the polarization state of the SHG signal is the same for all the wavelengths, the corresponding excitation fundamental wave must have the same polarization state as well. Fig. 3.3 (c) shows the polarization state of the SHG signal by rotating POL2 at excitation wavelengths from 800 to 950 nm at 50 nm step. It is found that they all fit with linear polarization and the peaks are located at the same rotation angle, indicating that the polarization of the excitation and emission beams at the focal point are the same for different excitation

wavelengths. It is noted that the linearity of the polarization of the SHG beam is not as good as that of the excitation beam. Possible reasons include that the emitted SHG signal after high NA objective lens contains multiple angle components, which could deteriorate the linearity of the polarization. The relatively weak signal strength and deviation from designed working wavelength of the POL2 are also possible reasons.

After the SHG signal is generated at the focal point, we must make sure that they are collected equally at different wavelengths. The profile of excitation fundamental beam at the focal point is Gaussian which is described by the confocal parameter b and beam radius ω_0 . For SHG wave, b is the same as the excitation wave, but its beam waist is smaller than that of excitation wave because SHG has a larger propagation constant k . Hence, the divergence angle of SHG wave given by $\arctan(b/\omega_0)$ will be smaller than that of the fundamental wave. It ensures that for either forward or backward transmitted SHG, it will be collected by the objective lenses with same NAs. When the excitation wavelength changes, the confocal parameter b and beam radius ω_0 both change accordingly. However, the angular divergence of the beam, given by $\theta = \lambda/\pi\omega_0$ is the same for all the wavelengths [73]. Therefore, we expect that the collection conditions for SHG at different wavelengths are the same. In the case of SHG from BBO crystal, backward collected SHG comes from the reflection of forward SHG at the interface of crystal and air. When the focal point approaches the interface, more SHG signal will be collected by objective. The focal point in the crystal may vary at different wavelengths due to achromatic aberration, but considering the scale of the variation and the uniformity of the crystal, it is assumed to be not significant in our experiment.

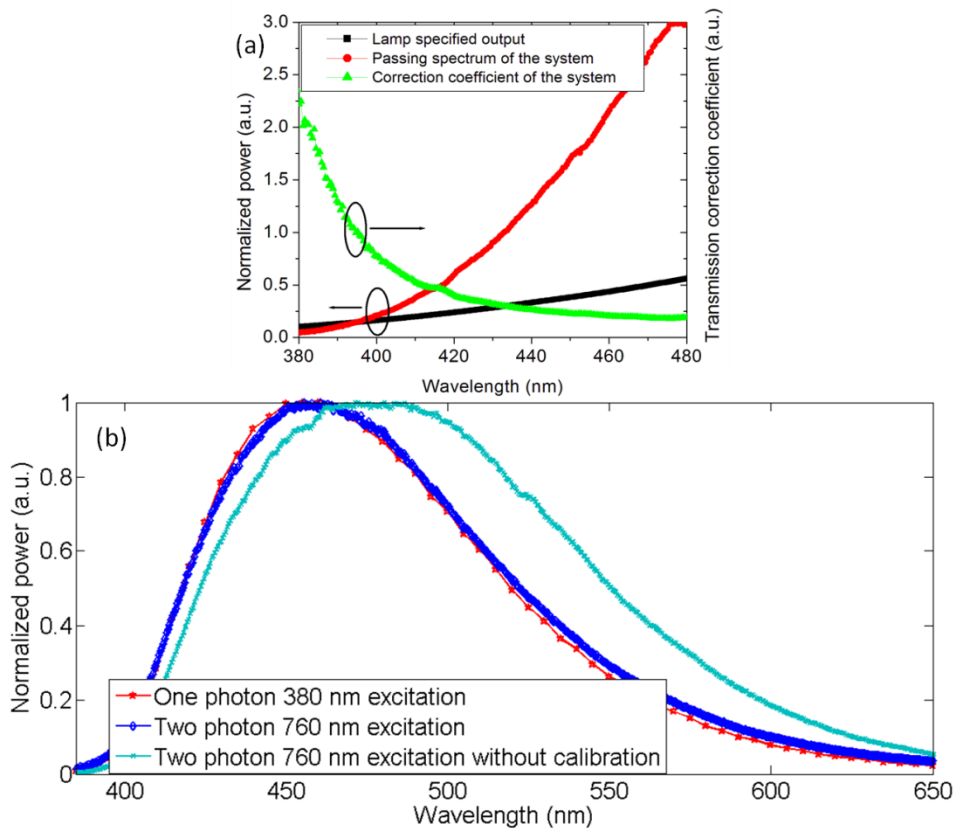


Figure 3.4 (a) Factory supplied NIST traceable spectrum of the standard lamp (black) and the lamp spectrum measured by our optical system (red) with which transmission/detector response correction coefficient is calculated (green); (b) One-photon and two-photon fluorescence emission spectrum for NADH with or without transmission/detector response calibration.

Finally, to fairly compare the SHG signal on the spectrometer at different wavelengths, transmission/detector response calibration for the detection system at different wavelengths is also necessary. One method to apply the transmission/detector response calibration is to divide the factory supplied National Institute of Standard and Technology (NIST) traceable spectrum of a standard intensity calibration lamp by the measured spectrum from the system so that the transmission/detector response correction coefficient of the system is obtained. In order to guide the light from the lamp uniformly to the objective lens, a two-port integrating sphere is used, in

which one port collects the lamp light while the other port transmits the light into the objective. The integrating sphere functions as a diffuser so that light rays from standard calibration lamp are uniformly cast onto the front aperture from all the incident directions. In Fig. 3.4 (a), the black curve represents known output of the lamp and the red curve represents the spectrum measured by the system. The resulting correction coefficient shown by the green curve can be used to compensate for the transmission/detector response at different wavelengths by multiplying it with the raw spectrum of any new measurements by the system. The accuracy of the calibration will dramatically affect the wavelength dependent measurement. Therefore, we verified the correctness of our calibration by measuring one-photon and two-photon fluorescence emission spectrum of a nicotinamide adenine dinucleotide (NADH) sample. It was previously found that one-photon and two-photon fluorescence properties of NADH are the same [78]. Hence, by comparing the one-photon and two-photon emission spectra of NADH, the correctness of transmission calibration can be verified. The one-photon emission spectrum of NADH was measured using a separate spectrofluorometer equipped with two double-grating monochromator [79]. In Fig. 3.4 (b), before calibration, the peak of the two-photon fluorescence emission is at 480 nm, and after calibration the peak is shifted to 450 nm. The overlap of the one-photon and two-photon emission spectra over the whole wavelength range indicates that our calibration method is correct. The results also demonstrate the importance of the transmission/detector response calibration. Similar transmission/detector response calibration is also applied in the forward channel, where the spectral response of the 60X objective lens, collection fiber and spectrometer are included.

3.3 Calibration results

Based on the above procedures for wavelength dependent measurement, the calibrated wavelength dependent SHG from a BBO crystal is measured and plotted in Fig. 3.5. The spectra are first recorded by the spectrometer and then multiplied by the transmission/detector response correction coefficient. The emission spectra for 40X objective, 10X objective and collimated beam are plotted in Fig. 3.5 (a) - (c). Each emission spectrum is further integrated over its wavelength span to get the total SHG power and compared with theoretical calculations. In order to take into account the finite line width of the laser, the theoretically calculated SHG power are averaged over each 10 nm bandwidth based on the spectrum shape. This processing makes the curves less oscillating than those shown in Fig. 3.1 (b). In Fig. 3.5 (d), it is observed that the SHG collected in the backward direction in the three different cases all match well with the theory. For the 40X objective case, some amount of SHG signal is collected below 400 nm despite a prediction of null in theory. This is likely because the angle spread of propagation constant $k(\lambda)$ due to focusing makes it possible to achieve perfect phase matching at wavelengths shorter than 800 nm. It also happens for less tight focusing case such as 10X objective case, but it is absent from the plane wave case. The peak wavelength shift for collimated beam and focused beam is also less obvious in the real experiment case largely due to the fact that the 10 nm laser bandwidth is broader than the peak wavelength shift. It is also seen that the forward and backward collected SHG at NA = 0.8 have similar wavelength dependence trend, which matches with the fact that source of backward collected SHG is purely the reflection of forward SHG. Although surface SHG can be generated from materials like quartz plate, its SHG signal is much weaker than the reflected SHG from BBO crystal and thus surface SHG is not used in this study.

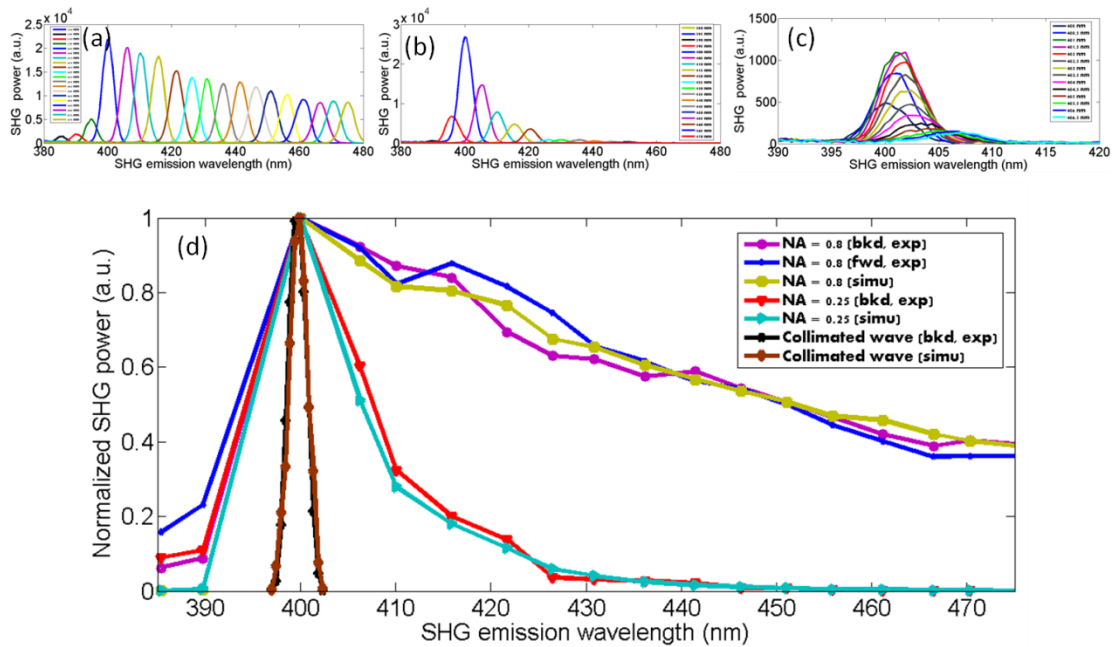


Figure 3.5 Experiment results for wavelength dependent SHG power versus emission wavelength with (a) 40X objective (NA=0.8), (b) 10X objective (NA=0.25) and (c) collimated beam; (d) theoretical and experimental comparison for wavelength dependent SHG power for collimated beam and focused beams.

3.4 SHG excitation spectrum from collagen tissues

With the above calibration method, the experimental system is calibrated for measuring the SHG excitation spectrum from collagen tissues.

We measured the wavelength dependent SHG from multiple mouse tail tendon tissue samples from two freshly sacrificed mice. The results are shown in Fig. 3.6. The measurement is in the backward direction. In each mouse, three pieces of thick tissue samples are excised from its tail, which are cut by a cryostat microtome into 10 μm thickness. Approximately ten slices of 10 μm samples can be obtained from each piece of tissue sample. From a slice, one or two locations can be measured. Due to the large amounts of data, only some representative results are shown here. Each data point is an average of six measurements.

Two typical spectral patterns have been observed in the mouse tail tendon samples. One is that when the excitation wavelength increases, SHG intensity decreases monotonically, while the other is with a single peak. The occurrence of these two types of spectral patterns is similar. In Fig. 3.6 (a), we show the monotonic decreasing spectral pattern from five measurements with a large difference in the dropping down percentage. From short to long wavelength, the SHG intensity drops down from a maximum to a minimum intensity within the wavelength tuning range. For the measurements shown here, the SHG power is observed to decrease with a drop down percentage within the 40-85% range. Fig. 3.6 (b) shows five measurements of the single peak spectral pattern with a large difference in the peak wavelengths. This type of pattern is characterized by a peak wavelength. The five measurements show the peak wavelength within the 830-900 nm range.

Other than the different spectral shapes, the absolute SHG intensities are also different between the two typical patterns. On average, the peak intensities of the single peak spectra are stronger than that of the monotonically decreasing spectra.

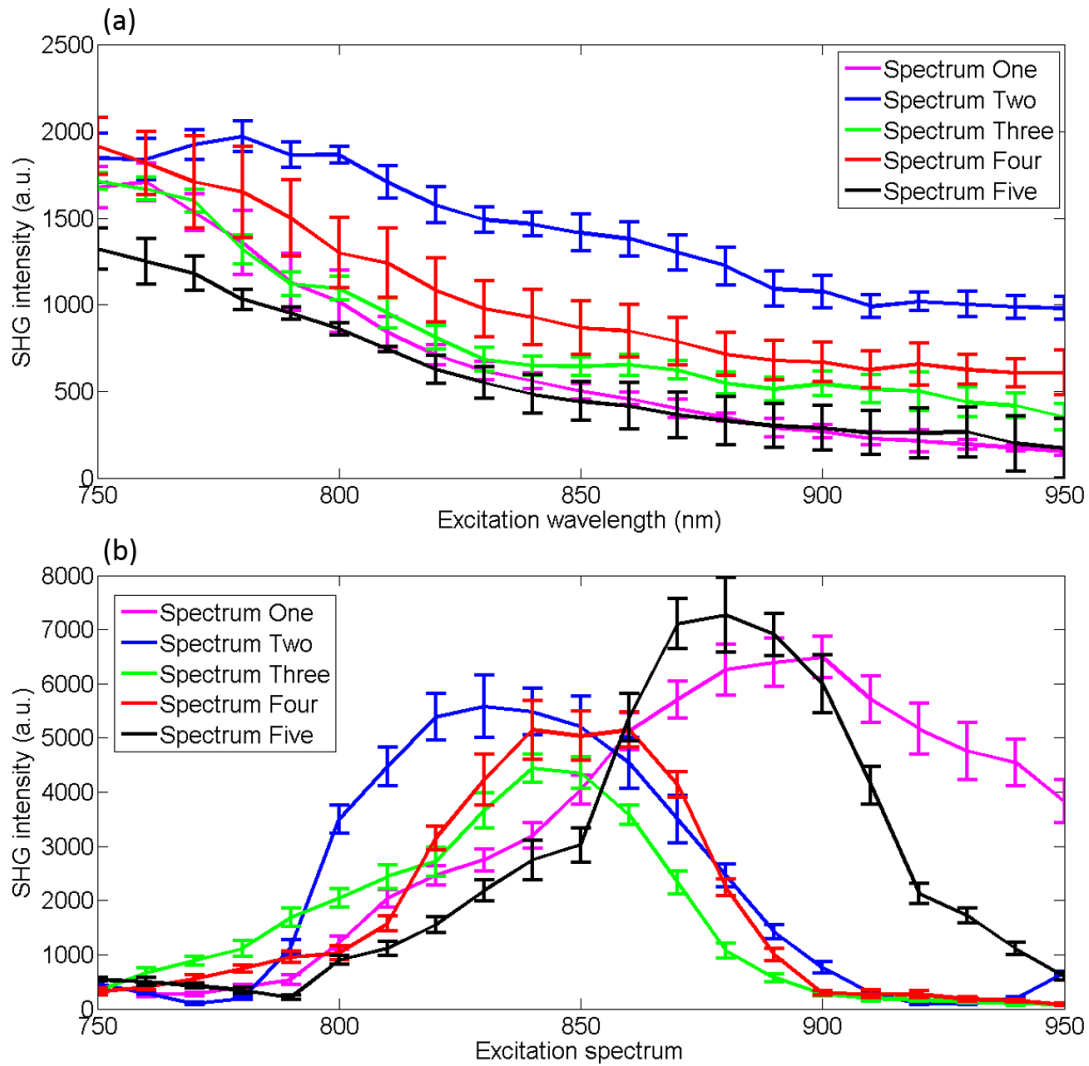


Figure 3.6 Wavelength dependent SHG spectrum from 10 μm mouse tail tendon with two typical spectrum patterns: (a) monotonically decreasing and (b) single peak. For each pattern, five spectra are plotted. The error bar draws the standard deviation of six repeated measurements at a same location.

In Fig. 3.7, representative patterns of spectra originating from 10 μm thin mouse Achilles tendon in the backward direction are shown. Still, there are two types of spectra and their occurrence is even. In the monotonically decreasing spectra category, in Fig. 3.7 (a), from short

to long wavelength, the power decreases approximately by 80% -25 %. For the single peak spectra in Fig. 3.6 (b), the peak wavelength ranges from 770 to 830 nm.

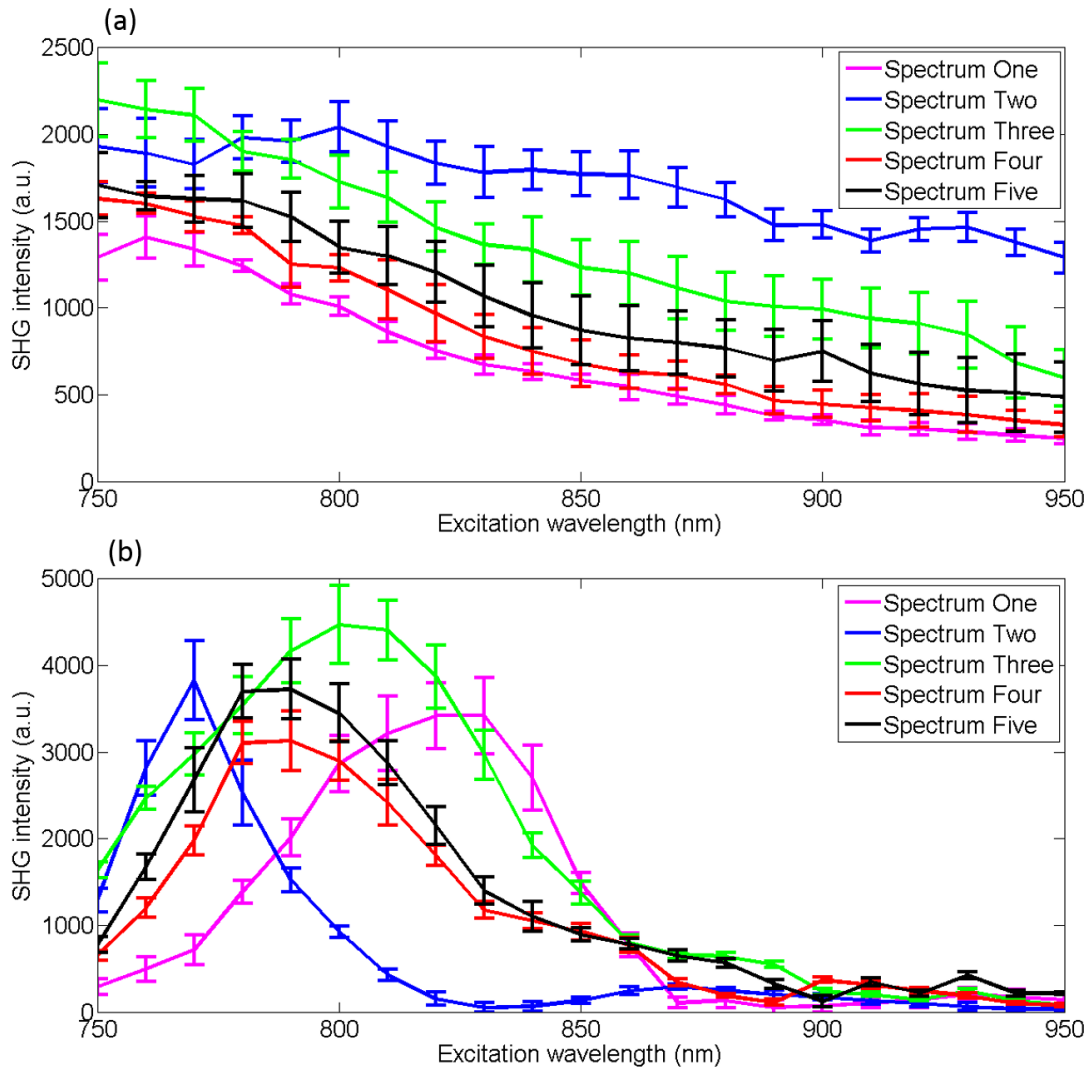


Figure 3.7 Wavelength dependent SHG spectrum from 10 μm mouse Achilles tendon with two typical spectrum patterns: (a) monotonically decreasing and (b) single peak. For each pattern, five spectra are plotted. The error bar draws the standard deviation of six repeated measurements at a same location.

The measurement results show that Achilles tendon has relatively shorter peak wavelength than tail tendon. This peak wavelength difference is perhaps due to either the

variation of fibril diameter or the microstructure of the two tissue types, both of which suggests a connection between wavelength dependence spectrum with the fibril microstructure in the focal volume. In Chapter 5, this connection will be studied under the framework of quasi phase matching.

The two different spectral patterns, namely monotonic decrease and single peak patterns may have been caused by a difference on the phase matching condition due to local variation of collagen microstructure. The current measurement is a single point detection setup, where the variation of local fibril microstructure cannot be avoided. Neglecting the wavelength dependence of nonlinear coefficient, from the perspective of phase matching, the “single peak” spectral pattern shows an optimum excitation wavelength. This implies that the fibrils in the focal volume may form an organized structure that can assist phase matching and perform the wavelength selection. In a location where a monotonic decrease pattern is observed, the wavelength selection is not clear. This may indicate that within those locations, the fibril organization may be more random, which deteriorates the phase matching and wavelength selection condition. The sensitivity of SHG to local collagen microstructure is also the cause of the variation among individual spectrum even within the same pattern group. Current SHG imaging is not sufficient to resolve the microstructure variation of collagen fibrils. The collagen fibril microstructure can be resolved by TEM which requires special processing of the sample. In the future, acquiring SHG and TEM images simultaneously will provide the information about correlation between the SHG properties and collagen microstructure. This structure-assisted phase matching for backward SHG will be discussed in more detail in Chapter 5.

3.5 Conclusions

In summary, the calibration procedures for wavelength dependent SHG measurement are introduced. The accuracy of the calibration procedures is proved by measuring the SHG wavelength dependence in a BBO crystal. The agreement between theory and experiment for the BBO crystal demonstrates that our proposed method can be used as a validation method when investigating the wavelength dependence of SHG from biological tissues. In the end, the wavelength dependence of SHG from mouse tail tendon and Achilles tendon tissues are measured for 10 μm thick samples. It is observed that, there are two typical types of excitation spectra. One is that the SHG power decreases monotonically. The other is that there is a single peak wavelength in the spectrum, where the peak wavelength of Achilles tendon is normally shorter than that of the tail tendon. The variation of the SHG excitation spectrum in different locations and in different tissue types shows that SHG is very sensitivity to the local environment of the fibril microstructure. This is also an indication of the complexity of the phase matching condition in collagen tissues.

Chapter 4: Quantifying the back scattering of SHG

In this chapter, we measure the contribution of backward generated and backward scattered second harmonic wave to the total backward-collected SHG in collagen tissues. Our results show that significant amount of backward collected SHG may arise from the direct generation of backward SHG.

4.1 ²Introduction

SHG imaging in the backward detection geometry is necessary for imaging thick tissues and tissues *in vivo*. While SHG can be generated in both forward and backward directions, scattering from tissues can also change the propagation direction. In this chapter, we are interested in quantifying the backward scattering of SHG from tissues. To this end, it is helpful to clearly define the SHG components collected by the detectors in both directions. In Fig. 4.1, the SHG initiated from the focal point is named as forward generated SHG and backward generated SHG (BG-SHG) according to their generation direction. Due to the existence of tissue scattering, the forward generated SHG might be backscattered and is named as backward scattered forward generated SHG (BS-SHG). The total SHG collected in the backward direction, consisting of BG-SHG and BS-SHG, is simply named as backward SHG (B-SHG). Similarly, in the forward direction, we have forward scattered backward generated SHG and forward

² A version of Chapter 4 has been published as Shen, M., Tian, Y., Chong, S., Zhao, J., Zeng, H., and Tang, S. (2013), *Quantifying the backscattering of second harmonic generation in tissues with confocal multiphoton microscopy*. *Journal of Biomedical Optics*. Edits have been made to better meet the requirements of the journal.

generated SHG. For understanding the issue of SHG signals in collagen tissues, it is interesting to study the contribution of BS-SHG among the B-SHG.

Nadiarnykh et al. qualitatively investigated the scattering issue in cellulose specimens [51]. It was observed that from depths near the tissue surface the backward images displayed small fibrils not present in the forward channel. In addition, at depths beyond one mean free path of scattering, the fibril morphologies became highly similar, suggesting the observed backward contrast was also comprised of a component that arose from multiple scattering of the initially forward generated signal. In the entire 500 μm thickness of the cellulose, the F/B ratio increased from unity to 6.2. It was explained that when the excitation focal point was moved deeper into the sample, the backward SHG became less coherent due to enhanced scattering, causing the backward signal to decrease. The forward generated SHG experienced less scattering because it was approaching the bottom surface of the tissue, causing the forward signal to increase. Although the trend of image composition variation along the depth is known through these investigations, there is no quantitative analysis about the variation of BS-SHG and BG-SHG among the B-SHG with depth variation.

As an attempt to quantify the contribution of BS-SHG to the B-SHG, Légaré et al. measured the proportion of BS-SHG to the forward generated SHG in the mouse Achilles tendon and fascia [50]. The B-SHG from thick samples was compared to the B-SHG from thin samples. This measurement, together with the F/B ratio obtained from thin samples, determined the proportion of BS-SHG to the forward SHG, which was 20% and 2% for 2 mm thick mouse Achilles tendon and fascia tissues, respectively. Among the total B-SHG, the BS-SHG accounted for 83% and 44%, respectively. According to Légaré's measurements, the BS-SHG dominated the B-SHG in a 2 mm thick mouse Achilles tendon while it contributed equally to the B-SHG

with the BG-SHG in fascia tissues of a few mm thick. A drawback of this work is that slicing of tissues is necessary for comparing the F/B ratio of thin and thick samples. Measuring the ratios at different locations may be affected by the microstructure of the collagen structure at that location because a small change of microstructure may also impact the results. Therefore, a non-invasive method quantify the scattering of backward scattering of SHG is desired.

Previously, Han et al. presented a similar method to measure the F/B ratio without using a forward detection channel in a confocal multiphoton microscopy [80]. The authors separated the BG-SHG and BS-SHG according to their distinct spatial distribution of signal intensity in the confocal pinhole plane. The BG-SHG was described as a Gaussian distribution with a narrow peak when the scattering after generation was neglected; while the BS-SHG was described as a uniform distribution over the radial distance from the optical axis due to its diffusive nature. Their summation constituted B-SHG in the pinhole plane. The relative amplitudes of the Gaussian and uniform distributions were obtained by collecting the B-SHG through a series of pinholes of different radii, and these relative amplitudes were converted to the proportion of BS-SHG to B-SHG. However, their method has only been applied to a focal depth near the surface. In here, we will extend the method to a more general condition where the focal depth is not limited to the surface and also consider scattering of the BG-SHG.

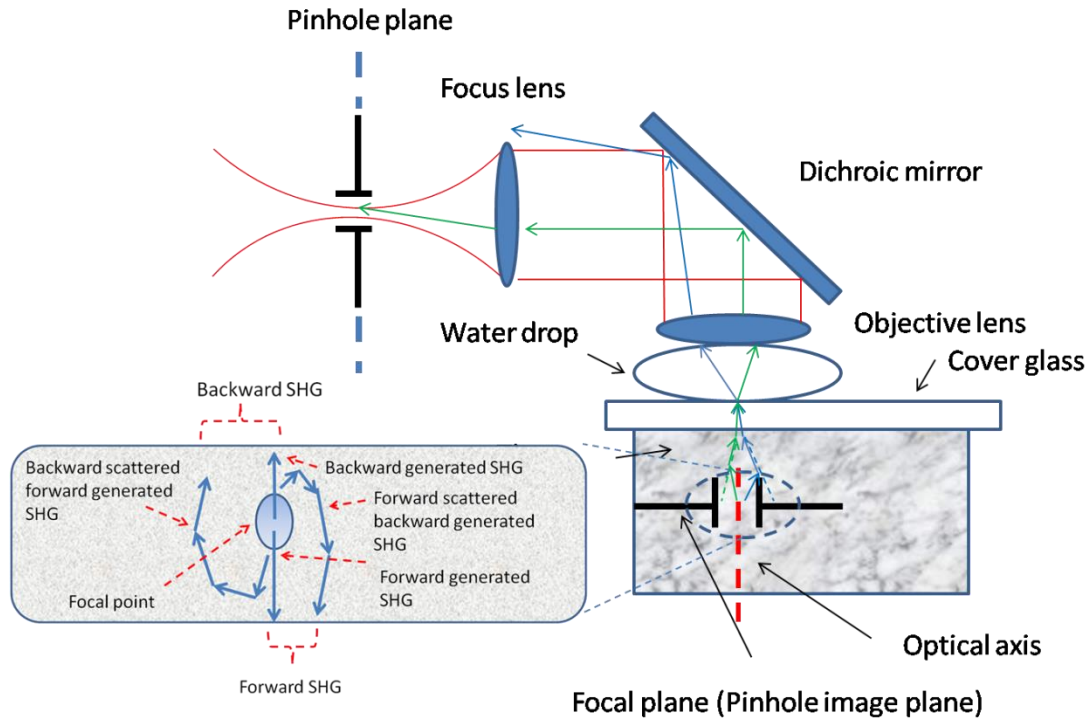


Figure 4.1 An illustration of photon generation and collection by pinholes in the Monte Carlo simulation with various SHG signal components in forward and backward directions.

In this work, we apply the model of SHG signal distribution described in [80] and extend the SHG pinhole measurement based on various core-diameter fibers in a confocal multiphoton microscopy to investigate the proportion of BS-SHG to the forward generated SHG and the B-SHG from different mouse collagen tissues. The distribution of BG-SHG and BS-SHG are different at the focal plane, which will be verified by Monte Carlo (MC) method. Utilizing this property, the contribution of BS-SHG to the B-SHG and the proportion of BS-SHG among the forward SHG can be measured. The pinhole method quantifies the contribution of BS-SHG and BG-SHG to the B-SHG. One advantage of this method is that the proportion of BG-SHG and BS-SHG among the B-SHG can be calculated without the need of forward detection, which can be useful for potential clinical applications.

4.2 Methods

4.2.1 Calculation methods

In this subsection, we describe the two methods used for quantifying the proportion of BS-SHG. Experimental results obtained by these two approaches are compared in the later sections.

The ratio of SHG power measured in the forward direction over the one measured in the backward direction is defined as F/B . The ratio detected from thin sample $(F/B)_{thin}$ is considered to reflect the ratio of the forward generated SHG over the BG-SHG from the focal volume because scattering is minimum in a thin sample. For thick samples, the corresponding ratio $(F/B)_{thick}$ is different from $(F/B)_{thin}$. Assuming that scattering of the BG-SHG is negligible when compared to the scattering of the forward generated SHG, the $(F/B)_{thick}$ can be expressed as,

$$\left(\frac{F}{B}\right)_{thick} = \frac{S_F(1-c)}{S_B + cS_F} \quad (4.1)$$

where S_F and S_B are the SHG power generated in the forward and backward directions from the focal volume, whose ratio S_F/S_B can be approximated by $(F/B)_{thin}$. The proportion of BS-SHG to the forward generated SHG, represented by c , is

$$c = \frac{(S_F/S_B) - (F/B)_{thick}}{[1 + (F/B)_{thick}](S_F/S_B)} = \frac{(F/B)_{thin} - (F/B)_{thick}}{[1 + (F/B)_{thick}](F/B)_{thin}} \quad (4.2)$$

Similar method was utilized in [50], in which $(F/B)_{thin}$ and $(F/B)_{thick}$ are both measured. Since the summation of BG-SHG and BS-SHG is the B-SHG, we can deduce the proportion of BS-SHG to B-SHG to be $\rho = cS_F/(S_B + cS_F) = 1/(S_B/cS_F + 1)$. However, it may not be applicable to the situation where the tissue is too thick to obtain the forward SHG or scattering of BG-SHG is

not negligible. Therefore, we follow [80] to take another approach that is purely based on the SHG signal collected in the backward direction.

Instead of measuring the SHG power in both the forward and backward directions, the B-SHG, which is the sum of BG-SHG and BS-SHG at the pinhole plane, is investigated in the second approach. The BG-SHG and BS-SHG are expressed as a Gaussian and a uniform function, respectively, of the radial distance r from the optical axis as shown in Eq. (4.3). The b is the peak intensity and ω is the $1/e^2$ half width of the BG-SHG. The ω here is not the width of the focal point but rather the width of the signal spot on the detection pinhole plane, which is broader than the width of the focal point due to scattering. Although the forward generated SHG also follows a sharp Gaussian function in the forward direction at the focal plane where it is generated, the BS-SHG has a diffusive nature because it experiences multiple scattering. BS-SHG can be considered as a Gaussian function with very large ω such that it is relatively independent of the radial distance. Therefore, it can be further simplified as a uniform distribution over the length scales considered here. Forasmuch, f is the peak intensity of the forward generated SHG and c is the proportion of BS-SHG to the forward generated SHG. Dividing b in both terms on the right hand side of Eq. (4.3) does not alter the relative magnitude of these terms but makes our subsequent analysis and discussion simpler. The signal collected by a pinhole is the integration of the intensity over the pinhole area as shown in Eq. (4.4), where R is the pinhole radius. The first term on the right hand side of Eq. (4.4) represents the BG-SHG power collected at the pinhole plane, which corresponds to S_B if neglecting the loss from the focal plane to the pinhole plane. The second term represents the BS-SHG power collected at the pinhole plane which corresponds to cS_F .

$$I_{SHG}(r) = b \exp[-2(\frac{r}{\omega})^2] + fc \propto \exp[-2(\frac{r}{\omega})^2] + \frac{fc}{b} \quad (4.3)$$

$$P_{r=R} = \int_0^{2\pi} d\theta \int_0^R I_{SHG}(r) r dr \propto 8\pi \left\{ 1 - \exp\left[-2\left(\frac{R}{\omega}\right)^2\right] \right\} / \omega^2 + \pi R^2 fc / b \quad (4.4)$$

In Eq. (4.4), there are two unknowns ω and fc/b , where fc/b is the ratio of BS-SHG over BG-SHG at $r = 0$. Therefore, at least two pinhole measurements are necessary for solving them. In both simulations and experiments, we first obtain the SHG power as a function of pinhole size. Afterwards, the data points are fitted by the model described in Eq. (4.4) in order to obtain ω and fc/b values. The relative magnitude of BG-SHG over BS-SHG is known after ω and fc/b are known. Since the ratio of the two terms stands for cS_F/S_B , aided with the measured S_F/S_B by $(F/B)_{thin}$, which reflects the generation ratio, we can obtain c .

4.2.2 Sample preparation

Three male C3H/HeN mice, four weeks of age were sacrificed. Tail samples were firstly removed and tendon samples were stripped off from the bone structures after the thin layers of outer skin were peeled off. The tendons were measured directly right after they were obtained. Achilles tendon was exposed in its full length after removal of the skin from the hind legs. A dissecting scope helped with determining the thickness of the tissue. The tissue blocks were embedded in paraffin and prepared for frozen sectioning. The embedded tissues were sectioned to 10 μ m thickness using a cryostat. The sections were then transferred to coverslips.

4.3 Monte Carlo simulation

In order to characterize the distribution of BG-SHG and BS-SHG in the pinhole plane and to validate the pinhole method, a MC simulation is conducted. The purpose is to examine the BG-SHG spatial distribution on the pinhole plane when the focal point is not on the surface but inside tissue. This is necessary because only if its distribution satisfies the Gaussian expression, can we apply multiple pinhole measurements and curve fitting with Eq. (4.4). When the scattering is too strong, the BG-SHG distribution may deviate from Gaussian expression, which may affect the accuracy of the pinhole method. In [80], the authors assumed that the focal point was close to the top surface, and the BG-SHG was Gaussian distributed. Therefore, their measurements were restricted to the surface only. Another requirement of applying Eq. (4.4) is the uniform distribution of BS-SHG intensity in the pinhole plane. For thin tissue samples with small scattering coefficients, the uniform distribution may not be satisfied. Besides examining the BS-SHG and BG-SHG distribution under various conditions, BS-SHG and BG-SHG photons can be differentiated by MC simulation so that the contribution of forward SHG and B-SHG can be obtained. Comparing these results with the ones obtained from simulating pinhole method, the principle of the pinhole method can be validated.

As a confocal setup, pinholes with various radii are used to collect the photons as shown in Fig. 4.1, where the pinhole plane is conjugate to the focal plane (pinhole image plane). The magnification from the objective and focus lens pair is set to be unity in our simulation for simplicity. Photons generated at the focal plane need to propagate through the tissue and pass through the pinhole prior to being collected. If the BG-SHG is generated at the tissue surface, then tissue scattering in the collection path can be neglected and the signal spot size at the pinhole plane should be the same as the signal spot size at the focal plane. However, if the BG-

SHG is originated from deeper inside the tissue, then the signal spot size at the pinhole plane should be much larger than the signal spot size at the focal plane due to scattering. Effect of scattering on the signal spot size at the pinhole plane can be simulated by MC.

Only the photons that fall within the pinhole and the collection angle of the detection system will be collected. Each photon exits the tissue surface at a specific position and angle which link a unique ray trace between the pinhole plane and the pinhole image plane. Therefore, when a SHG photon exits the tissue, it is geometrically back-projected to the pinhole image plane, where it can be analyzed to determine whether it falls within the image of the confocal aperture on that plane, and thus can be collected by the optical system or not [81]. For example, the photon following the blue path in Fig. 4.1 is not collected by the pinhole, but the photon following the green path is collected. Other than the position of the back projected photon, its exit angle with respect to the optical axis needs to be smaller than the NA of the objective lens in order to be collected. The interface between cover glass and collagen tissue does not alter SHG ray path because the refractive index of collagen at 400 nm is close to that of glass [49], while the interface between cover glass and immersion water is supposed to bend the SHG ray path slightly away from the optical axis due to their relative refractive index. However, it does not affect the conjugate nature between the pinhole plane and its image plane. Due to the conjugate relation between the pinhole image plane and the pinhole plane, the distribution of SHG signal on the pinhole plane can be plotted according to the distribution on the pinhole image plane determined by this back projection method.

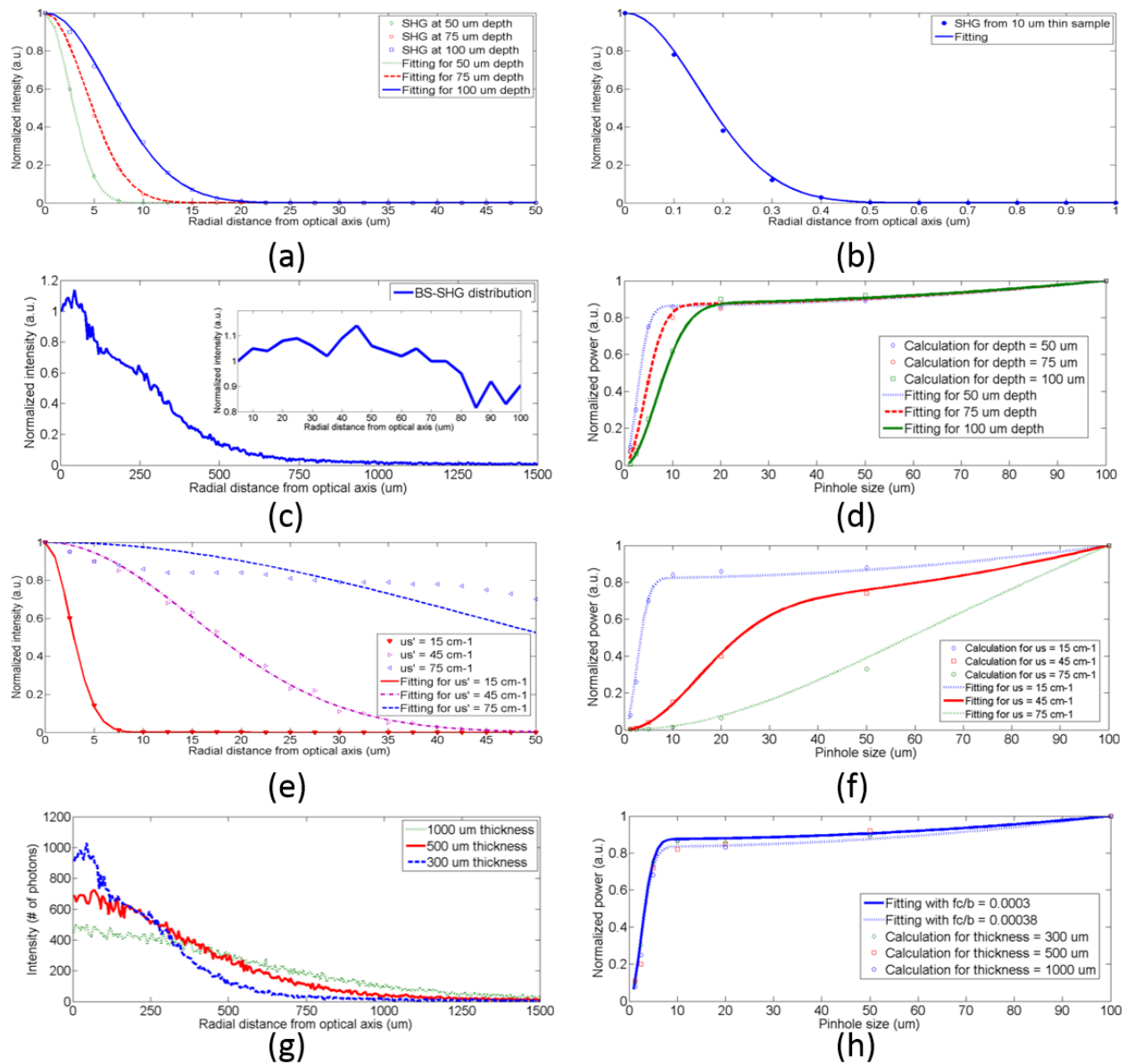


Figure 4.2 (a) The BG-SHG intensity only versus radial distance from optical axis in the pinhole image plane for SHG at 50, 75 and 100 μm depth; (b) BG-SHG intensity only distribution without scattering in the pinhole image plane; (c) BS-SHG intensity only versus radial distance from optical axis at 50 μm depth with 300 μm thicknesses; (inset) the zoomed in BS-SHG distribution over a shorter range; (d) dependence of relative B-SHG power on pinhole sizes for F/B ratio = 7.5 in the focal plane at the 50, 75 and 100 μm depths; (e) BG-SHG intensity versus radial distance from optical axis for reduced scattering coefficients 15, 45 and 75 cm^{-1} ; (f) dependence of relative B-SHG power on pinhole sizes for F/B ratio = 7.5 in the focal plane at

three reduced scattering coefficients; (g) BS-SHG intensity versus radial distance from optical axis for tissue thicknesses as 300, 500 and 1000 μm ; (h) dependence of relative B-SHG power on pinhole sizes for F/B ratio = 7.5 in the focal plane for the three thicknesses.

As the general formalism of the MC simulation will be presented in detail in Appendix A, we only report the modification to the basic approach required to simulate the propagation of the forward and backward generated SHG photons. In the simulation, 800 nm excitation wavelength and an objective lens with $\text{NA} = 0.8$ are used. The forward and backward generated SHG photons have a Gaussian distribution at the focal plane with $\omega_0 = 0.5 \mu\text{m}$, according to the lateral intensity squared profile in Ref. [31]. The angle distribution of the SHG photons cannot be simply determined by the NA of the objective lens because the phase matching condition refrain large angle emission from happening. Therefore, we use the experimentally measured parameters given in [80] as $\theta = \pm 15$ degree around the optical axis as the maximum emission angle from the optical axis. The refractive index of the tissue and the water surrounding the tissue are 1.5 and 1.3 respectively. The anisotropy, scattering and absorption coefficients are 0.9, 150 cm^{-1} and 1 cm^{-1} unless otherwise stated [82, 83]. The reduced scattering coefficient $\mu_s' = 15 \text{ cm}^{-1}$ is within the range of measured values in Ref. [84].

Fig. 4.2 (a) plots the intensity distributions of BG-SHG, which are generated at different depths, over the radial distance from the optical axis. The tissue is modeled as 300 μm thick. All the intensities are normalized to its maximum at optical axis. It is observed that BG-SHG generated at 50, 75 and 100 μm depths decays exponentially with the radial distance from the optical axis and the half widths at $1/e^2$ are 5.0, 8.2 and 13.0 μm respectively. The deeper the focal plane, the larger the spot size of the BG-SHG observed at the pinhole image plane due to

increased scattering. At these depths, the distributions of BG-SHG match with the Gaussian shape. As a comparison, the distribution of BG-SHG in a sample as thin as 10 μm from which the scattering effect can be neglected is plotted in Fig. 4.2 (b). Without scattering, the width of the SHG spot is not broadened in the pinhole image plane so that it keeps the same half width of the original focal spot as 0.25 μm .

Fig. 4.2 (c) shows the distribution of BS-SHG in the pinhole image plane. Due to multiple scattering, the BS-SHG has a very broad spot size. It is relatively uniform within 100 μm and then starts to decrease exponentially when the radial distance is larger than 100 μm as shown in the inset of Fig. 4.2 (c). The fluctuation is due to the limited number of photons simulated in the simulation.

We then draw the dependence of B-SHG power on the pinhole size assuming the ratio of forward and backward generated SHG is 7.5 in the focal volume at 50, 75 and 100 μm focal depths as shown in Fig. 4.2 (d). This particular ratio is from mouse tail tendon F/B intensity ratio experiment measurements which will be described in Section 4.5. Good model fittings are obtained when $\omega = 5 \mu\text{m}$ and $fc/b = 0.0003$ for the 50 μm focal depth, $\omega = 8.2 \mu\text{m}$ and $fc/b = 0.00075$ for the 75 μm focal depth, and $\omega = 13 \mu\text{m}$ and $fc/b = 0.0018$ for the 100 μm focal depth. From the ω and fc/b values, the ρ and c parameters are obtained as $\rho = 19.4\%$ and $c = 3.2\%$ for 50 μm depth, $\rho = 18.4\%$ and $c = 3.0\%$ for 75 μm depth, and $\rho = 17.4\%$ and $c = 2.8\%$ for 100 μm depth, respectively. It shows that the deeper the focal depth (with fixed tissue thickness), the less BS-SHG contributes to the backward SHG. Since the path length for the generated photons is shorter when the depth is deeper, the BS-SHG photons are less likely to be backscattered. The results obtained by this method are compared with MC simulation. In the simulation, we

differentiate the BS-SHG and BG-SHG photons collected within the 100 μm radius area in the pinhole image plane according to their original generation direction. The simulation gives $\rho = 19.9\%$ and $c = 3.2\%$ for 50 μm depth, $\rho = 16.8\%$ and $c = 2.7\%$ for 75 μm depth, and $\rho = 15.6\%$ and $c = 2.4\%$ for 100 μm depth. The good matching between simulation and our fitting method validates the principles of this pinhole measurement in the above conditions.

The scattering properties of tissues may vary over a large range among different tissue types and species. Therefore, we also simulate the intensity distribution of BG-SHG at 50 μm depth with reduced scattering coefficient μ_s' of 15, 45 and 75 cm^{-1} in a 300 μm thick tissue as shown in Fig. 4.2 (e). A reduced scattering coefficient of 45 cm^{-1} approximates that of Achilles tendon, which is a tissue type measured in our experiment and in Ref. [50]. The spot size increases from 5 to 30 μm and a Gaussian distribution is still observed with the scattering coefficient increased from 15 to 45 cm^{-1} . However, when the scattering coefficient increases to 75 cm^{-1} , the BG-SHG shows a $1/e^2$ half width as $\sim 88 \mu\text{m}$ but the shape deviates from a Gaussian distribution.

The dependence of B-SHG on pinhole size is simulated in Fig. 4.2 (f) with the above scattering coefficients. The F/B intensity ratio is still 7.5. Substituting the ω obtained in Fig. 4.2 (e) into Eq. (4.4), the optimum model fitting are obtained with $fc/b = 0.0003, 0.021, \text{ and } 0.45$ for the reduced scattering coefficients of 15, 45 and 75 cm^{-1} . The corresponding ρ and c are 21.2% and 3.5%, 34.2% and 10.5%, 59.0% and 20.5% for 15, 45, and 75 cm^{-1} . Direct MC simulation results are 19.9% and 3.2%, 32.1% and 10.2%, 53.0% and 17.1% respectively. The difference between pinhole method and simulation increases with μ_s' such as the $\mu_s' = 75 \text{ cm}^{-1}$ case. For large μ_s' since the ω deviates from Gaussian, the fc/b parameters have to be set higher for good

fitting, which results in an over estimation of the BS-SHG. It demonstrates that our pinhole measurement method has a limitation for tissues with large scattering coefficients.

We also investigate how tissue thickness affects the SHG scattering. In the MC simulation, the μ_s' is 15 cm^{-1} and the tissue thicknesses are 300, 500 and 1000 μm . The focal depth is at 50 μm and F/B intensity ratio is 7.5. It is known that the thickness of tissue affects the BS-SHG distribution significantly. Hence, the distributions of BS-SHG for the three thicknesses are illustrated in Fig. 4.2 (g). For 300 μm thickness, the intensity drops down quickly when the radial position is deviating from the optical axis. Intensities drop slower in the 500 and 1000 μm cases, but thicker tissues result in stronger BS-SHG. By normalizing the three distribution curves, it is confirmed that at least within 100 μm radial distance from the optical axis, their distributions are approximately uniform.

By repeating the previous pinhole method and simulation, it is found that the curves from Eq. (4.4) and discrete dots from MC simulation for different thicknesses are very close in Fig. 4.2 (h). All the data points seem to fit within a small range of fc/b . Thus we calculate that ρ may vary from 19.0% to 23.5% and c may vary from 3.0% to 4.1%. From MC simulation, the ρ and c are 19.9% and 3.2% for 300 μm , 21.8% and 3.8% for 500 μm , and 23.8% and 4.1% for 1000 μm . From these results, the backward scattering does not vary significantly with thickness because the backward scattered photons are collected by a finite pinhole size, which in our case is the maximum pinhole size 100 μm . Although the BS-SHG is stronger for thicker tissues, the proportion of collected BS-SHG among the total BS-SHG is small because the BS-SHG is distributed over a wider range. On the contrary, the total BS-SHG intensity is weaker from thinner tissues but the proportion of BS-SHG collected is greater because the BS-SHG intensity

drops down quickly when its radial distance deviates from the optical axis. These trends can be clearly seen in Fig. 4.2 (g). If we extend the pinhole size to 1500 μm which almost covers the whole range of BS-SHG, the ρ and c from the above three thicknesses become 37.5% and 12.0%, 47.3% and 18.0%, 56.6% and 26.0%. The ρ and c values not only depend on the tissue scattering properties, but also depend on the size of the collection area. The differences between various thicknesses are greater when we consider all the BS-SHG. These simulation results indicate that larger pinhole sizes can collect more BS-SHG photons such that the scattering performance differences among different μ_s' or thicknesses are greater. Nevertheless, in order to obtain an accurate prediction for ρ and c by the pinhole method, the largest pinhole size is limited. It is because that uniform distributed BS-SHG is necessary in order to apply Eq. (4.4). As we can see in Fig. 4.2 (c) and (g), the BS-SHG distribution is no longer uniform with respect to the radial distance when the radial distance is far from the optical axis. In a 300 μm thick tissue, according to our simulation, the uniform distribution can only be maintained within 100 μm from the optical axis. Therefore, this pinhole method can only be applied to predict the BS-SHG photon's scattering performance collected by a pinhole area smaller than it. In addition to this limitation, from Fig. 4.2 (e) and (f), when the scattering coefficient is too large, the BG-SHG deviate from Gaussian distribution. It may causes overestimation of ρ and c .

4.4 Experiment setup and calibration

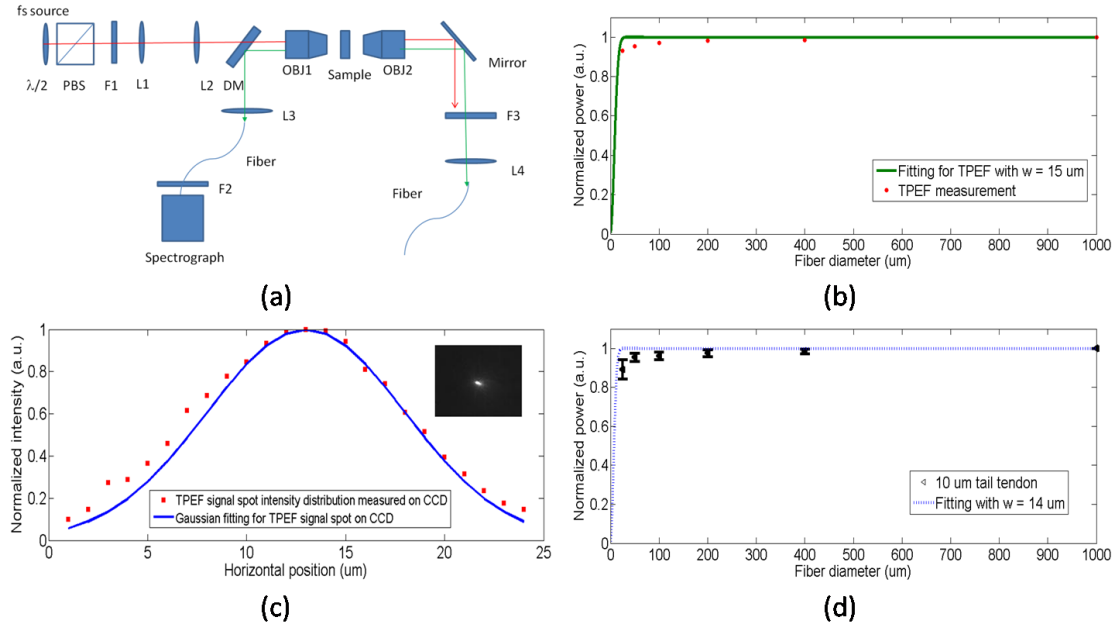


Figure 4.3 (a) Experiment setup for measuring the scattering property of tissues based on a confocal multiphoton microscopy; $\lambda/2$, half wave plate; PBS, polarization beam splitter; F1, F2, and F3, filter sets; L1, L2, L3, and L4, lens sets; OBJ1, and OBJ2, objective lens; DM, dichroic mirror; (b) experiment measurement for the dependence of relative backward TPEF power on fiber diameter for TPEF solution and the fitting curve with $w = 15 \mu\text{m}$; (c) TPEF intensity distribution along the horizontal direction on CCD image plane and its fitting with Gaussian shape; (inset) CCD captured image for TPEF signal; (d) experiment measurement for the dependence of relative B-SHG power on fiber diameter for of 10 μm mouse tail tendon tissues and the fitting curve with $w = 14 \mu\text{m}$.

Fig. 4.3 (a) shows the schematics of the experimental setup for single point detection. Its advantage is that it is easier to implement the pinhole measurement than a typical imaging setup which requires a de-scanned detection. The light source is a mode-locked titanium-sapphire laser (Chameleon, Coherent, USA) providing wavelength tunable femto-second laser pulses from 720 to 960 nm. A half wave plate ($\lambda/2$, 10RP52-2, Newport, USA) and a polarization beam splitter

(PBS, PBS052 AR600-1000 nm, Thorlabs, USA) are used to control the excitation laser power. The laser spectrum is cleaned by a long pass filter (F1, FGL715, Thorlabs, USA). The laser beam is expanded by a pair of lenses (L1, L2) with focal lengths of 35 and 300 mm respectively to fill the back aperture of the water-immersion 40X objective (OBJ1, NA = 0.8, LUMPLFLN, Olympus, USA). The backward SHG is collected by the same objective and is directed to the spectrograph through a 660 nm long pass dichroic beam splitter (DM, FF660-Di02, Semrock, USA). The SHG signal is coupled into a multimode fiber by a 35 mm focal length focusing lens (L3). A number of multimode fibers with various core diameters from 25, 50, 100, 200, 400 to 1000 μm are used as pinholes in the experiment. In the Achilles tendon measurements, an additional 600 μm fiber is used for more accurate measurements. Measurements of SHG power are obtained with a spectrograph (SpectraPro-150, Roper Scientific, USA), which is directly connected with the multimode fibers. The residual excitation laser beam is further attenuated by a band-pass filter (F2, FF01-750, Semrock, USA) attached to the spectrograph. The forward SHG is collected by a water-immersion 60X objective (OBJ2, NA = 1.0, LUMPLFLN, Olympus, USA) and is then reflected by a mirror and further focused into a 600 μm multimode fiber by a 25 mm focal length lens (L4). Another low-pass filter (F3, FF01-680, Semrock, USA) blocks the excitation laser beam.

For the purpose of verifying our pinhole measurements by different core-diameter fibers, we measure the dependence of two photon excitation fluorescence (TPEF) signal on the pinhole size from a homogeneous fluorescence solution in the backward direction as shown in Fig. 4.3 (b). Since there is negligible scattering in the homogeneous solution, only the backward generated TPEF is collected. The value of fc/b equals to zero in our curve fitting because there is no scattered forward TPEF in the backward direction. It is found that $\omega = 15 \mu\text{m}$ provides a good

fitting in Fig. 4.3 (b). The fitting criteria follow the least square fitting such that the parameter ω and fc/b minimize summation of the squares of offsets of the experimental data points from the fitting curve. The sensitivity and accuracy issue of the fitting will be discussed in the next section. The deviation from the fitting curve for relatively small fiber diameter may be caused by the low NA's of these fibers which are 0.1 while the NA's of the rest fibers are 0.22. A 0.1 NA is already very close to the NA of the focusing lens L3 which is 0.11 calculated according to the focal length of L3 and the beam width of TPEF signal. In this way, the signal collection is affected slightly. Furthermore, the fiber core diameters are all large compared to the spot size under the condition of no scattering. Therefore, most of the signal is collected by the smallest fiber and the intensity change cannot be measured well by experiment. For comparison, the spot size of the TPEF signal at the focal spot of L3 is directly measured by a CCD camera (MLC 205, Matrix vision, Germany) as shown in the inset of Fig. 4.3 (c). The $1/e^2$ spot size for the TPEF signal is $\sim 23 \mu\text{m}$ and $16 \mu\text{m}$ along the horizontal and vertical directions in the CCD image plane respectively. Fig. 4.3 (c) plots the intensity distribution along the horizontal direction on the CCD and the fitting with a Gaussian curve. Please be aware that the ω we obtained from pinhole measurement is half of the width of the signal spot size at $1/e^2$ and the full width should be $30 \mu\text{m}$, which matches with the CCD measurement.

Similarly, we also obtain the SHG power versus fiber diameter for the $10 \mu\text{m}$ thick mouse tail tendon in Fig. 4.3 (d). Measurements of SHG signal intensity with each fiber are repeated five times. In order to avoid significant back reflection of the forward generated SHG from the tissue/glass interface, the thin tissue samples are laid beneath a coverslip rather than being sandwiched between a coverslip and a glass slide. There is no glass slide below the sample,

which is immersed in water. In 10 μm thick tissue samples, we assumed a negligible BS-SHG. Hence, the size of the focusing spot, ω can be fitted by Eq. (4.4) with $fc/b = 0$, which is found to be 14 μm . Considering that the theoretical $1/e^2$ width of the focal spot is 0.5 μm and the theoretical magnification of the objective lens (OBJ1 \sim 4.5 mm) and focusing lens (L3 \sim 35 mm) is 7.8 times, the theoretical spot size on the CCD is estimated to be around 4 μm . The broadening of the focusing spot in experiment is likely due to the spherical aberration and other aberrations of lens L3 which is a spherical singlet lens.

4.5 Experimental results and discussions

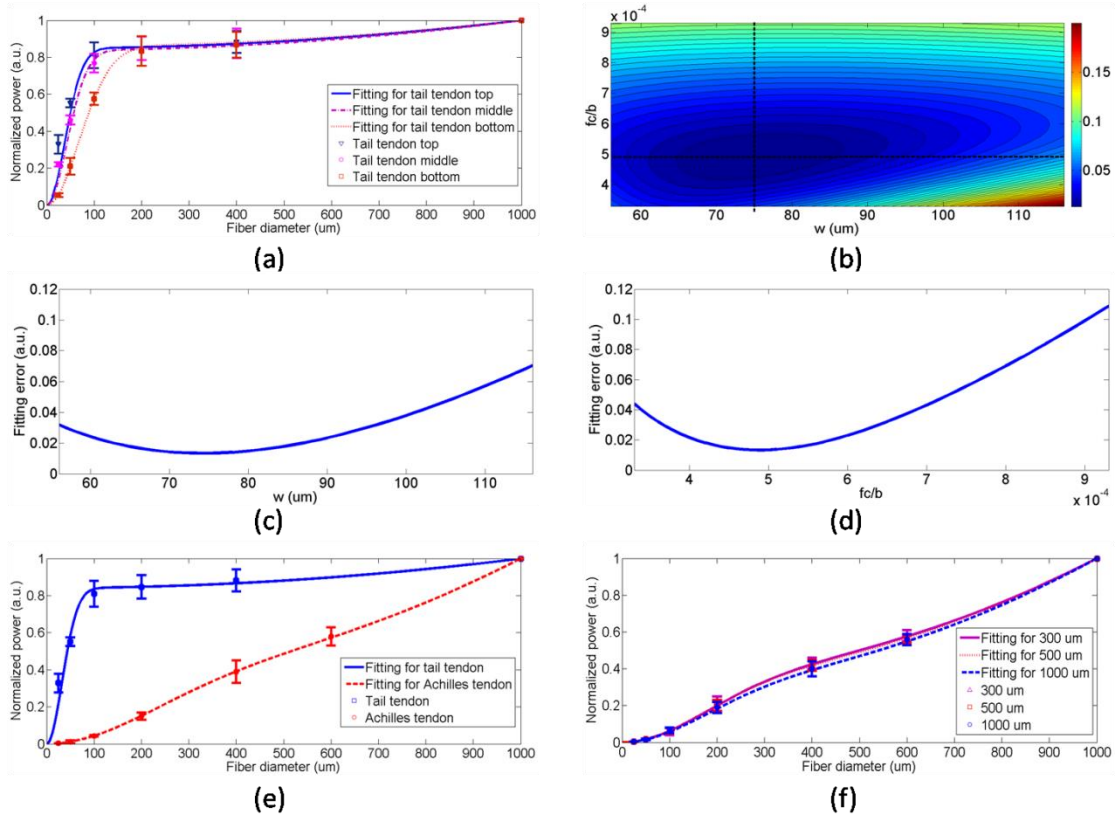


Figure 4.4 (a) Experiment measurement for the dependence of relative B-SHG power on fiber diameter for mouse tail tendon at different depths and the related fitting curves; (b) contour map plotting the isolines of fitting error with various w and fc/b ; the sensitivities are plotted along the two dash lines crossing at the best fitting pair ($w = 75$ and $fc/b = 0.0005$) as a function of w (c) and fc/b (d); (e) the dependence of relative B-SHG power on fiber diameter for tail tendon and Achilles tendon with similar tissue thicknesses and focal point depth; (f) the dependence of relative B-SHG power on fiber diameter for Achilles tendon with different thicknesses but at the same focal point depth 50 μm .

The normalized SHG signals of the mouse tail tendon tissue at three focal depths (50, 80 and 110 μm) beneath tissue surface are shown in Fig. 4.4 (a). The sample thickness is 250 μm . Each data point represents an average of five measurements of different lateral locations at the

specific focal depth. The fitted results are summarized in Table 4.1. Notice that when the focal depth gets deeper, the $1/e^2$ width (ω in second column) increases from 75 to 135 μm mainly due to stronger scattering of the BG-SHG. The fc/b parameter (in third column) also increases with depth, consistent with MC simulations in Fig. 4.2 (a). The ratio of BG-SHG to BS-SHG (S_B/cS_F in fourth column) increases from 5.62 to 6.07. The ratio of BS-SHG to B-SHG (ρ value in column five) decreases from 15.14% to 14.23%, because for fixed tissue thickness, the distance between focal point and rear surface of the tissue becomes smaller, which leads to less backscattering of the forward generated SHG.

The accuracy and sensitivity of this curve fitting method are discussed in Fig. 4.4 (b). As we mentioned, the curve fitting is based on least square such that the parameter ω and fc/b minimize summation of the square of the offsets at 25, 50, 100, 200 and 400 μm between experimental data and the fitting curve. Taking the measurements at tail tendon top as an example, summation of the offset square between experimental data and fitting curve with various ω and fc/b are plotted as isolines in the contour map. The minimum sum offsets square is 0.013 (a.u.), which is from the fitting curve with $\omega = 75 \mu\text{m}$ and $fc/b = 0.0005$. To quantify the quality of fitting, a fitting error is defined as summed square of the fitting offset divided by the summed square of the intensity values measured by different fibers. For this case, the fitting error is calculated to be 5%. We neglect the data for 1000 μm fiber because both experimental data and fitting curves are normalized to one at the largest fiber. Extending from the best fitting pair along the ω and fc/b direction, as the two dash line in the contour map, the fitting errors are relatively symmetry around the best fitting parameters in Fig. 4.4 (c) and (d) with similar slopes.

For the red fitting curve in Fig. 4.2 (d) and green fitting curve in Fig. 4. 3 (b) the fitting errors are 1.1‰ and 1.9‰, respectively.

Assuming that the F/B ratio measured for 10 μm thin samples can be approximated as the generation ratio for forward and backward SHG, i.e. $S_F/S_B = (F/B)_{thin}$, the percentage of the forward SHG that is backscattered can be calculated from the ratio of S_B/cS_F . The measured F/B ratio for 10 μm thin tendon is represented in the form of average (standard deviation) as 7.62 (0.81). The intensities are measured and averaged over five different positions on the tissues. Calibration of the forward and backward detection is based on the auto-fluorescence peak at 550 nm from the 10 μm skin tissue. The F/B absolute intensity ratio is found to be 0.5 for the fluorescence signal. All of our F/B measurements are then calibrated with this value. Some of the previous published results reveal that the F/B ratios measured for tendon are close to unity [52, 57]. With the corresponding F/B ratio from thin samples, we find the proportion of BS-SHG to the forward generated SHG, which is in Table 4.1 column six as

$$c = \frac{(S_B / cS_F)^{-1}}{S_F / S_B} = \frac{(S_B / cS_F)^{-1}}{(F / B)_{thin}} \quad (4.5)$$

From top surface to deeper depth, c (1) value varies from 2.3% (0.2%) to 2.1% (0.2%). As we have described in Fig. 4.2 (a) to (c), the reduced scattering coefficient, F/B intensity ratio and other parameters such as depth and thicknesses used in simulation are approximately the real values in experiments. Therefore, comparing the simulation with the experiment results (2.8 ~ 3.2% in simulation versus 2.1 ~ 2.3% in experiment), it is found that the simulation results are slightly greater than experimental results. This might be caused by the difference in the spot size between simulation and experiment.

The calculated fitting error for the simulation data (1.1‰) is smaller than that for the experiment data (5‰). It is because that, in the simulation, the BG-SHG and BS-SHG closely match with the Gaussian and constant profile described in Eq. (4.4). The actual distribution in experiment is not as perfect as in simulation, resulting in increased fitting error. In this study, the fitting error is relatively small compared to measurement error. In Fig. 4.4 (a), it is shown that the SHG intensity measurement shows a relatively large standard deviation. This fluctuation originates from the difference of the fiber position and possible sample movement over multiple measurements. Furthermore, the measurement of the $(F/B)_{\text{thin}}$ intensity ratio also shows a variation of $\sim 10\%$ over multiple locations. Thus, the accuracy of the ρ and $c(1)$ values are limited by the accuracy of the measurements instead of the fitting error. For single tissue type measured at the different depths, the variation in the ρ and $c(1)$ values are not significant. Nevertheless, a consistent trend in the change of ρ and $c(1)$ can still be obtained. A more significant depth difference may enlarge the difference between the ρ and $c(1)$ values. When comparing Achilles tendon with tail tendon, significant difference in ρ and $c(1)$ are obtained.

Table 4.1 A summary of the curve fitting parameters for pinhole experiment results and the derived values describing the scattering property of the tail tendon tissue at different depths.

Depth (μm)	ω (μm)	fc/b	S_B/cS_F	ρ (%)	c (1) (%)	F/B	c (2)(%)
50	75	0.0005	5.62	15.14	2.3(0.2)	6.23(0.09)	2.4(1.1)
80	85	0.0007	5.83	15.00	2.3(0.2)	6.45(0.11)	1.9(1.1)
110	135	0.0015	6.07	14.23	2.1(0.2)	6.63(0.15)	1.6(1.4)

Note: ω : the half $1/e^2$ width of the SHG spot in the pinhole plane; fc/b : the ratio of BS-SHG over BG-SHG at optical axis; S_B/cS_F : the BG-SHG over BS-SHG intensity ratio; ρ : the BS-SHG over B-SHG intensity ratio; c (1): the BS-SHG over forward SHG intensity ratio obtained from pinhole method; F/B : the forward over backward SHG intensity ratio; c (2): the BS-SHG over forward SHG intensity ratio obtained from measuring thin and thick sample. The number in the parenthesis is the standard deviation of the corresponding parameters.

We can also take the approach described in Eq. (4.2) to directly calculate c . The F/B ratio is measured at the three depths in the thick tissues directly in the column seven of Table 4.1. At each depth, five measurements are conducted at different lateral positions. The increase of the F/B ratio is also observed and discussed in Ref. [6] from fibrillar cellulose matrices. According to the spot size determined, the spot size in forward and backward direction should be no larger than the collection fiber core diameter of 600 μm and 1000 μm respectively. Therefore, it is reasonable to assume that most of the forward and backward generated SHG are collected by our fiber collection system in their respective channels. Using the $(F/B)_{thin}$ from 10 μm samples and $(F/B)_{thick}$ at different depths, we obtain the parameters c at different depths by applying Eq. (4.2), which are listed in the eighth column of Table 4.1 indicated by c (2). From top depth to deeper depth c varies from 2.4% (1.1%) to 1.6% (1.4%). These values match with the values obtained

by pinhole measurements. The standard deviation of $c(2)$ is greater than that of $c(1)$ because the standard deviations of F/B ratio measurements from thin and thick tissues are transferred to the calculation of $c(2)$.

The experiment is repeated three times to calculate ρ and $c(1)$ in tail tendon from three animals at different depths. The results are listed in Table 4.2. Note that ρ and $c(1)$ are similar for the three animals. In addition, the trend such as less scattering of forward SHG with increasing depth inside the tissue is also observed among all the data sets.

Table 4.2 The ρ and $c(1)$ values at different depths for mouse tail tendon tissues from three animals.

Animal I			Animal II			Animal III		
Depth (μm)	ρ (%)	$c(1)$ (%)	Depth (μm)	ρ (%)	$c(1)$ (%)	Depth (μm)	ρ (%)	$c(1)$ (%)
50	15.14	2.3(0.2)	40	14.40	2.5(0.4)	40	14.78	3.0(0.4)
80	15.00	2.3(0.2)	75	14.68	2.3(0.2)	80	14.36	2.5(0.3)
110	14.23	2.1(0.2)	120	14.15	2.0(0.3)	130	13.84	2.1(0.3)

In addition to comparing scattering in mouse tail tendon at different depths, we also compare the scattering in tail tendon with Achilles tendon from hind legs as shown in Fig. 4.4 (e). The tissue thickness is 270 μm and the depth of focal point is 50 μm . The curve fitting parameters ω and fc/b are obtained as 320 μm and 0.08, which provides ρ as 60.9%. The F/B ratio is measured as 23 (2.5), which is close to the values measured in Ref. [50]. The c is obtained as 6.8% (1.3%) accordingly. Compared with the results from tail tendon, at the same

depth, the ρ and c are 15.14% and 2.3% (0.2%). The c value difference between tail tendon and Achilles tendon is largely due to their respective scattering coefficient difference. According to previous literature, the scattering coefficient of Achilles tendon is around 45 cm^{-1} while that of tail tendon is from 8 to 30 cm^{-1} [50, 84]. Their F/B intensity ratios are measured to be 23 (2.5) and 7.6 (0.8). The combined effects of F/B intensity ratio and scattering coefficient determine that the BS-SHG contributes to the total backward SHG more in the Achilles tendon than in the tail tendon. In $200 \sim 300 \text{ }\mu\text{m}$ thick tail tendon, at different depth, the BS-SHG constitutes 15% of the total backward SHG while it constitutes more than 60% in the Achilles tendon. The proportion of forward SHG that backscatters is two times greater for the Achilles tendon tissue than the tail tendon tissue.

As we discussed in Fig. 4.2 (g) and (h), the scattering differences are not significant when different thicknesses of tissues are compared by a relative small pinhole size. In order to demonstrate a stronger thickness dependent BS-SHG, we replace the 35 mm focal length focusing lens L3 with another 25 mm focal length lens to reduce the beam size at the pinhole plane. Therefore, the relative collection area can be increased. The cost is that the NA of the signal can be greater than that of the collection fiber especially for small NA fibers, which may affect the signal collection for small diameter fibers.

In Fig. 4.4 (f), ρ and c are calculated from pinhole measurements with improved collection area for Achilles tendon tissues of different thicknesses: 270, 520 and 1000 μm . The focus is fixed at 50 μm . The fitting parameters are summarized in Table 4.3. It is noted that the ρ and c increase with thickness. For a 1000 μm tissue, 10.1% (1.4%) of the forward SHG are

backscattered and 70.5% of the backward SHG originate from BS-SHG. This result is close to the result reported in Ref. [50].

Table 4.3 The curve fitting parameters and the derived ρ and c (1) values of Achilles tendon with different thicknesses at 50 μm depth.

Thickness (μm)	ω (μm)	fc/b	S_B/cS_F	ρ (%)	c (1) (%)
270	325	0.10	0.54	65.02	8.5(1.6)
520	320	0.11	0.48	67.50	9.0(1.3)
1000	325	0.13	0.42	70.50	10.1(1.4)

In this study, we quantify the contribution of BS-SHG to B-SHG in two types of collagen tendon tissues with different scattering coefficients. For strong scattering tissues such as Achilles tendon, the BS-SHG dominates B-SHG. For moderate scattering tissues such as tail tendon, however, the scattering of the forward SHG is not the major source of the backward SHG.

Tissue scattering is characterized by transportation mean free path. When the photon propagation length in the tissue approaches transportation mean free path, the probability of completely randomizing its direction approaches 100%. Therefore, tissue with a large reduced scattering coefficient μ_s' such as Achilles tendon is likely to give significant number of forward generated backward scattered photon. When the focal point approaches the bottom surface of the tissue, the shortened propagation length reduces the backward scattering.

A strong original backward generation increases the proportion of BG-SHG among the total backward SHG. The original backward generation strength is another important difference between tail tendon and Achilles tendon. Although BG-SHG is another source of backward SHG,

the mechanism for BG-SHG is still not fully understood. This topic will be studied in the next chapter.

4.6 Conclusions

In summary, we propose a pinhole method to investigate the scattering properties of SHG in the mouse tail tendon and Achilles tendon based on confocal multiphoton microscopy. Monte Carlo simulation proves that the BG-SHG and BS-SHG can be modeled as Gaussian distribution and uniform distribution respectively in the pinhole detection plane. Based on the knowledge of the SHG distribution, we also obtain the spot width of the BG-SHG and the relative intensity of the BG-SHG and BS-SHG. The advantage of the pinhole method, compared with previous back scattering quantification methods, is that it is non-invasive and requires little sample preparation. Through pinhole measurements, the dependence of BS-SHG on focal depth is quantified in experiment. It is found that BS-SHG does not dominate the total backward SHG in tail tendon tissues with thicknesses of around three hundred micrometers. For Achilles tendon with similar thickness and focal depth, the contribution of BS-SHG to B-SHG is much higher due to its higher scattering coefficient, and the F/B intensity ratio. When the thickness of the Achilles tendon increases to a thousand micrometers while maintaining the same focal depth, as high as ~ 10% of the total forward SHG is backscattered and collected in the pinhole. These investigations can help understand and interpret SHG measurement in microscopy and spectroscopy.

Chapter 5: Phase matching of backward second harmonic generation assisted by lattice structure

In this chapter, we study the phase matching mechanism of backward SHG in collagen. It provides explanation to the wavelength dependence spectrum and scattering measurement of backward SHG results in the previous chapters.

5.1 Introduction

In the last chapter, as we have discussed, backward scattered SHG does not dominate the total backward SHG in tail tendon tissues with thicknesses of around three hundred micrometers. It implies that backward generated SHG still contributes significantly to the total backward-collected SHG. A clear understanding about the mechanism of backward SHG in collagen tissues is thus needed. As we have reviewed in Chapter 1, the current available models have limitations in both theoretical modeling method and experiment validation. Therefore, it raises the necessity of investigating the mechanism of backward phase matching in collagen tissues in a more systematic theoretical framework and experiment approach.

Several models have been proposed in order to explain the significant backward generated SHG. Williams et al. attributed the SHG from a thin surface layer with tens of nanometers thickness, which reduced the interaction length in the collagen so that it was comparable with the coherence length for backward SHG [52]. Type I collagen fibrils usually form highly organized quasi-crystalline structures, which have been proposed as a quasi-phase matching (QPM) structure to study the interaction between neighboring fibrils [60, 61]. QPM is a

technique for phase matching nonlinear optical interactions in which the relative phase is corrected at regular intervals using a periodic structure built into the nonlinear medium [62]. In Ref. [60], LaComb et al. assigned different values for the phase mismatch Δk for the forward and backward directions to explain the relative intensity in both directions, but how the Δk was related with the structure was not explained. Later on, Tian et al. theoretically discussed the effect of additional wave vector by lattice structure on optimum backward SHG under a dipole model framework [61]. From the perspective of electrical field calculation, the difficulty of the dipole method lies in the selection of the unit dipole which generates the SHG. The dipole size selection is a tradeoff between accuracy and calculation volume. Identifying the physical meaning of an appropriate dipole size is not easy. Therefore, although intuitive, the dipole method lacks a physical insight into the problem and has some unsolved issues. In addition, the underlying assumption behind the dipole model is that the generated SHG photon does not interact with the surrounding fibrils, which is not strict.

The periodic collagen microstructure is similar as a 2D photonics crystal with a 2D periodic second order nonlinear coefficient. It has been reported that new phase matching processes can appear in a photonics crystal with 2D periodic nonlinear susceptibility mainly because the 2D structure of lattice could provide additional virtual momentum to the total phase mismatch [85-88]. Berger et al. first investigated different orders of QPM process which satisfies certain phase matching directions. The efficiency of the nonlinear process is proportional to the corresponding Fourier series coefficient [86]. The conversion efficiencies for different types of periodic structure such as hexagonal, square, rectangular, were compared in Ref. [85] in order to find the optimal one. Besides phase matching assistance, the conversion efficiency can also be enhanced via the strong localized fields and reduced group velocity at the edge of the band edge,

which usually requires a strong dielectric contrast between nonlinear material and medium in the structure [87, 88]. In collagen tissues, the dielectric coefficient contrast between fibrils and background is usually not very high. Therefore, the field localization effect and group velocity effect are not as important as the phase matching effect. Regarding the theoretical method applied, fundamental and SHG waves are assumed to be plane wave and nonlinear susceptibility is expanded by reciprocal vector in Ref. [85, 86] while all the major physical terms including wave functions are expanded by reciprocal vector in Ref. [87, 88]. The latter method is also called plane wave expansion, which is studied in detail in Ref. [89].

In this chapter, we study the backward SHG in biological tissues, specifically collagen. We apply a new approach that treats the collagen microstructure as a 2D photonics crystal and study its backward SHG. The method used in 2D photonics crystals will be applied on collagen microstructures. The hypothesis is that the backward generated SHG achieves phase matching by the assistance of periodic structure. It is validated by investigating the relation between excitation/emission angles and optimized excitation wavelength in both theory and experiment. The chapter is structured as follows: In the theory section, the principle of backward phase matching in a periodic lattice structure is revealed, and an SHG intensity expression is obtained by the plane wave expansion method; In the simulation section, effects of angle tilting, beam focusing, and single fibril diameter are simulated via the theoretical solutions; In the experiment section, the effect of different excitation and emission angles on the excitation spectrum of collagen tissues are experimentally investigated and compared with simulation.

5.2 Theory

5.2.1 Lattice assisted phase matching and angle tilting for backward SHG

Collagen tissue is composed of regularly aligned fibrils, which can be considered as a 2D lattice. From the TEM images in Fig. 1.1, collagen fibrils show a relatively regular packing structure which is similar to a 2D crystal. Collagen has been modeled as 2D periodic structure before in Ref. 61. Fig. 5.1 (a) shows the 2D lattice in the spatial space, where each dot represents a fibril cylinder. The elementary lattice vectors are $\mathbf{c}_1 = (0, a)$ and $\mathbf{c}_2 = (a, 0)$, where the parameter “ a ” represents the distance between the centers of two adjacent collagen cylinders. Fig. 5.1 (b) shows the corresponding elementary reciprocal lattice vectors in the k space, which are $\mathbf{d}_1 = (0, 2\pi/a)$ and $\mathbf{d}_2 = (2\pi/a, 0)$ given by $\mathbf{c} \cdot \mathbf{d}_j = 2\pi\delta_{ij}$ ($i, j = 1, 2$). Each dot in the k space represents a virtual momentum $(m2\pi/a, n2\pi/a)$, provided by the lattice structure, in which m and n are integers.

In this study, we only consider the case where the wave vectors are in the XY plane. For backward SHG, the wave vector of the SHG beam \mathbf{k}_{SHG} is at opposite direction as that of the fundamental beam $\mathbf{k}_{\text{fundamental}}$. The phase mismatch can be written as $\Delta\mathbf{k} = 2\mathbf{k}_{\text{fundamental}} - \mathbf{k}_{\text{SHG}} = 2\mathbf{k}_1 + \mathbf{k}_2$, where $\mathbf{k}_1 = \mathbf{k}_{\text{fundamental}}$ and $\mathbf{k}_2 = -\mathbf{k}_{\text{SHG}}$. Since the lattice structure introduces virtual momentum $\mathbf{K}_{mn} = m\mathbf{d}_1 + n\mathbf{d}_2$, the phase mismatch expression can be modified as $\Delta\mathbf{k}' = 2\mathbf{k}_1 + \mathbf{k}_2 - \mathbf{K}_{mn}$ in a periodic structure.

Taking $m = 1$ and $n = 0$, the virtual momentum becomes $\mathbf{K}_{mn} = \mathbf{d}_1 = (0, 2\pi/a)$ in the y direction, which is defined as the depth direction in our study. The projections of the phase mismatch in the x (lateral direction) and y directions are expressed as

$$\begin{aligned}\Delta k'_y &= 2 \times \frac{2\pi n_\omega \cos \alpha}{\lambda_{ext}} + \frac{4\pi n_{2\omega} \cos \theta}{\lambda_{ext}} - \frac{2\pi}{a} \\ \Delta k'_x &= 2 \times \frac{2\pi n_\omega \sin \alpha}{\lambda_{ext}} + \frac{4\pi n_{2\omega} \sin \theta}{\lambda_{ext}}\end{aligned}\tag{5.1}$$

The α and θ are the angles between the fundamental wave or SHG wave and y axis, with positive angles defined as tilting counter-clockwise. Here λ_{ext} is the fundamental excitation wavelength. The n_ω and $n_{2\omega}$ are the refractive index at the fundamental and SHG wavelengths, respectively. For simplicity, we will assume $n_\omega = n_{2\omega}$ in the rest of the chapter. In Eq. (5.1), the parameters λ_{ext} , α , and θ all affect the phase mismatch for a given spacing a .

From Eq. (5.1), phase matching in the x direction, where $\Delta k'_x = 0$, can be achieved when $\alpha = -\theta$. Phase matching in the y direction, meaning $\Delta k'_y = 0$, is only achieved at an optimum excitation wavelength that can be found as

$$\lambda_{opt} = 2n_\omega a (\cos \theta + \cos \alpha)\tag{5.2}$$

A simple illustration is shown as the vectors between point A and B in Fig. 5.1 (b). When $\alpha = -\theta = 0$, phase matching can be achieved at

$$\lambda_{opt} = 4n_\omega a\tag{5.3}$$

For excitation wavelengths shorter than λ_{opt} , phase matching can still be achieved by increasing θ and α according to Eq. (5.2). However, for excitation wavelengths longer than λ_{opt} , there is no solution to θ and α in Eq. (5.2), which means there is no perfect phase matching for those longer wavelengths.

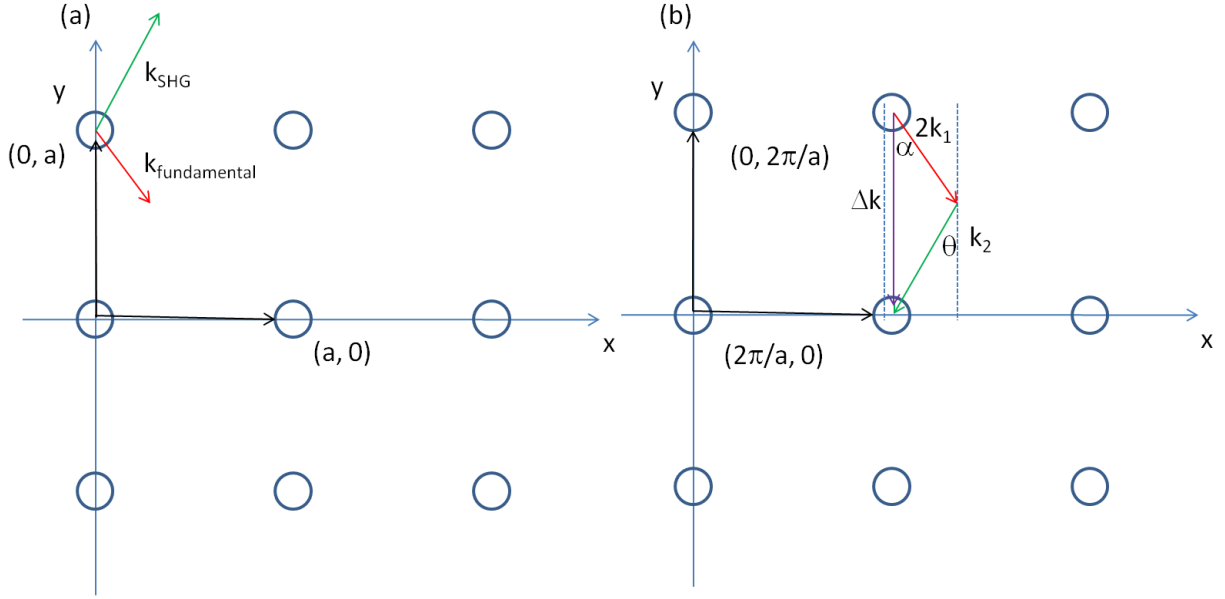


Figure 5.1 (a) Illustration of the periodic structure with elementary lattice vectors $(a,0)$ and $(0,a)$; The red and green arrows represent the wave vector of fundamental and SHG $k_{\text{fundamental}}$, k_{SHG} ; (b) the corresponding k space diagram with elementary reciprocal vector $(0,2\pi/a)$ and $(2\pi/a, 0)$; The red, green and purple arrows between A, B dots illustrate fundamental, SHG wave vector k_1 , k_2 and the backward phase mismatch Δk .

5.2.2 Theoretical background of the SHG in collagen simulation

In order to describe the dependence of SHG intensity on phase mismatch quantitatively, a solution to the SHG intensity is needed. The SHG intensity in a periodic nonlinear material can be solved by the plane wave expansion method [89]. In this method, the electrical fields and the dielectric function are expanded as Fourier series in the spatial frequency domain. Maxwell's equation is solved algebraically by formulating an eigenvalue problem in the spatial frequency domain. After the fundamental field is solved, it is substituted into the Green's function to obtain the expression of SHG intensity. We only quote the key results that are related with the simulation and experiments in here. More detailed derivation and validation steps are recorded in Appendix B. The SHG intensity in a periodic structure is expressed as [89].

$$|E(2\omega)|^2 = 16\pi^4 \left(\frac{\omega a}{2\pi c} \right)^2 \left(\frac{c}{v_g} \right)^2 |E_{k_2}(r)|^2 |F(k_1, k_2)|^2 \left| \frac{\sin(aN_x \Delta k'_x / 2)}{\sin(a\Delta k'_x / 2)} \right|^2 \left| \frac{\sin(aN_y \Delta k'_y / 2)}{\sin(a\Delta k'_y / 2)} \right|^2 \quad (5.4)$$

The last two function terms in Eq. (5.4) describe the interaction of SHG waves from neighboring cylinders. The N_x and N_y represent the number of cylinders along the lateral and depth direction in the focal volume. When perfect phase matching in the lateral or depth direction is satisfied, meaning $\Delta k'_x$ or $\Delta k'_y$ equal to 0, those terms reduce to N_x^2 or N_y^2 , respectively. The $E_{k_2}(r)$ term describes the distribution of the SHG field in the space. The $F(k_1, k_2)$ function term can be considered as an effective nonlinear susceptibility with respect to the fundamental and SHG fields within a unit cell. It can be expressed as

$$F(k_1, k_2) = \frac{1}{V_0} \int_{V_0} dr' \chi^{(2)} u_{k_2}^*(r') u_{k_1}(r') u_{k_1}(r') \exp(i\Delta k'_x x') \exp(i\Delta k'_y y') \quad (5.5)$$

Here V_0 denotes the volume of the unit cell. The $u_{k_1}(r')$ and $u_{k_2}(r')$ are periodic functions with period a expressing the normalized distribution of the excitation and SHG field, respectively. Next, we focus on the phase matching related terms and simplify Eq. (5.4) into Eq. (5.6) and (5.7).

$$|E(2\omega)|^2 \propto |F(k_1, k_2)|^2 |S(N_x, \Delta k'_x)|^2 |S(N_y, \Delta k'_y)|^2 \quad (5.6)$$

$$S(N_{x(y)}, \Delta k') = \frac{\sin(aN_{x(y)} \Delta k'_{x(y)} / 2)}{\sin(a\Delta k'_{x(y)} / 2)} \quad (5.7)$$

In collagen tissues, the collagen fibrils only occupy part of the tissue in a periodic distribution. Single fibrils are considered as unit cells generating SHG. The SHG intensity generated by a single fibril is calculated by integrating over a unit cell, which is represented by

the $F(k_1, k_2)$ function term. The total SHG is the coherent summation of SHG from all the unit cells within the focal length, which is represented by the $S(N_{x(y)}, \Delta k')$ function terms.

5.3 Simulations

5.3.1 Effect of lattice structure and angle tilting on phase matching for backward SHG

By Eq. (5.2), the optimized excitation and emission angles for achieving perfect phase matching can be obtained for a certain wavelength range. When the angle condition cannot be satisfied or the wavelength is beyond the range, perfect phase matching cannot be achieved and thus the SHG intensity decreases. How does the SHG intensity vary with the angles and wavelength can be simulated according to Eq. (5.1) and (5.6).

In the following simulation, we will investigate the perfect phase matching and non-perfect phase matching scenarios for two excitation wavelengths, 800 and 900 nm. To study the effect of multiple fibrils, the effective nonlinear susceptibility $F(k_1, k_2)$ for a unit cell is simplified to be equal to unity. Other simulation parameters are selected as: $n_{\omega} = n_{2\omega} = 1.45$, spacing $a = 150$ nm is chosen according to an average diameter for mouse tail tendon reported in Ref. [90, 91], $N_x = 4$ and $N_y = 10$ are selected based on a focal depth of ~ 1500 nm and focal width of ~ 600 nm for a typical 40X objective with NA = 0.8.

Fig. 5.2 shows the phase mismatch and SHG intensity as a function of α , θ , and excitation wavelength. Figs. 5.2 (a) and 5.2 (b) show the 2D contour map of phase mismatch $\Delta k'_x$ and $\Delta k'_y$ as a function of α and θ at 800 nm excitation wavelength. For the purpose of normalization, the $\Delta k'_x$ and $\Delta k'_y$ are multiplied by spacing a . The range of α is selected from 0 to 35° because the largest incidence angle provided by a NA = 0.8 objective lens is $\sim 37^\circ$. When θ

$= -\alpha$, phase matching in the lateral direction with $\Delta k'_x = 0$ is satisfied, which is shown as a dark blue band marked by the arrow in Fig. 5.2 (a). According to Eq. (5.3), the longest wavelength that can achieve perfect phase matching is $\lambda_{opt} = 4n_{\omega}a = 870$ nm. For a fundamental wavelength shorter than 870 nm such as 800 nm, two opposite θ angles can satisfy $\Delta k'_y = 0$ for each α , which is illustrated as the “left opened half circle” dark blue band marked by black arrow in Fig. 5.2 (b). Fig. 5.2 (c) shows the 2D contour map for SHG intensity as a function of α and θ . In Fig. 5.2 (c), the highest SHG intensity happens at the crossing point of these two bands, where perfect phase matching with $\Delta k'_x = \Delta k'_y = 0$ are satisfied simultaneously. The optimized θ and α pair for achieving phase matching at $\lambda_{ext} = 800$ nm are $\alpha = 23.4^\circ$ and $\theta = -23.4^\circ$, indicated by the arrow, which can also be verified by Eq. (5.2).

Figs. 5.2 (d) - (f) plot the same contour maps for $\lambda_{ext} = 900$ nm. Fig. 5.2 (d) shows that phase matching in the lateral direction with $\Delta k'_x = 0$ is satisfied when $\theta = -\alpha$. However, there is no selection of α and θ pair that can satisfy perfect phase matching in the y direction because this λ_{ext} is longer than 870 nm. In Fig 5.2 (e), $\Delta k'_y$ is always larger than zero, and the minimum $\Delta k'_y$ appears at $\alpha = \theta = 0^\circ$ and its value increases as α increases. In Fig. 5.2 (f), the highest SHG intensity happens $\alpha = \theta = 0^\circ$, and this SHG intensity is lower than that in Fig. 5.2 (c) because of the phase mismatch.

From the above results, when the λ_{ext} is shorter than $4n_{\omega}a$, perfect phase matching can be achieved with an optimized selection of α and θ given by Eq. (5.2). However, if λ_{ext} is longer than $4n_{\omega}a$, there is no perfect phase matching along the depth direction and the optimized α and θ values are 0° .

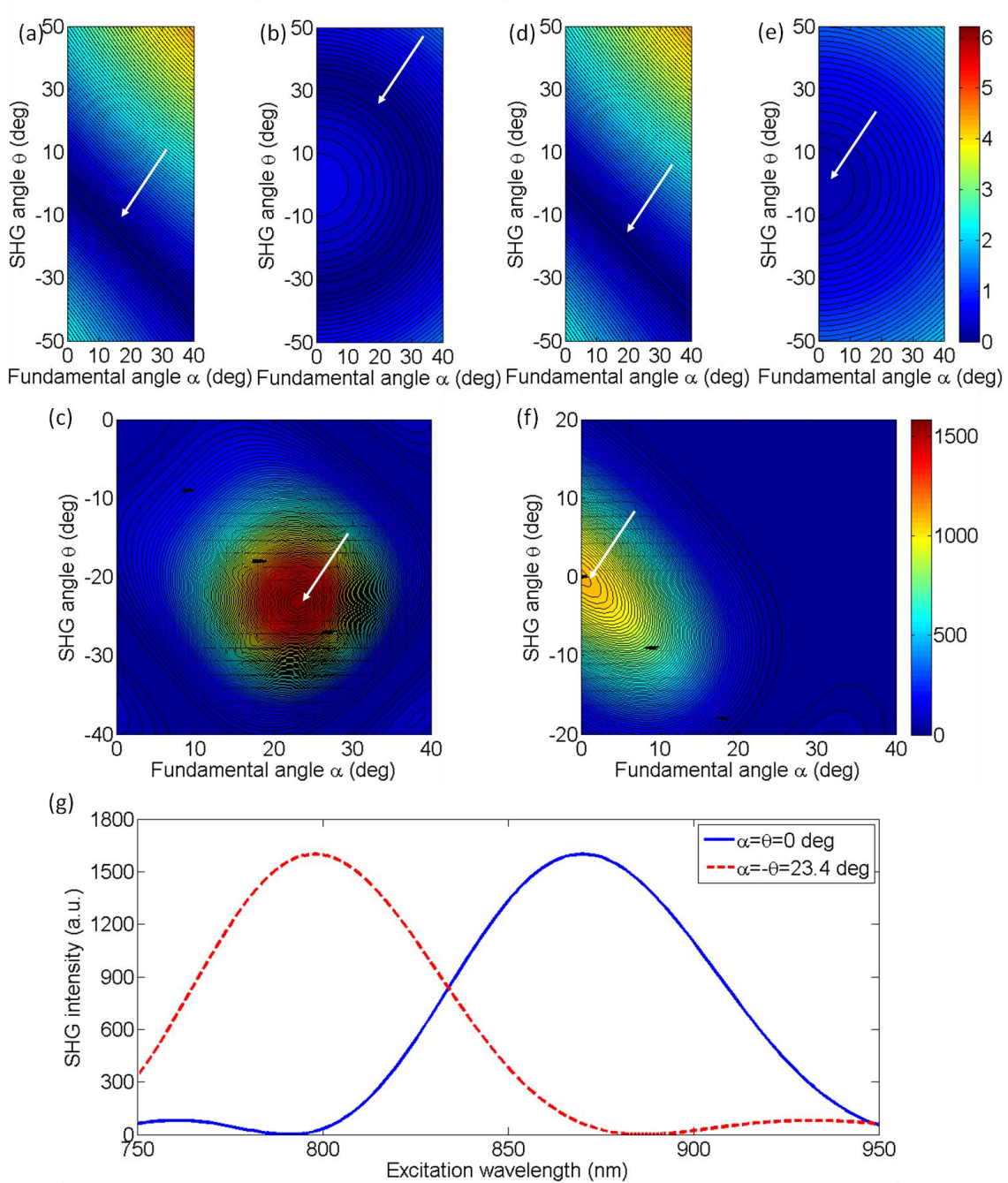


Figure 5.2 The contour map of $\Delta k'_x$, $\Delta k'_x$ and SHG intensity depends on fundamental excitation angle α and SHG emission angle θ for 800 nm excitation wavelength (a)-(c) and 900 nm excitation wavelength (d)-(f). (g) For $\alpha = -\theta = 0^\circ$ and 23.4° , the corresponding SHG intensity from 750 nm to 950 nm. The structure is $N_x = 4$, $N_y = 10$ and $a = 150$ nm.

Fig. 5.2 (g) draws the excitation spectrum when $\alpha = \theta = 0^\circ$ and $\alpha = -\theta = 23.4^\circ$, which shows the intensity variation for wavelength other than 800 and 900 nm in the above two cases. As we have already discussed, the optimum excitation wavelength for these two angle sets are $\lambda_{opt} = 870$ and 800 nm respectively. From the figure, the half intensity bandwidth is approximately 40 nm.

From Eq. (5.4), the SHG intensity is approximately proportional to $N_x^2 N_y^2$ for small phase mismatch. Less number of fibrils in the focal volume results in lower SHG intensity but also flattens dependence on $\Delta k'_x$ and $\Delta k'_y$, which means broader bandwidth of the SHG excitation spectrum. Our model is based on the grating effect in a periodic structure for achieving phase matching. Less number of fibrils reduces the grating effect and eventually violates the assumption for the model. Validation on this issue is not investigated in this chapter and will be studied in the future. In previous literature such as in Ref. 54, longer excitation wavelengths have been used in SHG imaging. To address the phase matching condition at longer wavelengths, modifications to the model will be needed, such as considering some randomness of the periodic structure and different orientations of the wave vectors of the photons in the SHG process.

5.3.2 Effect of single fibril and excitation beam focusing on backward SHG excitation spectrum

As discussed in Section 5.2, the $F(k_1, k_2)$ function describes the SHG intensity from a unit cell consisting of a single fibril. The integration is over a relatively short length of a single fibril diameter, which is comparable with the coherence length of backward SHG. Thus, considerable backward SHG can be generated from the single fibrils. Furthermore, when the fibril spacing and the wavelength satisfy certain relationship, the SHG from individual fibrils can sum up

constructively, resulting in a strong backward SHG. Therefore, the backward SHG generated from a periodic structure can be much stronger than a bulk material with the same total length. For example, if we apply the Eq. (5.5) to two fibrils with diameter 140 nm (average collagen fibrils) and 1500 nm (representing the whole focal volume is occupied by collagen) respectively, their intensity difference is as large as three orders of magnitude. Considering the coherent summation over multiple layers in the focal volume, the intensity increment provided by the periodic structure is even more. This quick estimation demonstrates the importance of periodic structure in backward SHG enhancement.

The combined effect of single unit and periodic structure on the SHG excitation spectrum is demonstrated in Fig. 5.3. Since the wavelength dependence of the $\chi^{(2)}$ is not clear yet, we ignore its wavelength dependency. We choose fibril diameter $d = 140$ nm and spacing $a = 150$ nm to simulate 70% packing ratio in regular tail tendon tissues [92, 93]. The solid green curve represents a plane wave incidence at $\alpha = 0^\circ$ for the fibril structure $N_x = 4, N_y = 10$. The θ angle is kept at 0° . It is found that the impact of single fibril on its peak wavelength is negligible as the peak wavelength for 140 nm diameter fibril keeps as 870 nm. It is because the single fibril's phase matching variation $F(k_1, k_2)^2$ is moderate as shown in dash dot purple in the wavelength range.

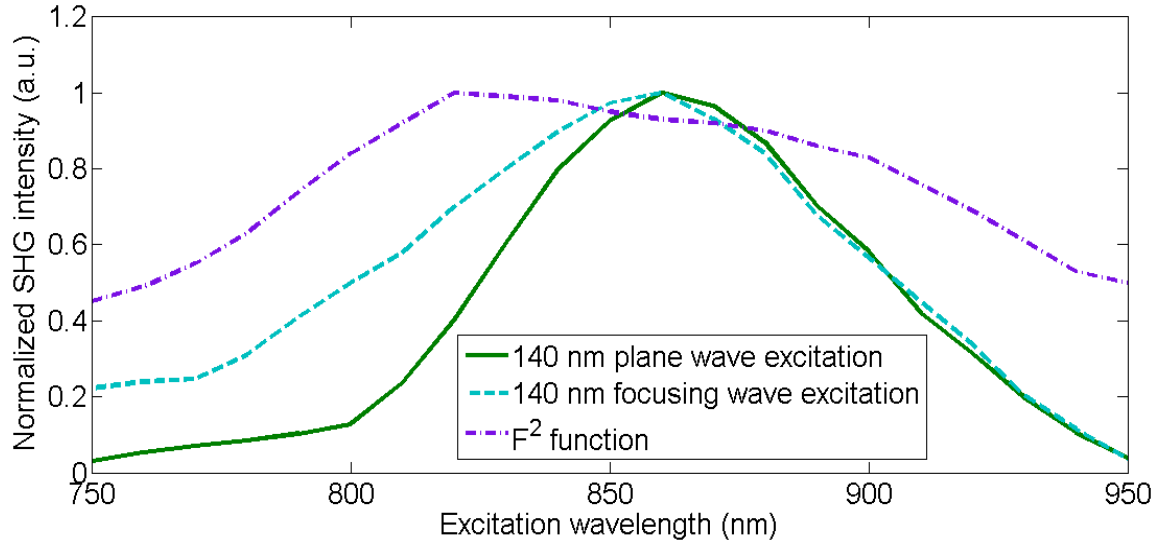


Figure 5.3 The normalized SHG excitation spectrum for fibril diameter $d = 140$ nm, structure $N_x = 4$, $N_y = 10$, without (solid green) and with (dash cyan) focusing. In the non-focusing case, $\alpha = 0^\circ$. The focused beam effect is simulated through summing up the excitation spectrum generated by plane waves with incidence angles vary from 0 to 35° . The wavelength dependence of $F(k_1, k_2)^2$ function is plotted in dash dot purple, which shows the impact of single fibril on excitation spectrum.

In multiphoton microscopy using high NA objectives, the excitation light is focused into a light cone which covers a range of incident angles α . To simulate the excitation spectrum excited by a focused beam, the SHG amplitude $A(r, z)$ under different incident angles α is integrated, where the excitation light is assumed of a Gaussian distribution

$$A(r, z) = \frac{A_0}{1 + 2iz/b} \exp\left(-\frac{r^2}{\omega_0^2(1 + 2iz/b)}\right) \quad (5.8)$$

A_0 is the amplitude at origin. The incident angle α is determined by $\arctan(r/z)$, where r and z are radial and height parameters of the cylindrical coordinate system. In the microscopy configuration, z equals to focal length of the objective lens. The dash cyan curve represents the

normalized excitation spectrum under focused incident light. Confocal parameter $b = 2 \mu\text{m}$ (at 800 nm) and focal spot width $\omega_0 = 0.5 \mu\text{m}$ take typical values of a 40X objective with NA = 0.8. The integration range for α is from 0° to 35° with 5° integration step size.

As discussed in Section 5.3.1, for this fibril structure, perfect phase matching at $\alpha = 0^\circ$ happens at 870 nm wavelength. For wavelength longer than 870 nm, $\alpha = 0^\circ$ is also preferred although no perfect phase matching is obtained. Since Gaussian beam has highest intensity at $\alpha = 0^\circ$, the optimized excitation wavelength does not shift under the focusing condition and the excitation spectrum with and without focusing match closely from the peak position towards longer wavelength. For wavelength shorter than 870 nm, the incident angle α can be increased to maintain perfect phase matching. Therefore, the excitation spectrum with focusing shows higher SHG intensity because of the multiple incident angles provided by the focused Gaussian beam. The half intensity bandwidth increases from 70 nm to 100 nm under focusing. With focused beam incidence, the Gaussian distribution of the intensity among various angle components may alter the α angle that generates the strongest SHG intensity slightly because of a compromise between phase matching and excitation intensity distribution.

5.4 Experiment

5.4.1 Experiment setup and preparation

From the above theoretical and simulation studies, α , θ , fibril spacing a , and excitation wavelength λ_{ext} all affect the phase matching and SHG intensity. Next, we will investigate their effects in experiment. The multiphoton microscopy system has been reported previously in Chapter 3. In order to control the excitation and emission angles, a few sets of rings with

different radii have been designed as shown in Fig. 5.4. The rings can be added in the excitation path, or the emission path, or both to control the excitation and emission angle respectively. The excitation and emission angles can be calculated by $\arctan(r/f)$, in which r is the radius of the ring and f is the focal length. The objective (LUMPLFLN, Olympus, USA) is water-immersion 40× and has NA = 0.8, focal length $f = 4.5$ mm, and radius of back aperture of 3.2 mm.

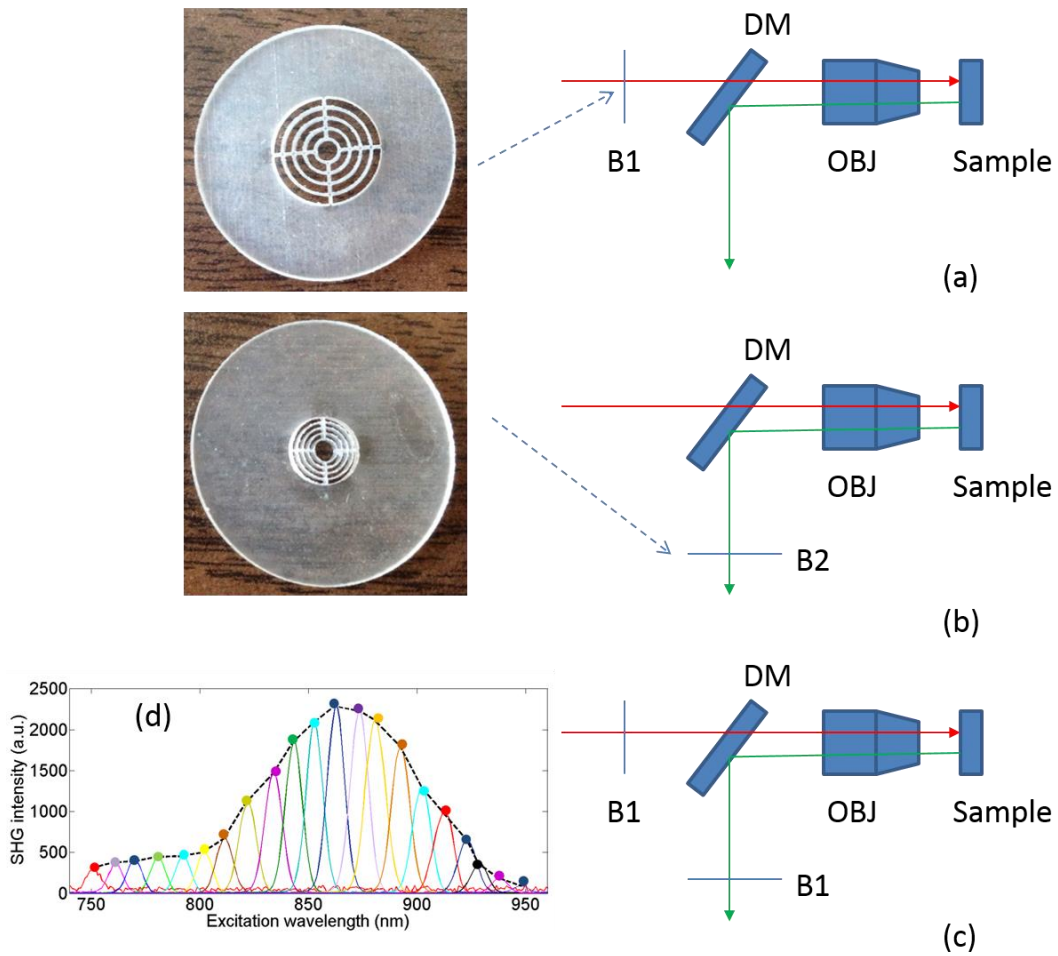


Figure 5.4 Pictures of the ring filters and schematics of their positioning in the beam path for different experiment conditions: (a) filtering the excitation path; (b) filtering the emission path and (c) filtering both excitation and emission path. (d) illustration of SHG excitation spectrum. The solid curve are the SHG emission spectra for different excitation wavelengths from 750 to 950 nm. The dashed line is the SHG excitation spectrum.

Two sets of ring filters are used in this experiment: a larger ring filter set B1 with four concentric rings whose center radii are 1.45, 2.45, 3.45 and 4.45 mm respectively, and the width of the rings is 0.9 mm. For clear and simple denotation, the four rings' radius ranges are described as 1~2, 2~3, 3~4 and 4~5 mm in the following. A smaller ring filter set B2 with four concentric rings whose center radii are 1.2, 1.7, 2.2 and 2.7 mm respectively, and the width of the rings is 0.4 mm. In the same way, the rings' radius ranges are denoted as 1~1.5, 1.5~2, 2~2.5 and 2.5~3 mm. The width of the blocking part between the rings is 0.1 mm. Both ring filters have a 1 mm radius circular hole in the center, which selects the excitation or emission beam near the 0° angle. The ring filters are fabricated by Agile (Uxbridge, ON) using ultra high resolution 3D printing. Light can be selected to pass a particular ring by blocking the other rings with silicone gel temporarily. The substrate of the ring filters and the silicone gel have been examined to not pass light in the fundamental and SHG wavelength bands.

In Fig. 5.4 (a), filter B1 is placed in the excitation path before the dichroic beam splitter (DM) and objective. The center hole is with radius 1 mm ($\alpha = 0^\circ$ to 11°) and the two rings on B1 are used with center radii 1.45 mm ($\alpha = 12^\circ$ to 22°) and 2.45 mm ($\alpha = 23^\circ$ to 32°). In Fig. 5.4 (b), filter B2 is placed in the emission path. The center hole is with radius 1 mm ($-\theta = 0^\circ$ to 11°) and the four rings are used with center radii 1.2 mm ($-\theta = 12^\circ$ to 17°), 1.7 mm ($-\theta = 18^\circ$ to 22°), 2.2 mm ($-\theta = 24^\circ$ to 28°) and 2.7 mm ($-\theta = 29^\circ$ to 33°). In Fig. 5.4 (c), two B1 are placed in the excitation and emission path simultaneously in order to perform angle selection in both excitation and emission directions with center radii 1.45 mm ($\alpha = -\theta = 12^\circ$ to 22°) and 2.45 mm ($\alpha = -\theta = 23^\circ$ to 32°).

Fig. 5. 4 (d) shows how an SHG excitation spectrum is obtained. In the experiments, the excitation laser wavelength is tuned from 750 to 950 nm at 10 nm step size. An SHG emission spectrum (shown as solid curves) is recorded by a spectrometer for each excitation wavelength. The SHG emission wavelength is at exactly half of the excitation wavelength. When the excitation wavelength is tuned, the value of the SHG emission intensity is extracted (marked as solid circles) and plotted as a function of the excitation wavelength. The SHG emission intensity as a function of the excitation wavelength is defined as the SHG excitation spectrum (shown in dashed line). The peak wavelength of the excitation spectrum is the excitation wavelength that produces the strongest SHG intensity. In order to fairly compare the SHG intensity at different excitation wavelength, the calibration procedures described in Chapter 3 are conducted, where the laser excitation power, pulse width, and polarization are maintained to be the same, and the transmission coefficients are calibrated at different wavelength.

The tissue samples are mouse tail tendon from two freshly sacrificed mice. In each mouse, three pieces of thick tissue samples were excised and further sliced into 10 μm thick sections to exclude the scattering effect. In order to reduce the possibility of damaging the tissue, the power shed on the tissue is less than 20 mW. Each measurement at one sample location is repeated three times and the results are averaged. The backward SHG excitation spectrum can vary with tissue samples and locations because of the intrinsic collagen microstructure. Therefore, the excitation spectra shown below are some typical spectra which help with clarifying the concepts and carrying out discussions. Although the excitation spectrum varies from location to location, the variation of the excitation spectrum excited or collected by different rings still show some consistent trend.

We also compare the experiment results with simulations. The tail tendon is simulated by $a = 150$ nm and $d = 140$ nm. Fibril numbers $N_x = 4$, $N_y = 10$ and refractive index $n_\omega = n_{2\omega} = 1.45$ are the same as the parameters in Fig. 5.2. To simulate the angle selection on the excitation and/or emission light by the ring filters, only the light that passing through the angle range defined by the corresponding rings is integrated.

5.4.2 Manipulating the excitation beam angle

The filter setup in Fig. 5.4 (a) is applied to control the excitation beam angle. Fig. 5.5 shows the SHG excitation spectrum from tail tendon excited by the beam without passing the spatial filter, and passing the filter through the center hole (α is 0° to 11°), and two rings of B1 with radius from $1 \sim 2$ mm, $2 \sim 3$ mm (α is 12° to 22° and 23° to 32°), respectively. To demonstrate the peak wavelength change clearly, the normalized spectra are first shown in Fig. 5.5 (a). In Fig. 5.5 (a), The spectrum without any filtering (black) and the spectrum excited by normal incidence beam from the center hole (green) share similar peak wavelength because the dominant excitation power is from the center hole. The red and blue curves represent the spectra excited by the inner and outer rings of B1 and the peak excitation wavelength shift is clear. Since the beam entering from a larger radius ring has a larger α angle, its peak excitation wavelength shifts to a shorter one. Fig. 5.5 (b) plots the actual intensities of the excitation spectra. It shows a decrease of SHG intensity when spatial filters are applied, and the SHG intensity drops more significantly with a larger ring. It also demonstrates that the signal from center hole constitutes a large portion of the total intensity. Since the SHG intensities are excited at different angles, the emitted SHG signals do not overlap spatially and thus they sum up incoherently. The SHG

intensity drop is caused by the energy decrease at a larger incidence angle of the excitation beam which has a Gaussian distribution.

In Fig. 5.5 (c), the SHG excitation spectrum with different excitation angles is simulated. A similar trend of the peak wavelength shifting with increasing excitation angle is obtained.

In bulk SHG crystal, angle tuning is another mechanism of achieving phase matching in forward SHG, when the crystal angle is tuned, the peak excitation wavelength that can generate strong SHG also shifts. However, the angle tuning mechanism may not be able to provide sufficient momentum compensation in backward SHG, where the amount of phase mismatch is dramatic. Meanwhile, the quasi-phase matching mechanism can provide a large amount of momentum compensation in backward SHG due to the virtual momentum from a periodic structure, where the virtual momentum can come from the photonic crystal structure of the collagen fibrils.

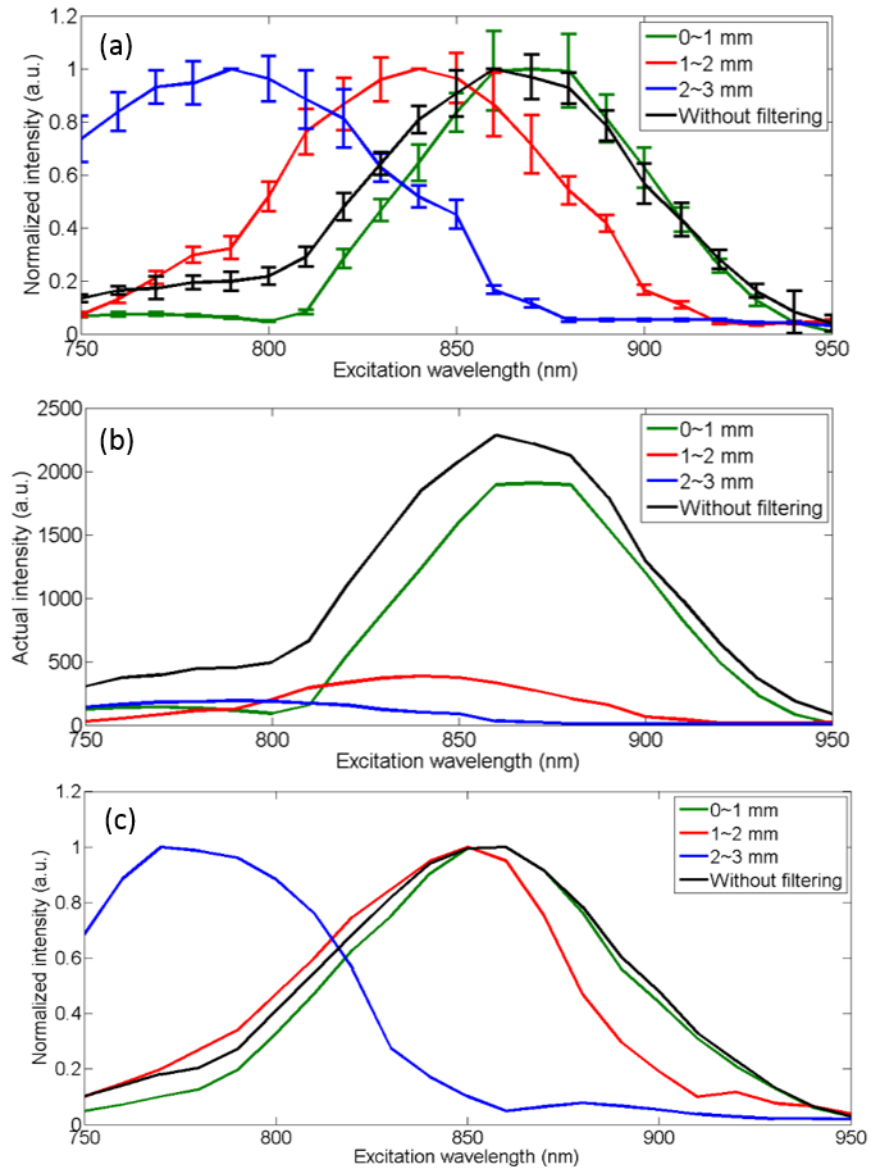


Figure 5.5 (a) The normalized and (b) actual average excitation spectrum of mouse tail tendon with the excitation path filtered by ring filter B1; The results are averaged over three measurements at the same location and the error bar shows the standard deviation. The allowed α angles are 12° to 22° and 23° to 32° . (c) Simulation results with $a = 150$ nm, $d = 140$ nm and fibril numbers $N_x = 4$, $N_y = 10$ for the above angled excitation beams.

5.4.3 Manipulating the emission beam angle

The setup in Fig. 5.4 (b) is used to control the emission beam angle. Figs. 5.6 (a) and (b) plot the normalized and actual SHG excitation spectrum, respectively, from tail tendon when filtering the emission beam angle. In Fig. 5.6 (a), the spectrum shape and peak wavelength from the center hole is similar to the spectrum without any filtering. As expected, from the inner most ring with radius from 1 ~ 1.5 mm ($-\theta$ is 12° to 17°) to the outer most ring with radius from 2.5 ~ 3 mm ($-\theta$ is 29° to 33°), the peak wavelengths of the excitation spectrum shift from 860 nm to 800 nm. By examining ten slices of tissue sections from different parts of the two mice, the average peak wavelength shift is $\sim 70 \pm 20$ nm. In Fig. 5.6 (b), the actual intensity is shown to drop from inner to outer rings. When the emission angle $-\theta$ is increased by applying the rings, the corresponding incident angle α that satisfies phase matching also increases according to $\alpha = -\theta$. Thus, the SHG intensity drop is also caused by the increase of the incident angle of the excitation beam.

In Fig. 5.6 (d), the SHG excitation spectrum with different emission angles is simulated. A similar shift of the peak wavelength with increasing emission angle is obtained. The shift is from 860 nm to 800 nm which is close to the experimental average shift. The excitation focusing beam is simulated through the method explained in Section 5.3.2. The collection of the emission signal by different rings is simulated by integrating the emitted SHG at different angles over the area of the rings.

Another regularly observed spectrum pattern has a falling down trend as shown in Fig. 5.6 (c), where the SHG intensity drops down as the excitation wavelength increases, which has already been reported in Chapter 3. The dropping down trend is more significant for larger radius ring. This pattern may have resulted from an irregularity of the fibril structure in the focal

volume. With fewer numbers of fibrils in the depth or lateral direction, the excitation spectrum is broadened because phase matching condition is relaxed. One of the supporting proves is the relatively lower actual intensity for this pattern than the other type of spectrum. Another possibility is that the peak excitation wavelength may be shorter than 750 nm due to fibril spacing variation. The existence of different patterns of excitation spectra in tail tendon shows the complexity of collagen structures in tissues, which deserves further investigation.

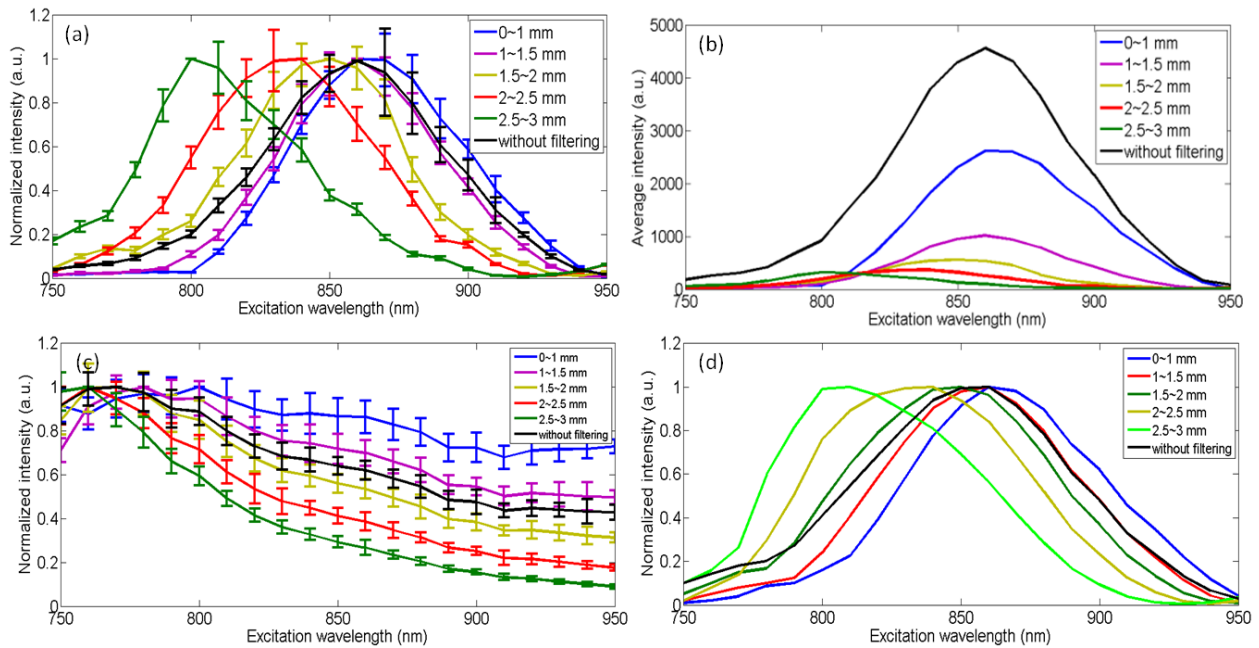


Figure 5.6 One typical type of the (a) normalized and (b) actual average excitation spectrum of mouse tail tendon with the emission path filtered by ring filter B2; (c) another typical type of the normalized excitation spectrum; (d) simulation for the experiment results in (a) with $a = 150$ nm, $d = 140$ nm and fibril numbers $N_x = 4$, $N_y = 10$ for focused excitation beam. When the emission path is filtered, the allowed $-\theta$ angles are 0° to 11° , 12° to 17° , 18° to 22° , 24° to 28° and 29° to 33° .

5.4.4 The impact of different fibril diameter

Achilles tendon that has a different fibril diameter is also investigated. Fig. 5.7 (a) and (b) plot the excitation spectrum from Achilles tendon filtered the same way as Fig. 5.6. The major result difference between the two types of tissues is the spread of the excitation spectra's peak wavelengths with emission angle increasing. Unlike in tail tendon, the peak wavelengths shift from 840 to 800 nm with the same ring radius increasing in Achilles tendon. The average peak wavelengths shift is 40 ± 11 nm by measuring ten slices of samples, but the shift is 70 ± 20 nm for tail tendon.

In Fig. 5.6 (d) and Fig. 5.7 (c), the shift of peak wavelengths with increasing emission angle is simulated for the two types of tendons respectively. The simulated peak wavelength shift is from 860 nm to 800 nm in tail tendon and is from 800 to 760 nm in Achilles tendon. The narrower shift for Achilles tendon is explained as follows. According to Eq. (5.2) and Eq. (5.3), for a smaller $d = 110$ nm representing Achilles tendon, the optimized excitation wavelength is shorter than the 750 nm [92]. Therefore, the bump appears in the wavelength range longer than 750 nm in the experiment may appear to be the first side lobe in the simulated excitation spectrum. Hence, the θ angle providing optimized phase matching selection for the side lobe is not as strict as the main peak. As a result, the optimized excitation wavelength from different emission angles does not vary much for a smaller spacing a .

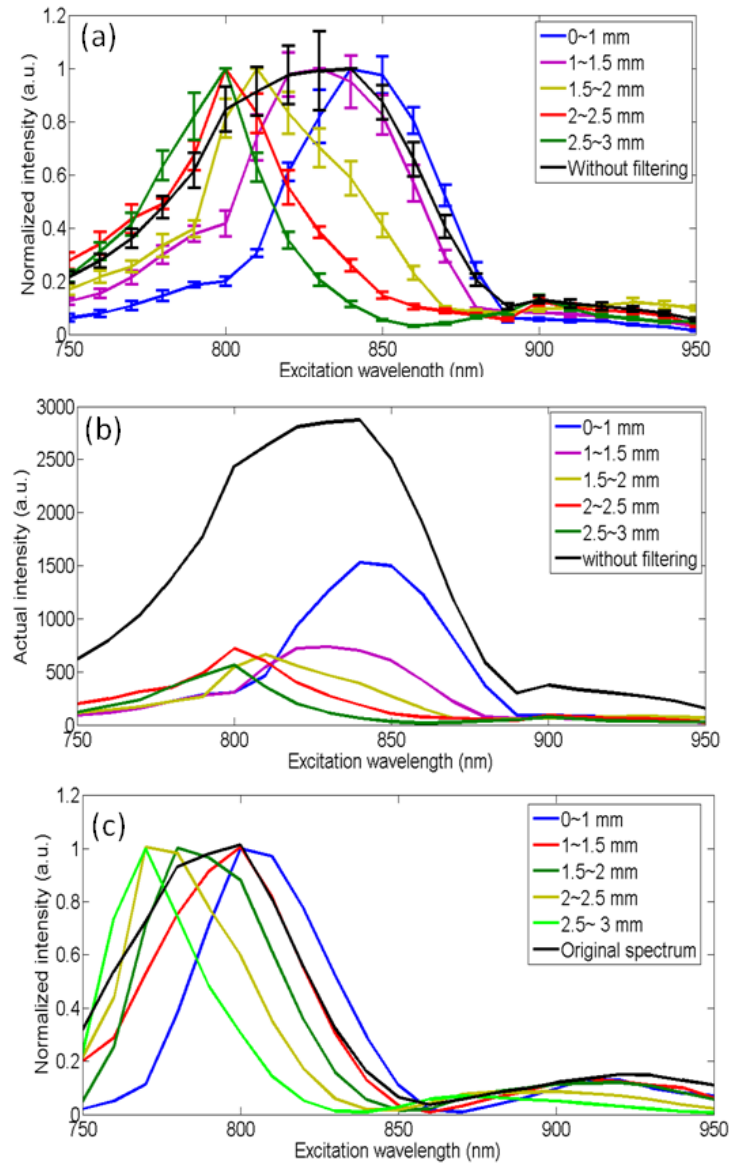


Figure 5.7 (a) Normalized and (b) actual average excitation spectrum of mouse Achilles tendon with the emission path filtered by ring filter B2; (c) simulation for the experiment results in (a) with $a = 120$ nm, $d = 110$ nm and fibril numbers $N_x=4$, $N_y=10$. When the emission path is filtered, the allowed θ angles are 12° to 17° , 18° to 22° , 24° to 28° and 29° to 33° .

5.4.5 Manipulating both the excitation and emission angle

Lastly, we follow the setup in Fig. 5.4 (c) and use two B1 filters in the excitation and emission path respectively to measure the excitation spectrum of the tail tendon samples. The center hole of B1 is not used. In emission and excitation, we use the same radii rings with radius from 1 ~ 2 mm, 2 ~ 3 mm (α is 12° to 22° and 23° to 32°) at the same time in order to confine the excitation and emission angle to be the same. In Fig. 5.8 (a), the two excitation spectra obtained from the two rings are observed to peak at 810 and 850 nm, respectively. Since the excitation and collection angles are the same, the phase matching condition in this experiment is tentatively explained by Eq. (5.2). In order to verify which angle component is the source of the collected emission signal, we also measure the spectrum by removing the excitation filter but keep the emission filter. The results are shown in solid curves in Fig. 5.8 (a). After removing the excitation filter, the peak wavelength of the SHG excitation spectrum is still at 810 and 860 nm, respectively, except that the bandwidth is slightly broadened. The similar SHG excitation spectrum with and without the spatial filtering in the excitation path indicates that the main contributing angle component in the excitation comes from $\alpha = -\theta$. This result shows that angle components in the focused beam contribute to the phase matching for certain excitation wavelength.

Fig. 5.8 (b) shows the simulation results under a similar condition as in the experiment where the spatial filtering is applied or removed in the excitation beam path. The unchanged peak wavelength as well as the effect of bandwidth broadening due to the removal of B1 filter in the excitation path is very similar as the experiment results.

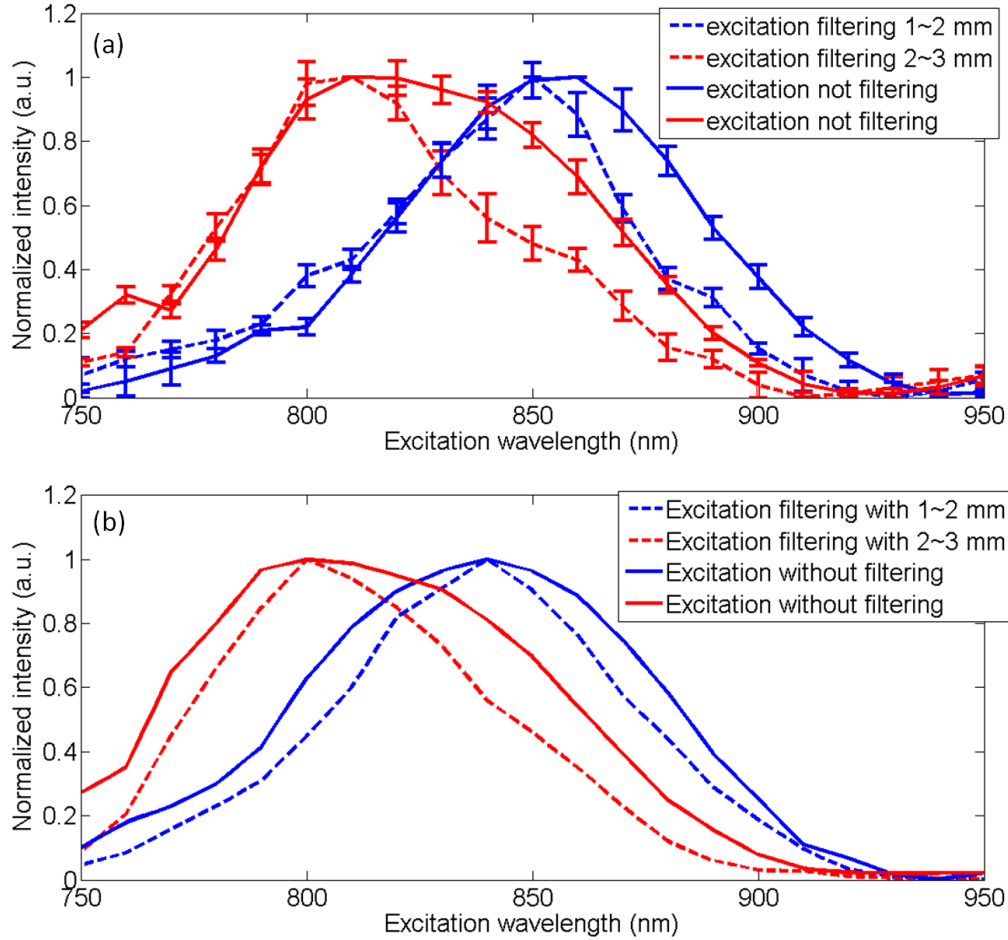


Figure 5.8 (a) Experimental results of the normalized excitation spectrum comparison with different filtering setups for mouse tail tendon; (b) Simulation results with (dash) and without (solid) excitation path filtering. $a = 150$ nm and $d = 140$ nm with fibril numbers $N_x = 4$, $N_y = 10$. When the excitation beam is filtered by the rings, the allowed α angles are 12° to 22° and 23° to 32° .

5.5 Conclusions

In this chapter, we present a theoretical framework aiming at explaining the mechanism of backward SHG in collagen tissues. It is based on the assumption that the phase matching in the backward direction can be assisted by the virtue momentum provided by the lattice structure consisted of the collagen fibrils. By tilting the fundamental and SHG wave vector angles,

optimized phase matching can be achieved for particular excitation wavelengths. A larger angle corresponds to a shorter optimized excitation wavelength. Using plane wave expansion method, the backward SHG intensity in a periodic structure like collagen is solved so that the effect of angle tilting on phase matching is quantitatively evaluated. Besides lattice structure, the effect of focusing excitation on backward SHG is also analyzed. The excitation spectrum with focusing shows higher SHG intensity at wavelength shorter than peak wavelength because of the multiple incident angles provided by the focused Gaussian beam. In experiment, through filtering the incident and emission angle of the excitation or emission beam by concentric rings, the relation among the incident, emission angles, and peak excitation wavelength is validated. The variations of excitation spectrum with excitation and emission angles are well explained by our theoretical model and numerical simulations.

Chapter 6: Summaries and future work

6.1 Summaries

SHG microscopy is a powerful tool to image collagen tissues. Both forward and backward detection configurations have been utilized. For imaging thick tissues and tissues *in vivo*, the backward detection configuration is particularly necessary. However, currently there is a lack of understanding about the mechanism of the backward SHG in collagen tissues. In this work, we study the SHG in collagen tissues. Its optic characteristics and backward phase matching mechanism are investigated.

We investigate the phase matching mechanism of backward SHG in collagen in a framework of quasi-phase matching. As supportive evidences to this, wavelength dependence of backward SHG and its scattering properties are studied. Quantifying the scattered and generated SHG in the backward direction shows the necessity of carrying out investigations on the mechanism of generating backward SHG. The wavelength dependence spectrum measurement provides a tool to analyze the phase matching issue.

The wavelength dependence of SHG is an important optic characteristic. A typical SHG excitation spectrum shows a single peak shape. Our measurement results for mouse tail tendon and Achilles tendon show a different peak wavelength range between them. Another frequently observed pattern is the monotonic decreasing intensity, which may originate from local microstructure variation. The wavelength dependence measurement is a useful tool to analyze the backward phase matching of SHG. For example, the optimized excitation wavelength in Chapter 5 is determined according to the peak wavelength of the excitation spectrum. Since there are many system factors that affect the measurements, calibration procedures are necessary.

Factors that are affected by wavelength include the focal volume, laser power and pulse duration, and transmission of the optic components. The accuracy of the calibration procedure is proved by measuring the SHG wavelength dependence in a BBO crystal. The agreement between theory and experiment for the BBO crystal demonstrates that our proposed method can be used as a validation method when investigating the wavelength dependence of SHG from biological tissues.

In order to differentiate the proportion of backward scattered (BS-SHG) and backward generated SHG (BG-SHG) among the total collected SHG in the backward direction, we use a pinhole method to investigate the scattering properties of SHG in the mouse tail tendon and Achilles tendon based on confocal multiphoton microscopy. Our Monte Carlo simulation proves that the two types of backward SHG contrast, e.g. BG-SHG and BS-SHG can be modeled as Gaussian distribution and uniform distribution respectively in the pinhole detection plane. Following this model, the spot width and the relative intensity of the two types of SHG are obtained in experiment. This pinhole method is noninvasive and requires little sample preparation. It is found that in a 300 μm thick tissue, BS-SHG accounts for 15% and 60% of the total backward SHG in the tail tendon and Achilles tendon respectively. This difference between the two types of collagen tissues is qualitatively explained by the scattering coefficient and F/B intensity ratio of the two tissues.

To understand the strong backward SHG observed in SHG microscopy, we propose a theoretical framework aiming at explaining the generation mechanism of backward SHG. We demonstrate in principle that the phase matching in the backward direction can be assisted by the virtue momentum provided by the lattice structure. Through tilting the fundamental and SHG wave vector angles, optimized phase matching is achieved. By plane wave expansion method,

the backward SHG intensity in a periodic structure is solved so that the effect of angle tilting is quantitatively discussed in the perfect phase matching and non-perfect phase matching conditions. Besides lattice structure, the effect of fibril size is also analyzed, whose general characteristic is similar to bulk material. In order to verify the phase matching and angle tilting effect, experiments are carried out using spatial filters. It is found that when the excitation or emission path is filtered, the optimized excitation wavelength of the emitted SHG signal shifts to shorter wavelength when the collection ring radius increases. Through comparing the optimized excitation wavelength with and without emission path filtering, it is validated that angled components of the focused beam is the source of emitted SHG at certain wavelength. These results validate our hypothesis about the backward phase matching in a periodic structure such as collagen. Our investigation towards phase matching of backward SHG provides a possible explanation about the efficient backward SHG in collagen.

Potential biological and medical application of the work relies on the hypothesis that we can find a link between the variations of collagen structure and some consistent optical measurement. Understanding the mechanism of the backward SHG phase matching is the first step of relating the fibril properties such as its diameter with backward SHG signal properties. Through this work, we have built a connection between fibril diameter and peak wavelength of the wavelength dependence curve in preliminary.

6.2 Future work

One limitation of the current study is that the information about the collagen microstructure in the focal volume is not measured directly. For the time being, we use different types of tissues to obtain different fibril diameters and spacing for the investigation of phase

matching. The average values of the fibril diameter and spacing are obtained from literature. However, the exact fibril diameter and local fibril packing organization are not known, which can also vary from location to location. Building a clear connection between the SHG signal properties and fibril microstructure properties requires two issues to be solved. One issue is to be able to acquire more accurate information about the fibril microstructure, especially from the same location where SHG is characterized. The other issue is to be able to control the fibrils to obtain different diameters in a more accurate and consistent way.

Electron microscopy can be used to obtain a more accurate spacing or fibril thickness. Currently, there has been reports that correlative confocal or SHG microscopy with electron microscopy is applied on fibril imaging so that fibrils can be visualized by the two contrasts at the same time [94]. Acquiring SHG and electron microscopy simultaneously will help improve the correlation between the SHG properties and collagen microstructure more accurately. Additionally, it has been reported that immersing collagen in sodium chloride (NaCl) solution can change the fibril thickness and further affect the F/B intensity ratio [52]. It is predicted that the solution ionic strength introduces a variation of the shell thickness of the fibril. Through precisely varying the fibril thickness or spacing, the investigation of the phase matching problem can be investigated more thoroughly.

The refractive index and nonlinear coefficient are other key factors that contribute to the wavelength dependent SHG excitation spectrum [95, 96]. Currently, we assume that the refractive index in the collagen fibrils and the interspace between fibrils are the same. The nonlinear coefficients are also assumed to be constant over a wide wavelength range. The theoretical and simulation work can be improved if these parameters can be treated more

accurately. Better understanding about SHG can be obtained if those optical properties can be further quantified experimentally.

In Chapter 5, we demonstrate that the backward generated SHG is angle dependent by using rings with different radius to differentiate the signal emitted from different angles. However, the achievable dimension of the spatial ring filter is limited by the 3D printing, where the rings can't be printed to be very thin. The positioning of the ring filter is manually controlled by a micrometer and its relative position with the center of the beam may not be very accurate. Better design and manufacture of the spatial filters, and controlling of the position of the filters will improve the accuracy and sensitive of the angle depended SHG measurement. This type of angle dependent SHG measurement could open a new possibility of probing the collagen microstructure.

Bibliography

1. J. Riesle, A. Hollander, R. Langer, L. Freed, and G. Vunjak - Novakovic, "Collagen in tissue - engineered cartilage: Types, structure, and crosslinks". *Journal of cellular biochemistry*, 1998. **71**(3): p. 313-327.
2. Y. Komai and T. Ushiki, "The three-dimensional organization of collagen fibrils in the human cornea and sclera". *Investigative ophthalmology & visual science*, 1991. **32**(8): p. 2244-2258.
3. S. Gay, P. Müller, C. Lemmen, K. Remberger, K. Matzen, and K. Kühn, "Immunohistological study on collagen in cartilage-bone metamorphosis and degenerative osteoarthritis". *Klinische Wochenschrift*, 1976. **54**(20): p. 969-976.
4. W. Dan, Z. Li, L. Liao, M. CHEN, R. ZENG, N.-h. DAN, C. CHEN, F. LIN, and H. LIN. "Skin collagen and its application in tissue engineering". in *The Fifth Asi-an International Conference of Leather Science and Tech-nology*. 2002.
5. S.H. Liu, R.-S. Yang, R. Al-Shaikh, and J.M. Lane, "Collagen in tendon, ligament, and bone healing: a current review". *Clinical orthopaedics and related research*, 1995. **318**: p. 265-278.
6. G. Chen, T. Sato, T. Ushida, N. Ochiai, and T. Tateishi, "Tissue engineering of cartilage using a hybrid scaffold of synthetic polymer and collagen". *Tissue engineering*, 2004. **10**(3-4): p. 323-330.
7. R. Milch, "Studies of collagen tissue aging: interaction of certain intermediary metabolites with collagen". *Gerontology*, 1963. **7**(3): p. 129-152.
8. C.J. Doillon and F.H. Silver, "Collagen-based wound dressing: Effects of hyaluronic acid and firponectin on wound healing". *Biomaterials*, 1986. **7**(1): p. 3-8.
9. P. Fratzl, "*Collagen: structure and mechanics*". 2008: Springer Science & Business Media.
10. D.J. Prockop, K.I. Kivirikko, L. Tuderman, and N.A. Guzman, "The biosynthesis of collagen and its disorders (second of two parts)". *The New England journal of medicine*, 1979. **301**(2): p. 77.
11. J. Prockop, "Collagens: molecular biology, diseases, and potentials for therapy". *Annual review of biochemistry*, 1995. **64**(1): p. 403-434.
12. P.P. Provenzano, D.R. Inman, K.W. Eliceiri, J.G. Knittel, L. Yan, C.T. Rueden, J.G. White, and P.J. Keely, "Collagen density promotes mammary tumor initiation and progression". *BMC medicine*, 2008. **6**(1): p. 11.
13. K. Kobayashi, K. Miyata, and T. Iino, "Three-dimensional structures of the connective tissue papillae of the tongue in newborn dogs". *Archivum histologicum Japonicum=Nihon soshikigaku kiroku*, 1987. **50**(3): p. 347-357.
14. 大谷修, "Three-dimensional organization of the connective tissue fibers of the human pancreas: a scanning electron microscopic study of NaOH treated-tissues". *Archivum histologicum japonicum*, 1987. **50**(5): p. 557-566.
15. C.H. Gerould, "Ultramicrostructures of the human tooth as revealed by the electron microscope". *Journal of Dental Research*, 1944. **23**(4): p. 239-245.

16. K. Kanaya, Y. Muranaka, and H. Fujita, "Uncoated observation and etching of non-conductive materials by ion beam bombardment in scanning electron microscopy". *Scanning electron microscopy*, 1981(Pt 4): p. 1379-1394.
17. S. Lewis, J. Osborn, and P. Stuart, "Demonstration of an internal structure within the red blood cell by ion etching and scanning electron microscopy". 1968.
18. B. Drake, C. Prater, A. Weisenhorn, S. Gould, T. Albrecht, C. Quate, D. Cannell, H. Hansma, and P. Hansma, "Imaging crystals, polymers, and processes in water with the atomic force microscope". *Science*, 1989. **243**(4898): p. 1586-1589.
19. P. Frederix, T. Akiyama, U. Staufer, C. Gerber, D. Fotiadis, D. Müller, and A. Engel, "Atomic force bio-analytics". *Current opinion in chemical biology*, 2003. **7**(5): p. 641-647.
20. P. Dolber and M. Spach, "Conventional and confocal fluorescence microscopy of collagen fibers in the heart". *Journal of Histochemistry & Cytochemistry*, 1993. **41**(3): p. 465-469.
21. A. Young, I. LeGrice, M. Young, and B. Smaill, "Extended confocal microscopy of myocardial laminae and collagen network". *Journal of Microscopy*, 1998. **192**(2): p. 139-150.
22. H. Puchtler, S. Meloan, and F. Waldrop, "Are picro-dye reactions for collagens quantitative?". *Histochemistry*, 1988. **88**(3-6): p. 243-256.
23. P. Stoller, K.M. Reiser, P.M. Celliers, and A.M. Rubenchik, "Polarization-modulated second harmonic generation in collagen". *Biophysical journal*, 2002. **82**(6): p. 3330-3342.
24. S. Roth and I. Freund, "Second harmonic generation in collagen". *The Journal of chemical physics*, 1979. **70**(4): p. 1637-1643.
25. G. Cox, E. Kable, A. Jones, I. Fraser, F. Manconi, and M.D. Gorrell, "3-dimensional imaging of collagen using second harmonic generation". *Journal of structural biology*, 2003. **141**(1): p. 53-62.
26. E. Brown and T. McKee, "Dynamic imaging of collagen and its modulation in tumors in vivo using second-harmonic generation". *Nature medicine*, 2003. **9**(6): p. 796-800.
27. S. Bancelin, C. Aimé, I. Gusachenko, L. Kowalczyk, G. Latour, T. Coradin, and M.-C. Schanne-Klein, "Determination of collagen fibril size via absolute measurements of second-harmonic generation signals". *Nature communications*, 2014. **5**.
28. P.-J. Su, W.-L. Chen, T.-H. Li, C.-K. Chou, T.-H. Chen, Y.-Y. Ho, C.-H. Huang, S.-J. Chang, Y.-Y. Huang, and H.-S. Lee, "The discrimination of type I and type II collagen and the label-free imaging of engineered cartilage tissue". *Biomaterials*, 2010. **31**(36): p. 9415-9421.
29. G.C. Cox, P. Xu, C.J. Sheppard, and J.A. Ramshaw. "Characterization of the second harmonic signal from collagen". in *Biomedical Optics 2003*. 2003. International Society for Optics and Photonics.
30. X. Chen, O. Nadiarynkh, S. Plotnikov, and P.J. Campagnola, "Second harmonic generation microscopy for quantitative analysis of collagen fibrillar structure". *Nature protocols*, 2012. **7**(4): p. 654-669.
31. W.R. Zipfel, R.M. Williams, and W.W. Webb, "Nonlinear magic: multiphoton microscopy in the biosciences". *Nature biotechnology*, 2003. **21**(11): p. 1369-1377.

32. P. Theer, M.T. Hasan, and W. Denk, "Two-photon imaging to a depth of 1000 μm in living brains by use of a Ti: Al₂O₃ regenerative amplifier". *Optics letters*, 2003. **28**(12): p. 1022-1024.
33. A. Diaspro, "*Confocal and two-photon microscopy: foundations, applications, and advances*". Vol. 1. 2002: Wiley-Liss New York.
34. P.J. Campagnola and C.Y. Dong, "Second harmonic generation microscopy: principles and applications to disease diagnosis". *Laser & Photonics Reviews*, 2011. **5**(1): p. 13-26.
35. G. Latour, I. Gusachenko, L. Kowalczyk, I. Lamarre, and M.C. Schanne-Klein, "In vivo structural imaging of the cornea by polarization-resolved second harmonic microscopy". *Biomedical optics express*, 2012. **3**(1): p. 1-15.
36. S. Psilodimitrakopoulos, D. Artigas, G. Soria, I. Amat-Roldan, A.M. Planas, and P. Loza-Alvarez, "Quantitative discrimination between endogenous SHG sources in mammalian tissue, based on their polarization response". *Optics express*, 2009. **17**(12): p. 10168-10176.
37. S. Brasselet, D. Ait-Belkacem, A. Gasecka, F. Munhoz, S. Brustlein, and S. Brasselet, "Influence of birefringence on polarization resolved nonlinear microscopy and collagen SHG structural imaging". *Optics express*, 2010. **18**(14): p. 14859-14870.
38. G. Latour, I. Gusachenko, L. Kowalczyk, I. Lamarre, and M.-C. Schanne-Klein, "In vivo structural imaging of the cornea by polarization-resolved second harmonic microscopy". *Biomedical optics express*, 2012. **3**(1): p. 1-15.
39. R. Ambekar, T.-Y. Lau, M. Walsh, R. Bhargava, and K.C. Toussaint, "Quantifying collagen structure in breast biopsies using second-harmonic generation imaging". *Biomedical optics express*, 2012. **3**(9): p. 2021-2035.
40. T. Hompland, A. Erikson, M. Lindgren, T. Lindmo, and C. de Lange Davies, "Second-harmonic generation in collagen as a potential cancer diagnostic parameter". *Journal of biomedical optics*, 2008. **13**(5): p. 054050-054050-11.
41. P.-S. Hu, C.-M. Hsueh, P.-J. Su, W.-L. Chen, V.A. Hovhannisyan, S.-J. Chen, T.-H. Tsai, and C.-Y. Dong, "The Use of Second-Order Susceptibility as Contrast Mechanism for Label-Free Imaging of Biological Tissue". *Selected Topics in Quantum Electronics, IEEE Journal of*, 2012. **18**(4): p. 1326-1334.
42. S.V. Plotnikov, A.C. Millard, P.J. Campagnola, and W.A. Mohler, "Characterization of the myosin-based source for second-harmonic generation from muscle sarcomeres". *Biophysical journal*, 2006. **90**(2): p. 693-703.
43. L. Moreaux, O. Sandre, S. Charpak, M. Blanchard-Desce, and J. Mertz, "Coherent scattering in multi-harmonic light microscopy". *Biophysical journal*, 2001. **80**(3): p. 1568-1574.
44. P.J. Campagnola and L.M. Loew, "Second-harmonic imaging microscopy for visualizing biomolecular arrays in cells, tissues and organisms". *Nature biotechnology*, 2003. **21**(11): p. 1356-1360.
45. I. Freund, M. Deutsch, and A. Sprecher, "Connective tissue polarity. Optical second-harmonic microscopy, crossed-beam summation, and small-angle scattering in rat-tail tendon". *Biophysical journal*, 1986. **50**(4): p. 693-712.
46. F. Vanzi, L. Sacconi, R. Cicchi, and F.S. Pavone, "Protein conformation and molecular order probed by second-harmonic-generation microscopy". *Journal of biomedical optics*, 2012. **17**(6): p. 0609011-0609018.

47. P. Bianchini and A. Diaspro, "Three - dimensional (3D) backward and forward second harmonic generation (SHG) microscopy of biological tissues". *Journal of biophotonics*, 2008. **1**(6): p. 443-450.
48. J. Adur, H.F. Carvalho, C.L. Cesar, and V.H. Casco, "Nonlinear Optical Microscopy Signal Processing Strategies in Cancer". *Cancer informatics*, 2014. **13**: p. 67.
49. P. Stoller, P.M. Celliers, K.M. Reiser, and A.M. Rubenchik, "Quantitative second-harmonic generation microscopy in collagen". *Applied optics*, 2003. **42**(25): p. 5209-5219.
50. F. Légaré, C. Pfeffer, and B.R. Olsen, "The role of backscattering in SHG tissue imaging". *Biophysical journal*, 2007. **93**(4): p. 1312-1320.
51. O. Nadiarnykh, R.B. LaComb, P.J. Campagnola, and W.A. Mohler, "Coherent and incoherent SHG in fibrillar cellulose matrices". *Optics express*, 2007. **15**(6): p. 3348-3360.
52. R.M. Williams, W.R. Zipfel, and W.W. Webb, "Interpreting second-harmonic generation images of collagen I fibrils". *Biophysical journal*, 2005. **88**(2): p. 1377-1386.
53. J. Mertz and L. Moreaux, "Second-harmonic generation by focused excitation of inhomogeneously distributed scatterers". *Optics communications*, 2001. **196**(1): p. 325-330.
54. S. Chu, "Quantitative analysis of backward generation and backscattering for epically collected second harmonic generation in biological tissues". *Journal of Medical and Biological Engineering*, 2007. **27**(4): p. 177.
55. S.-P. Tai, T.-H. Tsai, W.-J. Lee, D.-B. Shieh, Y.-H. Liao, H.-Y. Huang, K. Zhang, H.-L. Liu, and C.-K. Sun, "Optical biopsy of fixed human skin with backward-collected optical harmonics signals". *Optics express*, 2005. **13**(20): p. 8231-8242.
56. M. Han, G. Giese, and J. Bille, "Second harmonic generation imaging of collagen fibrils in cornea and sclera". *Optics Express*, 2005. **13**(15): p. 5791-5797.
57. R. LaComb, O. Nadiarnykh, and P.J. Campagnola, "Quantitative second harmonic generation imaging of the diseased state osteogenesis imperfecta: experiment and simulation". *Biophysical journal*, 2008. **94**(11): p. 4504-4514.
58. S.-W. Chu, S.-P. Tai, M.-C. Chan, C.-K. Sun, I. Hsiao, C.-H. Lin, Y.-C. Chen, and B.-L. Lin, "Thickness dependence of optical second harmonic generation in collagen fibrils". *Optics express*, 2007. **15**(19): p. 12005-12010.
59. C. Pouya, D. Stavenga, and P. Vukusic, "Discovery of ordered and quasi-ordered photonic crystal structures in the scales of the beetle *Eupholus magnificus*". *Optics express*, 2011. **19**(12): p. 11355-11364.
60. R. LaComb, O. Nadiarnykh, S.S. Townsend, and P.J. Campagnola, "Phase matching considerations in second harmonic generation from tissues: effects on emission directionality, conversion efficiency and observed morphology". *Optics communications*, 2008. **281**(7): p. 1823-1832.
61. L. Tian, H. Wei, Y. Jin, H. Liu, Z. Guo, and X. Deng, "Backward emission angle of microscopic second-harmonic generation from crystallized type I collagen fiber". *Journal of biomedical optics*, 2011. **16**(7): p. 075001-075001-8.
62. M.M. Fejer, G. Magel, D.H. Jundt, and R.L. Byer, "Quasi-phase-matched second harmonic generation: tuning and tolerances". *Quantum Electronics, IEEE Journal of*, 1992. **28**(11): p. 2631-2654.

63. P. Franken, A. Hill, C. Peters, and G. Weinreich, "Generation of optical harmonics". *Physical Review Letters*, 1961. **7**(4): p. 118-119.
64. R.W. Boyd, "*Nonlinear optics*". 2003: Academic press.
65. M.C. Teich and B. Saleh, "Fundamentals of photonics". Canada, Wiley Interscience, 1991: p. 3.
66. A. Fiore, V. Berger, E. Rosencher, P. Bravetti, and J. Nagle, "Phase matching using an isotropic nonlinear optical material". *Nature*, 1998. **391**(6666): p. 463-466.
67. G. Hall, K.B. Tilbury, K.R. Campbell, K.W. Eliceiri, and P.J. Campagnola, "Experimental and simulation study of the wavelength dependent second harmonic generation of collagen in scattering tissues". *Optics letters*, 2014. **39**(7): p. 1897-1900.
68. H. Askew and S. Matcher. "Investigation of the wavelength dependence of SHG from various tissues". in *SPIE BiOS*. 2012. International Society for Optics and Photonics.
69. J.A. Palero, H.S. De Bruijn, H.J. Sterenborg, and H.C. Gerritsen, "Spectrally resolved multiphoton imaging of in vivo and excised mouse skin tissues". *Biophysical journal*, 2007. **93**(3): p. 992-1007.
70. T.A. Theodossiou, C. Thrasivoulou, C. Ekwobi, and D.L. Becker, "Second harmonic generation confocal microscopy of collagen type I from rat tendon cryosections". *Biophysical journal*, 2006. **91**(12): p. 4665-4677.
71. W.R. Zipfel, R.M. Williams, R. Christie, A.Y. Nikitin, B.T. Hyman, and W.W. Webb, "Live tissue intrinsic emission microscopy using multiphoton-excited native fluorescence and second harmonic generation". *Proceedings of the National Academy of Sciences*, 2003. **100**(12): p. 7075-7080.
72. A. Zoumi, A. Yeh, and B.J. Tromberg, "Imaging cells and extracellular matrix in vivo by using second-harmonic generation and two-photon excited fluorescence". *Proceedings of the National Academy of Sciences*, 2002. **99**(17): p. 11014-11019.
73. J.-X. Cheng, A. Volkmer, and X.S. Xie, "Theoretical and experimental characterization of coherent anti-Stokes Raman scattering microscopy". *JOSA B*, 2002. **19**(6): p. 1363-1375.
74. G. Boyd and D. Kleinman, "Parametric interaction of focused Gaussian light beams". *Journal of Applied Physics*, 1968. **39**(8): p. 3597-3639.
75. D. Edelstein, E. Wachman, and C. Tang, "Broadly tunable high repetition rate femtosecond optical parametric oscillator". *Applied Physics Letters*, 1989. **54**(18): p. 1728-1730.
76. K. Kato, "Second-harmonic generation to 2048 Å in beta-BaB₂O₄". *IEEE journal of quantum electronics*, 1986. **22**: p. 1013.
77. J.B. Guild, C. Xu, and W.W. Webb, "Measurement of group delay dispersion of high numerical aperture objective lenses using two-photon excited fluorescence". *Applied optics*, 1997. **36**(1): p. 397-401.
78. S. Huang, A.A. Heikal, and W.W. Webb, "Two-photon fluorescence spectroscopy and microscopy of NAD (P) H and flavoprotein". *Biophysical journal*, 2002. **82**(5): p. 2811-2825.
79. J. Zhao, S. Zandi, F. Feng, H. Zeng, D.I. McLean, and H. Lui. "Assessing topographic cutaneous autofluorescence variation using fluorescence UV and visible excitation emission matrix (EEM) spectroscopy". in *SPIE BiOS*. 2011. International Society for Optics and Photonics.

80. X. Han and E. Brown, "Measurement of the ratio of forward-propagating to back-propagating second harmonic signal using a single objective". *Optics express*, 2010. **18**(10): p. 10538-10550.
81. A.A. Tanbakuchi, A.R. Rouse, and A.F. Gmitro, "Monte Carlo characterization of parallelized fluorescence confocal systems imaging in turbid media". *Journal of biomedical optics*, 2009. **14**(4): p. 044024-044024-16.
82. W.-F. Cheong, S.A. Prahl, and A.J. Welch, "A review of the optical properties of biological tissues". *IEEE journal of quantum electronics*, 1990. **26**(12): p. 2166-2185.
83. G. Marquez, L.V. Wang, S.-P. Lin, J.A. Schwartz, and S.L. Thomsen, "Anisotropy in the absorption and scattering spectra of chicken breast tissue". *Applied Optics*, 1998. **37**(4): p. 798-804.
84. R. LaComb, O. Nadiarnykh, S. Carey, and P.J. Campagnola, "Quantitative second harmonic generation imaging and modeling of the optical clearing mechanism in striated muscle and tendon". *Journal of biomedical optics*, 2008. **13**(2): p. 021109-021109-11.
85. A. Arie, N. Habshoosh, and A. Bahabad, "Quasi phase matching in two-dimensional nonlinear photonic crystals". *Optical and Quantum Electronics*, 2007. **39**(4-6): p. 361-375.
86. V. Berger, "Nonlinear photonic crystals". *Physical Review Letters*, 1998. **81**(19): p. 4136.
87. A. Cowan and J.F. Young, "Mode matching for second-harmonic generation in photonic crystal waveguides". *Physical Review B*, 2002. **65**(8): p. 085106.
88. J. Martorell, R. Vilaseca, and R. Corbalan, "Second harmonic generation in a photonic crystal". *Applied physics letters*, 1997. **70**(6): p. 702-704.
89. K. Sakoda, "*Optical properties of photonic crystals*". Vol. 80. 2004: Springer Science & Business Media.
90. D.B. Ameen, M.F. Bishop, and T. McMullen, "A lattice model for computing the transmissivity of the cornea and sclera". *Biophysical journal*, 1998. **75**(5): p. 2520-2531.
91. M. Maccarana, S. Kalamajski, M. Kongsgaard, S.P. Magnusson, Å. Oldberg, and A. Malmström, "Dermatan sulfate epimerase 1-deficient mice have reduced content and changed distribution of iduronic acids in dermatan sulfate and an altered collagen structure in skin". *Molecular and cellular biology*, 2009. **29**(20): p. 5517-5528.
92. T.C. Battaglia, R.T. Clark, A. Chhabra, V. Gaschen, E.B. Hunziker, and B. Mikic, "Ultrastructural determinants of murine achilles tendon strength during healing". *Connective tissue research*, 2003. **44**(5): p. 218-224.
93. S. Rigozzi, R. Müller, and J. Snedeker, "Collagen fibril morphology and mechanical properties of the Achilles tendon in two inbred mouse strains". *Journal of anatomy*, 2010. **216**(6): p. 724-731.
94. S. Bancelin, C. Aimé, I. Gusachenko, L. Kowalczyk, G. Latour, T. Coradin, and M.-C. Schanne-Klein. "Second Harmonic Generation quantitative measurements on collagen fibrils through correlation to electron microscopy". in *SPIE BiOS*. 2015. International Society for Optics and Photonics.
95. A.N. Bashkatov, E.A. Genina, V.I. Kochubey, and V.V. Tuchin. "Estimation of wavelength dependence of refractive index of collagen fibers of scleral tissue". in *EOS/SPIE European Biomedical Optics Week*. 2000. International Society for Optics and Photonics.

96. D. Leonard and K. Meek, "Refractive indices of the collagen fibrils and extrafibrillar material of the corneal stroma". *Biophysical journal*, 1997. **72**(3): p. 1382.
97. K. Binder and D. Heermann, "*Monte Carlo simulation in statistical physics: an introduction*". 2010: Springer Science & Business Media.
98. S.L. Jacques and L. Wang, Monte Carlo modeling of light transport in tissues, in *Optical-thermal response of laser-irradiated tissue*. 1995, Springer. p. 73-100.
99. L. Wang, S.L. Jacques, and L. Zheng, "MCML—Monte Carlo modeling of light transport in multi-layered tissues". *Computer methods and programs in biomedicine*, 1995. **47**(2): p. 131-146.
100. V. Periyasamy and M. Pramanik, "Monte Carlo simulation of light transport in tissue for optimizing light delivery in photoacoustic imaging of the sentinel lymph node". *Journal of biomedical optics*, 2013. **18**(10): p. 106008-106008.

Appendices

Appendix A Monte Carlo method for simulating photon transportation

In Chapter 4, we describe a method of quantify the scattering of forward generated SHG in the backward direction. The Monte Carlo (MC) method is applied to investigate the distribution of the SHG photons in the tissue sample and is an essential part of that research. The MC method for photon propagation in tissues is based on simulating a large number of individual photons propagating through tissue [97]. It involves with building of a stochastic model in which the expected value of a random variable is determined. This expected value is estimated by measuring many independent events according to random numbers describing the distribution of some of the variables. The following description is by no means a complete description about MC, but it serves as the purpose of a preliminary introduction.

The flowchart for typical photon propagation through tissue is shown in Fig. A.1. This method was first introduced by Wang et al. [98, 99]. The photon's position and direction is first specified by the Cartesian coordinates. Each photon starts with a weight of unity and subsequently loses weight as it goes through procedures such as absorption, reflection and transmission.

The propagation step size s of the photon is determined from the optical properties of the sample and a sampling of the probability distribution as

$$s = \frac{-\ln(\xi)}{\mu_t} \quad (\text{A.1})$$

μ_t is the interaction coefficient comprising of absorption coefficient μ_a and scattering coefficient μ_s . ξ is a random number. Once the step size s is specified, the photon new position can be

updated and a fraction of the photon's weight is lost. When the photon is scattered, there is a deflection angle ψ ranging from 0 to π and an azimuthal angle φ ranging between 0 and 2π . They are going to be sampled statistically. The choice of $\cos\psi$ and an azimuthal angle φ can be expressed as a function of the random number ξ ,

$$\cos\psi = \begin{cases} \frac{1}{2g} \left\{ 1 + g^2 - \left[\frac{1-g^2}{1-g+2g\xi} \right]^2 \right\} & \text{if } g > 0 \\ 2\xi - 1 & \text{if } g = 0 \end{cases} \quad (\text{A.2})$$

$$\varphi = 2\pi\xi \quad (\text{A.3})$$

g is the anisotropy and has a value between -1 and 1. A value of 0 indicates isotropic scattering and a value near 1 indicates forward directed scattering. Value of g is ~ 0.9 for tissues in the visible spectrum. Once the deflection angle and azimuthal angle are chosen, the new direction of photon can be calculated. When the photon hits the boundary, it may either escape the medium or be reflected by the boundary. The probability of a photon being reflected depends on the angle of incidence α_i . Snell's law determines the angle of transmission α_t according to $n_i \sin\alpha_i = n_t \sin\alpha_t$. n_i and n_t are the refractive index of the medium. Furthermore, the average of the internal reflectance for orthogonal polarization directions $R(\alpha_i)$ is

$$R(\alpha_i) = \frac{1}{2} \left[\frac{\sin^2(\alpha_i - \alpha_t)}{\sin^2(\alpha_i + \alpha_t)} + \frac{\tan^2(\alpha_i - \alpha_t)}{\tan^2(\alpha_i + \alpha_t)} \right] \quad (\text{A.4})$$

Whether the photon is internally reflected or escaped depends on the comparison of a random number with the internal reflectance. If a photon step size s is large enough to hit the interface and remaining step size ahead of the interface is s_1 , it is first moved to the interface without interactions and the remaining step size is $s-s_1$. The probability of following reflection or transmission is according to Fresnel's law mentioned previously.

If the Photon is neither reflected nor transmitted, it keeps propagating unless it is absorbed. Any photon with low weight is to be removed so that the simulation ends in a reasonable amount of time. When photons are absorbed, or exit the media due to transmission or reflection, it is recorded at where it exits or is absorbed.

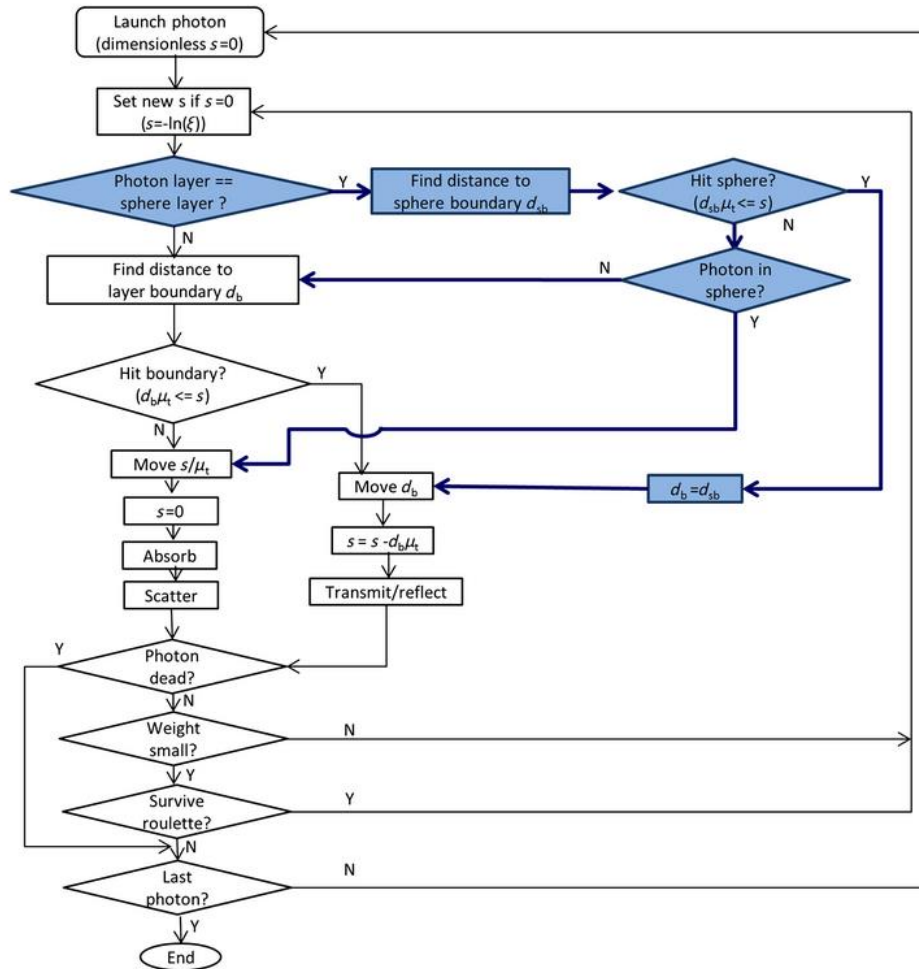


Figure A. 1 Flowchart for Monte Carlo simulation of photon propagation in tissues. From © V. Periyasamy and M. Pramanik, “Monte Carlo simulation of light transport in tissue for optimizing light delivery in photoacoustic imaging of the sentinel lymph node”. Journal of biomedical optics, 2013. 18(10): p. 106008-106008 [100]. Page 3. By permission from publisher.

Appendix B Plane wave expansion method

We use the plane wave expansion method to solve the electrical field satisfying Maxwell equation in a periodic structure in Chapter 5. For the completeness of our discussions, the key derivation steps and equations from Ref. [89] are quoted here. In a periodic structure, the partial differential equation for a field component E_z that is parallel with the long axis of the collagen cylinder (z axis) is,

$$\frac{1}{\varepsilon(\vec{r})} \left(\frac{\partial^2}{\partial x^2} + \frac{\partial^2}{\partial y^2} \right) E_z(\vec{r}) + \frac{\omega^2}{c^2} E_z(\vec{r}) = 0 \quad (\text{B.1})$$

the solutions to Eq.(B.1) can be written in the form

$$E_z(\vec{r}) = u(\vec{r}) \exp(i\vec{k}\vec{r}) \quad (\text{B.2})$$

$u(\vec{r})$ is a periodic function with period a and $\exp(i\vec{k}\vec{r})$ is the propagation part of the electrical field. In plane wave expansion, we need the reciprocal lattice vectors $\mathbf{G} (m,n)=m\mathbf{d}_1+n\mathbf{d}_2$, to expand a periodic function into a Fourier series. The $u(\vec{r})$ is expanded as,

$$u(\vec{r}) = \sum_{\vec{G}} \frac{A_k(\vec{G})}{|\vec{k} + \vec{G}|} \exp(i\vec{G}\vec{r}) \quad (\text{B.3})$$

With the reciprocal dielectric constant $1/\varepsilon$ also expanded by \mathbf{G} vectors, we substitute the expression of electrical field and reciprocal dielectric function into Eq. (B.1),

$$\sum_{\vec{G}} \left[\left[\vec{k} + \vec{G} \middle| \vec{k} + \vec{G}' \right] \kappa(\vec{G} - \vec{G}') A_k(\vec{G}') \right] = \frac{\omega^2}{c^2} A_k(\vec{G}) \quad (\text{B.4})$$

This eigenvalue equation Eq. (B.4) can be explicitly written in the form as

$$\begin{bmatrix} M_{11} & M_{12} & M_{13} & \cdots \\ M_{21} & M_{22} & M_{23} & \cdots \\ M_{31} & M_{32} & M_{33} & \cdots \\ \vdots & \vdots & \vdots & \ddots \end{bmatrix} \begin{bmatrix} A_k(G_1) \\ A_k(G_2) \\ A_k(G_3) \\ \vdots \end{bmatrix} = \frac{\omega^2}{c^2} \begin{bmatrix} A_k(G_1) \\ A_k(G_2) \\ A_k(G_3) \\ \vdots \end{bmatrix} \quad (\text{B.5})$$

These are matrix eigenvalue equations describing the dispersion relation of the electrical field, of the form

$$\hat{M}\vec{A} = \frac{\omega^2}{c^2} \vec{A} \quad (\text{B.6})$$

Each element of the matrix M is

$$M_{ij} = \left[\left[\vec{k} + \vec{G}_i \right] \left[\vec{k} + \vec{G}_j \right] \right] \kappa(\vec{G}_i - \vec{G}_j) \quad (\text{B.7})$$

The M matrix size is 187 by 187. The number of reciprocal lattice vectors \mathbf{G} are chosen to ensure that all of the reciprocal lattice vectors up to a given length were included. This is analogous to choosing both positive and negative frequencies up to a cutoff frequency in a Fourier expansion. The eigenvectors A_k are the expansion coefficient of the fields in Eq. (B.4) and ω/c are the eigenfrequency corresponding to the wave vector. Substituting A_k into Eq. (B.2) and (B.3), the electrical field E_z in the structure is obtained, given excitation wave vector \mathbf{k}_1 and frequency ω .

The following band diagram illustrates the multiple eigenfrequencies for a single k vector. We repeated the calculation in Fig. 2.4 of the Ref. [89] to verify the band calculations. Symbols Γ , X, M in the horizontal axis represent wave vectors of $(0, 0)$, $(0, \pi/a)$, and $(\pi/a, \pi/a)$. They are special points in the k wave space because they are on the edge of the first Brillouin zone, which is formed by the shortest lines between reciprocal lattice points. Corresponding to a single wave vector, there are multiple normalized frequencies given by $\omega a/2\pi c$ because adding

an integer times of π/a along k_x or k_y direction is considered as a same \mathbf{k} in a periodic structure. The similarity for the first few band curves between our results and the text book results demonstrate that our solving of the eigenfunction is correct.

The field patterns of the first band are shown in Fig. B. 2 (a) and (b). The simulation parameters are $a = 150$ nm, $d = 140$ nm, $n_{cylinder} = 1.4$, $n_{medium} = 1.3$. For patterns at 800 nm and 400 nm excitation wavelength, the intensity is concentrated in the higher index cylinder, which is split into four pieces at the corner of the figures. This can be observed more obviously with the field pattern for $d = 30$ nm in Fig. B. 2 (c). The intensity contrast between high and low refractive index is larger for the 400 nm excitation because the wavelength is closer to the dimension of the cylinders and spacing between them.

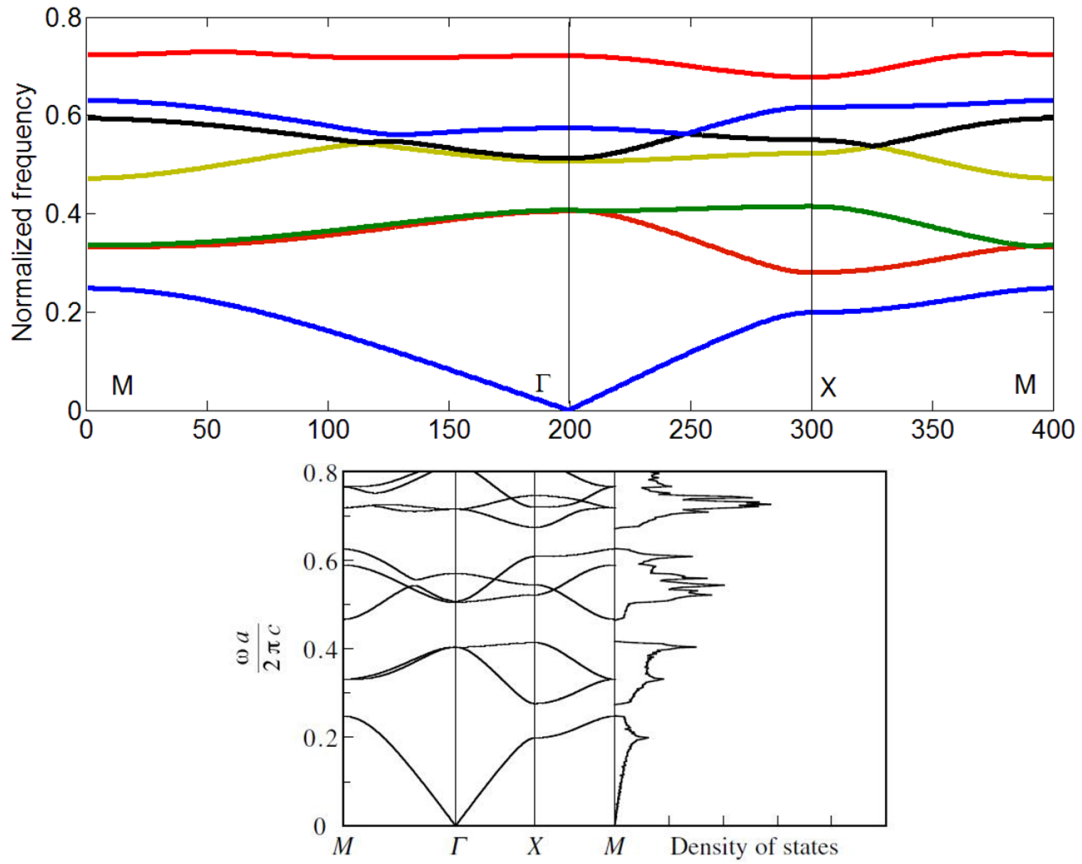


Figure B. 1 Comparison of (top) our calculated photonic band structure of a 2D square lattice composed of circular cylinders with the (bottom) results given in text book. The parameters used are the same. From © K. Sakoda, “Optical properties of photonic crystals”. Vol. 80. 2004: Springer Science & Business Media. Page 29. By permission from publisher.

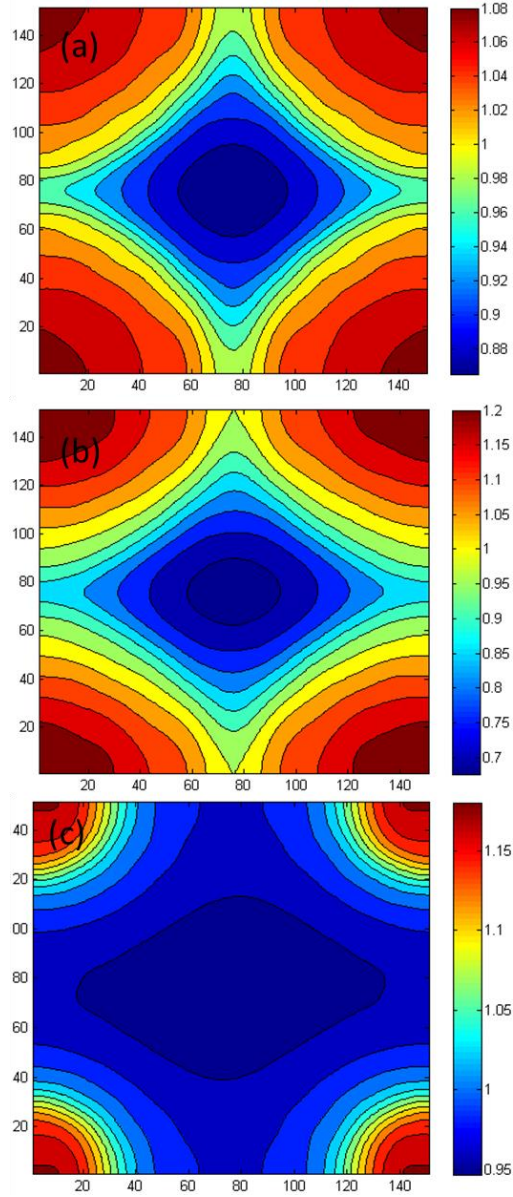


Figure B. 2 Electrical fields inside a unit square array of dielectric cylinders in medium. The color indicates the amplitude of the electrical field. The parameter simulations are $a = 150$ nm, $d = 140$ nm, $n_{cylinder} = 1.4$, $n_{medium} = 1.3$ with excitation wavelength at 800 (a) and 400 nm (b). In (c), the excitation wavelength is 800 nm and $d = 30$ nm.

With a fundamental field incidence, if each cylinder responds by generating SHG field, the SHG field function satisfies

$$\left[-\frac{1}{c^2} \frac{\partial^2}{\partial t^2} + \frac{1}{\varepsilon(x)} \left(\frac{\partial^2}{\partial x^2} + \frac{\partial^2}{\partial y^2} \right) \right] E_{2\omega} = -\frac{4\pi\chi^{(2)}(2\omega)^2}{c^2\varepsilon(x)} E_\omega^2 \quad (\text{B.8})$$

in which $E_{2\omega}$ and E_ω are complex SHG and fundamental fields. By applying Green's function

$$E_{2\omega} = \frac{4i\pi^2(2\omega)^2}{V} \sum_{\mathbf{K}} E_{\mathbf{K}}(r) \int_V dr' \chi^{(2)} E_{\mathbf{K}}^*(r') E_k(r') E_k(r') \quad (\text{B.9})$$

The subscript \mathbf{K} and k differentiate $E_{2\omega}$ from E_ω by propagation wave vector. According to Eq. (B.3), the integral in Eq. (B.9) is

$$\begin{aligned} & \int_V dr' \chi^{(2)} E_{\mathbf{K}}^*(r') E_k(r') E_k(r') \\ &= \int_V dr' \chi^{(2)} u_{\mathbf{K}}^*(r') u_k(r') u_k(r') \exp[i(k_x + k'_x - K_x)x'] \exp[i(k_y + k'_y - K_y)y'] \\ &= \sum_{j=0}^{N_x-1} \sum_{l=0}^{N_y-1} \int_{V_0} dr' \chi^{(2)} u_{\mathbf{K}}^*(r') u_k(r') u_k(r') \\ & \times \exp[i(k_x + k'_x - K_x)(x' + ja)] \exp[i(k_y + k'_y - K_y)(y' + la)] \\ &= V_0 F(k, K) \frac{1 - \exp[i(k_x + k'_x - K_x)aN_x]}{1 - \exp[i(k_x + k'_x - K_x)a]} \times \frac{1 - \exp[i(k_y + k'_y - K_y)aN_y]}{1 - \exp[i(k_y + k'_y - K_y)a]} \\ &= V_0 F(k, K) \exp(ia(N_x - 1)\Delta k_x / 2) \frac{\sin(aN_x \Delta k_x / 2)}{\sin(a\Delta k_x / 2)} \\ & \times \exp(ia(N_y - 1)\Delta k_y / 2) \frac{\sin(aN_y \Delta k_y / 2)}{\sin(a\Delta k_y / 2)} \end{aligned} \quad (\text{B.10})$$

The $F(k, K)$ function term can be considered as an effective nonlinear susceptibility with respect to the fundamental and SHG fields within a unit cell which is expressed in Eq. (B.11).

$$F(k, K) = \frac{1}{V_0} \int_{V_0} dr' \chi^{(2)} u_{\mathbf{K}}^*(r') u_k(r') u_k(r') \exp(i\Delta k_x x') \exp(i\Delta k_y y') \quad (\text{B.11})$$

Here V_0 denotes the volume of the unit cell. The N_x and N_y represent the number of cylinders along the lateral and depth direction in the focal volume. Physically, it describes the number of

cylinders in the focal volume. In this way, the integral of electrical fields in the whole space is simplified to the integral in a unit volume. Substituting $K = k_2$ and $k = k_1$, the SHG intensity in a periodic structure is expressed as

$$|E_{2\omega}|^2 = 16\pi^4 \left(\frac{\omega a}{2\pi c} \right)^2 \left(\frac{c}{v_g} \right)^2 |E_{k_2}(r)|^2 |F(k_1, k_2)|^2 \left| \frac{\sin(aN_x \Delta k_x / 2)}{\sin(a\Delta k_x / 2)} \right|^2 \left| \frac{\sin(aN_y \Delta k_y / 2)}{\sin(a\Delta k_y / 2)} \right|^2 \quad (\text{B.12})$$

Assuming that ε is real and matrix M is then a Hermitian matrix, the group velocity v_g is calculated by Hellmann-Feynman theorem as

$$A_k^{t*}(G) \frac{\partial M(k)}{\partial k_y} A_k(G) = \frac{\partial}{\partial k_y} \left(\frac{\omega_k^2}{c^2} \right) = \frac{2\omega_k}{c^2} v_g(\omega, k) \quad (\text{B.13})$$

where t denotes the transposed matrix and

$$\frac{\partial M(k)}{\partial k_y} = \left[\frac{|k+G'|}{|k+G|} (k_y + G_y) + \frac{|k+G|}{|k+G'|} (k_y + G'_y) \right] \times \kappa(G - G') \quad (\text{B.14})$$

The group velocity can be readily evaluated once the eigenvector and eigenfrequency are obtained by the band calculation.